

AD-A087 849

BOEING AEROSPACE CO SEATTLE WA  
CENTRIFUGE CRATER SCALING EXPERIMENT I. DRY GRANULAR SOILS. (U)  
FEB 78 R M SCHMIDT, K A HOLSAPPLE

DNA001-77-C-0169

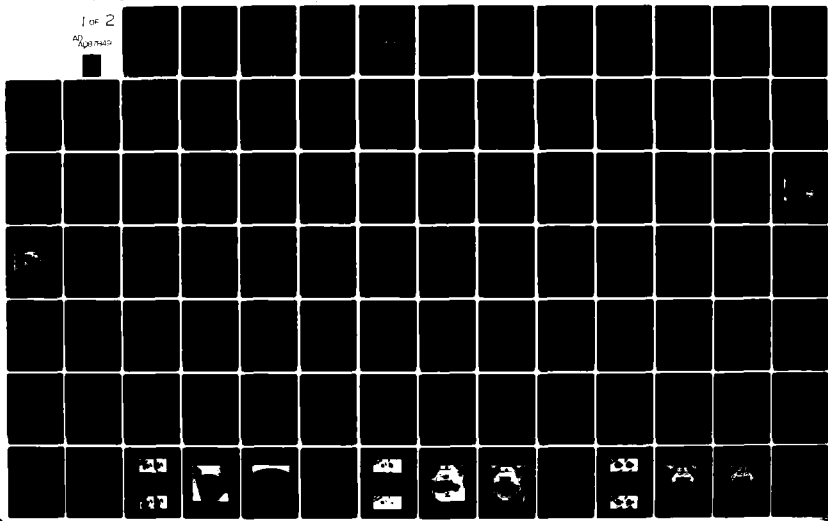
F/6 19/1

DNA-4568F

NL

UNCLASSIFIED

1 of 2  
AD-A087 849



ADA 087849

LEVEL II

AD-E300 863\*

12

DNA 4568F

# CENTRIFUGE CRATER SCALING EXPERIMENT I

## Dry Granular Soils

Boeing Aerospace Company  
P.O. Box 3999  
Seattle, Washington 98124

1 February 1978

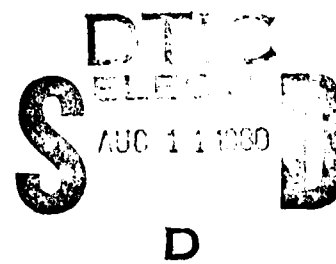
Final Report for Period 14 March 1977—31 January 1978

CONTRACT No. DNA 001-77-C-0169

APPROVED FOR PUBLIC RELEASE;  
DISTRIBUTION UNLIMITED.

THIS WORK SPONSORED BY THE DEFENSE NUCLEAR AGENCY  
UNDER RDT&E RMSS CODE B342077462 H35HAXSX35524 H2590D.

Prepared for  
Director  
DEFENSE NUCLEAR AGENCY  
Washington, D. C. 20305



80 7 16 048

DDC FILE COPY

Destroy this report when it is no longer  
needed. Do not return to sender.

PLEASE NOTIFY THE DEFENSE NUCLEAR AGENCY,  
ATTN: TISI, WASHINGTON, D.C. 20305, IF  
YOUR ADDRESS IS INCORRECT, IF YOU WISH TO  
BE DELETED FROM THE DISTRIBUTION LIST, OR  
IF THE ADDRESSEE IS NO LONGER EMPLOYED BY  
YOUR ORGANIZATION.



UNCLASSIFIED

SECURITY CLASSIFICATION OF THIS PAGE (When Data Entered)

REPORT DOCUMENTATION PAGE		READ INSTRUCTIONS BEFORE COMPLETING FORM
1. REPORT NUMBER DNA 4568F	2. GOVT ACCESSION NO. AD-A087849	3. RECIPIENT'S CATALOG NUMBER
4. TITLE (and Subtitle) CENTRIFUGE CRATER SCALING EXPERIMENT I. Dry Granular Soils	5. TYPE OF REPORT & PERIOD COVERED Final Report. Period 00 14 Mar 77-31 Jan 78	
6. AUTHOR(s) R. M. Schmidt K. A. Holsapple	7. CONTRACT OR GRANT NUMBER(S) DNA 001-77-C-0169	
8. PERFORMING ORGANIZATION NAME AND ADDRESS Boeing Aerospace Company P.O. Box 3999 Seattle, Washington 98124	9. PROGRAM ELEMENT, PROJECT, TASK AREA & WORK UNIT NUMBERS Subtask H35HAXS X355-24	
10. CONTROLLING OFFICE NAME AND ADDRESS Director Defense Nuclear Agency Washington, D.C. 20305	11. REPORT DATE 1 February 1978	
12. MONITORING AGENCY NAME & ADDRESS (if different from Controlling Office) X355	13. NUMBER OF PAGES 172	
14. DISTRIBUTION STATEMENT (of this Report) Approved for public release; distribution unlimited.	15. SECURITY CLASS (of this report) UNCLASSIFIED	
16. DECLASSIFICATION/DOWNGRADING SCHEDULE	17. DISTRIBUTION STATEMENT (of the abstract entered in Block 20, if different from Report)	
18. SUPPLEMENTARY NOTES This work sponsored by the Defense Nuclear Agency under RDT&E RMSS Code B342077462 H35HAXS X35524 H2590D.	19. KEY WORDS (Continue on reverse side if necessary and identify by block number) Accelerated Frame Testing      Alluvium      Gravity Dimensional Analysis      Centrifuge      JOHNIE BOY Similarity Analysis      Cratering      Ottawa Sand Similitude Requirements      Crater Scaling      PETN	
20. ABSTRACT (Continue on reverse side if necessary and identify by block number) Theoretical similitude requirements were derived. Applicability of these results to high G centrifuge cratering experiments was demonstrated using Ottawa sand which also allowed comparison with UDRI 1G results. A scaling rule was devised which adequately accounts for large differences in the properties of various chemical explosives. A centrifuge simulation of the JOHNIE BOY 500 ton event was satisfactorily performed demonstrating the overall applicability of the centrifuge method to simulate very large yield nuclear cratering events.		

DD FORM 1 JAN 73 1473 EDITION OF 1 NOV 65 IS OBSOLETE

UNCLASSIFIED

SECURITY CLASSIFICATION OF THIS PAGE (When Data Entered)

059610

## SUMMARY

Centrifuge experimental techniques provide possibilities for laboratory simulation of ground shock and cratering effects due to nuclear weapons. This premise is predicted upon the results of a similarity analysis which indicates that increased gravity is a necessary condition for subscale testing. The objectives of this investigation were to examine the similarity requirements of this type of subscale testing both theoretically and experimentally. To do this, a series of centrifuge experiments were performed to validate theoretical similarity requirements as well as to determine the practicality of applying the technique to dry granular soils with little or no cohesion.

Two sets of experiments were performed. The first was a series of ten shots using Ottawa sand as a convenient and well-characterized test medium. Results of these experiments are:

- a) Reproducibility was confirmed in the centrifuge environment.
- b) Particle size effects on final crater configuration were determined to be negligible for the cases considered.
- c) Validity of the derived similitude requirements was demonstrated.
- d) Scaling rules for apparent crater size and equivalence among different explosive types were derived.

Upon the successful completion of the Ottawa sand experiments, a second set of experiments was undertaken to simulate a large-scale cratering event. The JOHNIE BOY 500-ton nuclear field event of 1962 was chosen for the centrifuge simulation study. The prototype geology was a dry homogeneous alluvium which was straightforward to reconstitute on the centrifuge. It was a well-characterized event for which considerable computations of cratering mechanics were performed and it was used as a standard to develop a full-scale simulation method for cratering, demonstrated by the MINE THROW 120-ton Ammonium Nitrate/Fuel Oil (ANFO) experiment performed in 1971.

An equivalent full-scale PETN spherical charge configuration was determined. The equivalence criteria was based upon matching the kinetic energy

into the ground as well as the shape of the flow field. This hypothetical event was then simulated at subscale on a centrifuge at 345 G. The results satisfactorily demonstrated the applicability of using a centrifuge to simulate a small-yield nuclear-cratering event in alluvium.

The utility of the centrifuge method is based upon scaling results that indicate the equivalent full-scale explosive yield is equal to the actual charge size used in the subscale experiment times the cube of the centripetal acceleration.

Accession For	
NTIS GRA&I	
DDC TAB	
Unannounced	
Justification	
By _____	
Distribution/	
Availability Codes	
Dist.	Avail and/or special
A	

DTIC  
ELECTED  
S D  
AUG 11 1980  
D

## PREFACE

The authors would like to thank the following individuals and acknowledge their help and participation in this program.

Major G. J. Goss who, as technical monitor for DNA, provided enthusiastic direction contributing to the success of the program.

A. J. Piekutowski of the University of Dayton Research Institute (UDRI) who took a personal interest in sharing his proven experimental techniques for studying explosive crater formation in Ottawa sand.

F. W. Davies, A. B. Zimmerschied, H. E. Watson, and C. R. Wauchope of the Boeing Shock Physics Lab who provided laboratory support, helped with the ordnance applications and assisted in the data reduction.

B. M. Lempriere of the Boeing Aerospace Company whose critical reading and discussions contributed to the final report.

R. W. Henny of the Air Force Weapons Laboratory (AFWL) who provided technical information on soil selection and supplied the soils. These would have been very difficult to obtain without his help.

R. T. Allen and E. S. Gaffney of Pacifica Technology who performed the high explosive/nuclear equivalence calculations and who helped devise the test matrix to provide a useful and logical sequence of experiments based upon a restricted number of shots.

M. Y. C. Hou of the University of Washington who explored the feasibility of a dynamic stereo photogrammetry technique which could be applied to centrifuge on-board nonmetric cameras and used to document crater stability under large centripetal accelerations.

## TABLE OF CONTENTS

<u>SECTION</u>	<u>TITLE</u>	<u>PAGE</u>
	SUMMARY .....	1
	PREFACE .....	3
	LIST OF ILLUSTRATIONS .....	6
	LIST OF TABLES .....	8
1	INTRODUCTION .....	9
	1-1 BACKGROUND .....	9
	1-2 OBJECTIVES/APPROACH .....	10
2	THEORY OF MODELING .....	13
	2-1 SIMILARITY ANALYSIS OF FIELD EQUATIONS .....	14
	2-2 ANALYSIS OF SPECIFIC CONSTITUTIVE EQUATIONS .....	20
	2-3 DIMENSIONLESS PARAMETERS .....	28
3	EXPERIMENTAL TECHNIQUE .....	36
	3-1 CENTRIFUGE DESCRIPTION .....	36
	3-2 EXPLOSIVE CHARGE DESIGN .....	39
	3-3 SAMPLE PREPARATION .....	44
	3-4 TEST PROCEDURE .....	48
	3-5 1-G CONTROL SHOTS .....	49
4	OTTAWA SAND RESULTS .....	51
	4-1 PARTICLE SIZE DEPENDENCE .....	51
	4-2 CONSTANT $\pi_2$ TEST .....	53
	4-3 SCALING RULES .....	56
5	JOHNNIE BOY SIMULATION .....	63
	5-1 KAFB ALLUVIUM SCALING RULES .....	63
	5-2 NUCLEAR-PETN EQUIVALENCE .....	68
	5-3 EVALUATION OF RESULTS .....	69

TABLE OF CONTENTS (CONTINUED)

<u>SECTION</u>	<u>TITLE</u>	<u>PAGE</u>
6	CONCLUSIONS .....	76
7	REFERENCES .....	78
APPENDIX A: CENTRIFUGE SHOT RECORDS .....		81
APPENDIX B: 1-G CONTROL SHOT RECORDS .....		119
APPENDIX C: MATERIAL PROPERTIES OF TEST SOILS .....		137
APPENDIX D: STEREO CAMERA DYNAMIC PHOTOGRAHAMTRY .....		149

## LIST OF ILLUSTRATIONS

<u>FIGURE</u>		<u>PAGE</u>
1	Boeing 600 G centrifuge .....	37
2	Swing basket showing details of soil containers .....	38
3	Scaling rules for apparent crater volume in Ottawa sand .....	57
4	Scaling rule for apparent crater radius in Ottawa sand .....	58
5	Scaling rule for apparent crater depth in Ottawa sand .....	59
6	Scaling rule for apparent crater volume in KAFB alluvium .....	65
7	Scaling rule for apparent crater radius in KAFB alluvium .....	66
8	Scaling rule for apparent crater depth in KAFB alluvium .....	67
9	Kinetic energy coupling of JOHNIE BOY versus PETN simulation ...	70
10	Flow field comparison of JOHNIE BOY versus PETN simulation .....	71
11	Centrifuge simulation sensitivity to equivalent burial depth ...	72
12	JOHNIE BOY, centrifuge simulation and MINE THROW compared .....	73
A1	Comparison of crater 10-X with crater 10-0 .....	83
A2	Comparison of crater 11-X with crater 11-0 .....	87
A3	Comparison of crater 12-X with crater 12-0 .....	91
A4	Comparison of crater 13-X with crater 13-0 .....	95
A5	Comparison of crater 14-X with crater 14-0 .....	99
A6	Comparison of crater 15-X with crater 15-0 .....	103
A7	Comparison of crater 16-X with crater 16-0 .....	107
A8	Comparison of crater 17-X with crater 17-0 .....	111
A9	Comparison of crater 18-X with crater 18-0 .....	115
B1	Comparison of crater UDRI-9 with crater UDRI-22 .....	121
B2	Comparison of craters UDRI-117, UDRI-120 and UDRI-146 .....	124
B3	Comparison of crater UDRI-642 with crater UDRI-644 .....	126
B4	Comparison of crater UDRI-643 with crater UDRI-645 .....	128
B5	Comparison of craters UDRI-646, UDRI-647 and UDRI-648 .....	131
B6	Comparison of crater UDRI-649 with crater UDRI-652 .....	133
B7	Comparison of crater UDRI-650 with crater UDRI-651 .....	135

LIST OF ILLUSTRATIONS (CONTINUED)

<u>FIGURE</u>		<u>PAGE</u>
C1	Modeling clay triaxial compression test .....	142
C2	Sawing sand triaxial compression test .....	143
C3	Flintshot sand triaxial compression test .....	144
C4	Banding sand triaxial compression test .....	145
C5	KAFB alluvium no. 2 triaxial compression test .....	146
C6	KAFB alluvium no. 4 triaxial compression test .....	147
D1	Centrifuge rotor showing cameras and mounted sample .....	151
D2	The fixed camera base in the rotor hub of the centrifuge .....	152
D3	Control frame and control points .....	153
D4	Stereo-photos of craters at 10 G and 100 G .....	155
D5	The generalized flow chart for photogrammetric computation .....	160
D6	Topographic map for a typical crater .....	163
D7	Crater photo and profile determined by profilometer .....	164

LIST OF TABLES

<u>TABLE</u>		<u>PAGE</u>
1	Bomb calorimeter measurements for various explosive devices ....	41
2	Material properties for the four different explosive charges ...	43
3	Grain size distribution for three Ottawa sands .....	45
4	Ottawa sand cratering data summary .....	52
5	Variation of crater volume due to particle size effects .....	54
6	KAFB alluvium cratering data summary .....	64
A1	Ottawa sand centrifuge data for shots 10-X and 10-0 .....	82
A2	Ottawa sand centrifuge data for shots 11-X and 11-0 .....	86
A3	Ottawa sand centrifuge data for shots 12-X and 12-0 .....	90
A4	Ottawa sand centrifuge data for shots 13-X and 13-0 .....	94
A5	"Permaplast" clay centrifuge data for shots 14-X and 14-0 .....	98
A6	Ottawa sand centrifuge data for shots 15-X and 15-0 .....	102
A7	KAFB alluvium centrifuge data for shots 16-X and 16-0 .....	106
A8	KAFB alluvium centrifuge data for shots 17-X and 17-0 .....	110
A9	KAFB alluvium centrifuge data for shots 18-X and 18-0 .....	114
B1	Ottawa sand 1-G control shots, 1.7 grams lead azide .....	120
B2	Ottawa sand 1-G control shots, 0.4 gram PETN .....	122
B3	Ottawa sand 1-G control shots, 1.265 grams PETN .....	125
B4	Ottawa sand 1-G control shots, 4.0 grams PETN .....	127
B5	KAFB alluvium 1-G control shots, 1.7 grams lead azide .....	129
B6	KAFB alluvium 1-G control shots, 1.265 grams PETN .....	132
B7	KAFB alluvium 1-G control shots, 4.0 grams PETN .....	134
D1	Distance determination employing the control frame .....	161
D2	Surface area and volume determination for the control frame ....	162

## SECTION 1 INTRODUCTION

### 1-1 BACKGROUND

The centrifuge has been used extensively to study the quasi-static response of soil structures to lithostatic loadings. This type of geotechnical modeling has gained little acceptance in the United States but has been widely used in Europe and in the Soviet Union during the past thirty years.<sup>1</sup>

The applicability of this method to dynamic experiments is not as well, if at all, established. Pokrovsky and Fyodorov<sup>2</sup> discuss experiments designed to study the effects of buried explosives used in the construction industry. In chapter eight of the second volume, they extensively address the question of ground shock as applied to failure prediction of soil materials for excavation purposes. In volume one, a few pages are devoted to the description of an investigation of the soil ejected by the action of an explosion. These early experiments, performed during the 1940's, used 1.5 gram detonator caps as the explosive source and were conducted in two different soil media: a dry sand and a moist clay. The centrifuge was operated at 65 G for the sand and at 100 G for the clay. In both cases, the results for the depth and the radius of the apparent crater were interpreted as satisfactory when compared with the calculated full size dimensions for the "natural state using the formula of Boreskov."

Scott and Morgan's<sup>1</sup> summary remarks concerning the entirety of the Russian geotechnical centrifuge work are especially applicable to these few reported cratering experiments. He states that "it is apparent from the effort put into the technique, that the Russian workers consider the centrifuge technique well proven, although it is not possible to discover from Pokrovsky's work<sup>2</sup> any satisfactory demonstration of the correlation between model and prototype tests for any of the studies he cites."

The only other reference to Soviet cratering experiments in an accelerated reference frame is the work of Viktorov and Stepenov.<sup>3</sup> Their work addressed soil excavation techniques using buried explosives. These

experiments, conducted with charges placed at optimum and greater depth of burial in moist sand, were not performed in a centrifuge. Since they were modeling the effect of a blast on the throw-out of soil and rocks, they chose to use a "linear accelerator" (presumably a rocket sled) to eliminate "the distortion of the results of the modeling by the Coriolis acceleration...."

In a recent investigation, Schmidt<sup>4</sup> examined the application of centrifuge experimental techniques to the modeling of cratering phenomena. An oil base modeling clay was used to investigate depth of burial effects at centripetal accelerations up to 480 G. The results of these experiments were in good agreement with the earlier work of Viktorov and Stepenov,<sup>3</sup> using the results of a dimensional analysis relating soil properties and explosive characteristics for the different experimental conditions. More importantly, by using the concept of a gravity-scaled charge yield parameter derived from the dimensional analysis, the results of both sets of high-G experiments were shown to compare favorably with data obtained from the Nevada Test Site (NTS) cratering series. This agreement for cratering efficiency as a function of non-dimensional depth of burst demonstrated the relevance of using subscale laboratory test performed at elevated gravity to predict large-scale cratering events in the field.

This work<sup>4</sup> emphasized cratering efficiency based upon apparent crater volume but left observed variations in crater shape unexplained. In addition, the gravity dependence due to the overburden may have dominated the phenomenon for buried shots which, in turn, may not be the case for near surface events. Additionally, the use of a cohesive oil base clay to model non-cohesive soils may have introduced offsetting strength effects and may have minimized possible Coriolis effects due to the cohesion of the overturning flap during crater formation. These concerns, as well as the design of a critical experiment to test the similitude hypothesis, provided the basis for the program described in this report.

## 1-2 OBJECTIVES/APPROACH

The overall objective of this program was to demonstrate, in a quantitative manner, the validity of using a laboratory-scale centrifuge

experiment to simulate an actual cratering event. The JOHNNIE BOY 500-ton nuclear cratering event was chosen for this purpose. It was conducted in the desert alluvium at NTS in July, 1962.

A systematic procedure for eliminating experimental uncertainties was devised. A new rotor for the Boeing 600-G centrifuge was fabricated to accommodate non-cohesive soils utilizing a symmetric swing-basket design. To verify the suitability of this configuration, ten test shots were performed using a well-characterized Ottawa sand. This sand type was chosen to allow direct comparison with the large body of high quality 1-G laboratory cratering data generated previously by Piekutowski.<sup>5,6</sup>

The first concern was reproducibility of data in the centrifuge environment to ensure that vibration, windage, slumping, and Coriolis effects did not invalidate proposed crater measurement techniques. The next step was to obtain preliminary confirmation that a gravity-scaled energy concept was applicable to a surface burst configuration in Ottawa sand. This will be referred to as the constant  $\pi_2$  test and is described in detail in Section 4-2. The final issue addressed by this series of tests was to determine the sensitivity of the high-G results to variations in sand-particle-size distribution. The results of these Ottawa sand experiments confirmed the suitability of the centrifuge technique for this type of modeling.

As is shown in Section 2, theoretical requirements for non-trivial scaling can be satisfied with a model material in the centrifuge identical to that of the prototype. Therefore, to simulate the JOHNNIE BOY event in a subscale experiment, it was imperative to use a soil that was characteristic of the original site. A suitable material was obtained from the Kirtland AFB (KAFB) environs and supplied by R. W. Henny of AFWL. Since this material differed significantly from the Ottawa sand, sample preparation techniques needed to be developed to ensure reproducibility. The constant  $\pi_2$  test was performed on samples of this material to confirm that the derived similarity requirements were valid for the KAFB alluvium.

For chemical explosives, the dependence upon different explosive properties can be accounted for by including the charge properties in the

dimensional analysis.<sup>4</sup> For nuclear events such as JOHNIE BOY, a high explosive/nuclear equivalence must be determined. To accomplish this, an analysis was performed based upon the so-called MINE THROW technique.<sup>7,8</sup> This involved calculations using a finite difference code to determine the size of an equivalent full-scale PETN charge size and an associated depth of burial. The PETN configuration was varied until the resulting early time flow field was in agreement with that calculated for the actual JOHNIE BOY nuclear event.<sup>9</sup> The results of these calculations<sup>10</sup> provided a hypothetical full-scale, high-explosive PETN event in which the charge radius was 1.88 meters and the depth of burial was 1.20 meters. The charge mass was 49.3 metric tons giving a nuclear equivalence factor of 13.4 percent. These calculated results were supplied by Allen.<sup>11</sup>

This hypothetical high-explosive equivalent event was to be simulated at laboratory subscale using a 1.25 gm PETN explosive charge. Based upon the similitude requirement  $g^3 E = \text{constant}$  and  $gL = \text{constant}$ , the experiment was to be performed at 345 G; hence, the test depth of burial was to be 120 cm/345 or 0.348 cm. (Actual placement was 0.362 cm.) To determine the sensitivity to the calculated equivalent depth of burial, Allen suggested that a second shot be performed at a burial depth of 0.845 cm.

A total of six shots were fired in this simulation series. Two shots under identical conditions demonstrated reproducibility. The next two shots using two different charge sizes confirmed that the KAFB alluvium satisfied the constant  $\pi_2$  test. Two final shots, performed at the conditions suggested by Allen<sup>11</sup>, bracketed the actual JOHNIE BOY results as predicted.

## SECTION 2

### THEORY OF MODELING

The modeling of full-scale cratering events by subscale centrifuge experiments is being investigated. To validate this technique, it is necessary to show under what conditions a subscale experiment does simulate a full-scale prototype and to determine the limitations and interpretations of subscale experiments. To examine these requirements, the relationships between comparable, but different scale, experiments are derived and studied.

Two methods are commonly used to derive modeling laws: similarity analyses and dimensional analyses. Similarity analyses require a complete set of equations adequate for describing the phenomena in question. Dimensional analyses, on the other hand, are based on an ad-hoc choice of independent variables, without regard to the physical laws relating them.

These two approaches overlap considerably. The governing equations of any phenomena, if properly posed, must be expressible in a dimensionally invariant form. Thus, if a dimensional analysis is performed, using those variables occurring in the complete set of governing equations together with appropriate initial and boundary conditions, then identical results are obtained by either method. Consequently, the identification of the governing equations serves also to identify the controlling variables.

In this section, a similarity analysis of cratering phenomena is presented. The analysis follows along the lines of Crowley<sup>12</sup> and Killian and Germain<sup>13</sup> with two significant differences. The general balance equations of continuum mechanics are employed, as opposed to particular forms used in the computer codes considered by Killian and Germain. Secondly, the similarity requirements of the general balance equations applicable to all materials are distinguished from the requirements imposed by particular constitutive equations used to describe various materials. In this way the generality of the results is more apparent. These results are then applied to the problem of a particular explosive detonated in or near a deformable soil medium with the region above the soil filled with a gas such as air. It is assumed that each of the three

media--the soil, the explosive, and the air, can be modeled as a continuum with appropriate constitutive equations. The general field equations will be discussed first.

## 2-1 SIMILARITY ANALYSIS OF FIELD EQUATIONS

The deformation and motion of any continuum must satisfy the field equation of mechanics in their general form. The general thermomechanical response of materials, given by Truesdell and Toupin,<sup>14</sup> include:

balance of mass

$$\rho \det \underline{\underline{E}} = \rho_0 \quad (1)$$

balance of angular momentum

$$\underline{\underline{I}} = \underline{\underline{I}}^T \quad (2)$$

balance of linear momentum

$$\operatorname{div} \underline{\underline{I}} + \rho \dot{\underline{b}} = \rho \dot{\underline{a}} \quad (3)$$

and balance of energy

$$\rho \dot{e} = \operatorname{Tr} (\underline{\underline{I}} \underline{\underline{L}}) + \rho r - \operatorname{div} \dot{\underline{q}}. \quad (4)$$

These equations relate the following seven fundamental fields

$\dot{\underline{x}}(\dot{\underline{x}}, t)$  position vector (5.1)

$\rho(\dot{\underline{x}}, t)$  mass density per unit volume (5.2)

$\underline{\underline{I}}(\dot{\underline{x}}, t)$  stress tensor (5.3)

$\dot{\underline{b}}(\dot{\underline{x}}, t)$  body force vector per unit mass (5.4)

$e(\dot{\underline{x}}, t)$  internal energy per unit mass (5.5)

$r(\dot{\underline{x}}, t)$  heat supply rate per unit mass (5.6)

$\dot{\underline{q}}(\dot{\underline{x}}, t)$  heat conduction vector (5.7)

and the four derived fields

$$\vec{v}(\vec{x}, t) = \frac{d}{dt} \vec{x}(\vec{x}, t) \quad \text{velocity vector} \quad (5.8)$$

$$\vec{a}(\vec{x}, t) = \frac{d}{dt} \vec{v}(\vec{x}, t) \quad \text{acceleration vector} \quad (5.9)$$

$$\underline{F}(\vec{x}, t) = \text{Grad } \vec{x}(\vec{x}, t) \quad \text{deformation gradient tensor} \quad (5.10)$$

$$\underline{L}(\vec{x}, t) = \left[ \frac{d}{dt} \underline{F}(\vec{x}, t) \right] \left[ \underline{F}^{-1}(\vec{x}, t) \right] \quad \text{velocity gradient tensor} \quad (5.11)$$

all expressible as functions of initial position  $\vec{x}$  and time  $t$ . A superposed arrow denotes a vector and a tilde under a quantity denotes a tensor. The superscript T on a tensor denotes the transpose, and the inverse is denoted by the superscript, -1. The operator div refers to the divergence with respect to the spatial position  $\vec{x}$ , and Grad is the gradient with respect to  $\vec{x}$ . The operator det refers to the determinate and a superimposed dot denotes the total derivative with respect to time. The initial mass density is denoted by  $\rho_0$ . In addition, these fields are related by whichever constitutive equations describe the response of the various materials and by the appropriate initial conditions and boundary conditions. Various forms of the constitutive equations are considered later.

At surfaces of discontinuity (e.g., shock fronts), these equations are augmented by jump conditions. For a shock or a detonation wave with local normal  $\vec{n}$  moving at speed  $U$  into an undeformed and unstressed material, the following equations apply:

$$\text{mass: } \rho_0 U = \rho U - \rho(\vec{v} \cdot \vec{n}) \quad (6)$$

$$\text{momentum: } \vec{In} + \rho_0 U \vec{v} = 0 \quad (7)$$

$$\text{energy: } \rho_0 U(e - e_0 + \frac{1}{2} \vec{v} \cdot \vec{v} - Q) + \vec{n} \cdot \underline{I} \vec{v} = 0 \quad (8)$$

and a compatibility condition

$$U(\mathcal{E} - I)\vec{n} + \vec{v} = 0 \quad (9)$$

where  $I$  is the identity tensor and the variables  $\rho$ ,  $\vec{v}$ ,  $\mathcal{I}$ ,  $e$ ,  $\mathcal{E}$  refer to the properties behind the shock,  $Q$  is the energy per unit mass added at the jump for a detonation wave,  $e_0$  and  $\rho_0$  are the energy and density in the undeformed material ahead of the wave.

Two different solutions to the entire set of eqs. 1 through 9 are to be compared. All of the quantities associated with the second solution will be denoted by primes. These two solutions are said to be similar if the following relationships

$$\vec{x}'(\vec{x}', t') = \alpha_x \vec{x}(\vec{x}, t) \quad (10.1)$$

$$\rho'(\vec{x}', t') = \alpha_\rho \rho(\vec{x}, t) \quad (10.2)$$

$$\mathcal{I}'(\vec{x}', t') = \alpha_{\mathcal{I}} \mathcal{I}(\vec{x}, t) \quad (10.3)$$

$$\vec{b}'(\vec{x}', t') = \alpha_b \vec{b}(\vec{x}, t) \quad (10.4)$$

$$e'(\vec{x}', t') = \alpha_e e(\vec{x}, t) \quad (10.5)$$

$$r'(\vec{x}', t') = \alpha_r r(\vec{x}, t) \quad (10.6)$$

$$\vec{q}'(\vec{x}', t') = \alpha_q \vec{q}(\vec{x}, t) \quad (10.7)$$

$$Q'(\vec{x}', t') = \alpha_Q Q(\vec{x}, t) \quad (10.8)$$

hold at homologous points defined by

$$\vec{x}' = \alpha_x \vec{x} \quad (10.9)$$

for homologous time

$$t' = \alpha_t t. \quad (10.10)$$

The derived fields are related as a consequence of their definitions by

$$\vec{v}'(\vec{x}', t') = \frac{\alpha_x}{\alpha_t} \vec{v}(\vec{x}, t) \quad (11.1)$$

$$\vec{a}'(\vec{x}', t') = \frac{\alpha_x}{(\alpha_t)^2} \vec{a}(\vec{x}, t) \quad (11.2)$$

$$\vec{E}'(\vec{x}', t') = \frac{\alpha_x}{\alpha_t} \vec{E}(\vec{x}, t) \quad (11.3)$$

$$\vec{L}'(\vec{x}', t') = \frac{1}{\alpha_t} \vec{L}(\vec{x}, t). \quad (11.4)$$

Here the ten various quantities  $\alpha_i$  are constants called scale factors. Note that if  $\alpha_x = \alpha_x$  in both solutions, the reference position  $\vec{x}$  is the initial position:  $\vec{x}(t = 0) = \vec{x}$ . This is henceforth assumed, leaving nine independent scale factors. Thus, in particular, eq. 11.3 states that the deformation gradient must be the same at homologous points and therefore the strains are identical also. In more detailed terminology, the two solutions are said to be geometrically, kinematically and dynamically similar.<sup>15</sup>

The question of the existence of two different solutions related by these similarity requirements is to be investigated. Both sets of solutions must satisfy the balance equations given above, regardless of the constitutive equations. This requirement will give certain restrictions relating the nine scale factors. Additional restrictions from specific constitutive equations are derived separately below.

Assume that a primed solution exists and substitute the primed fields into the balance equations 1 through 4 using the similarity relationships (eqs. 10.1 - 10.10) to get

$$\alpha_p \rho \det \vec{E} = \alpha_p \rho_0 \quad (12.1)$$

$$\alpha_T \underline{I} = \alpha_T \underline{I}^T \quad (12.2)$$

$$\frac{\alpha_T}{\alpha_x} \operatorname{div} \underline{I} + \alpha_p \alpha_b \rho \vec{b} = \frac{\alpha_p \alpha_x}{\alpha_t^2} \rho \vec{a} \quad (13)$$

$$\frac{\alpha_p \alpha_e}{\alpha_t} \rho \vec{e} = \frac{\alpha_T}{\alpha_t} \operatorname{Tr}(\underline{I} \underline{L}) + \alpha_p \alpha_r \rho r - \frac{\alpha_q}{\alpha_x} \operatorname{div} \vec{q}. \quad (14)$$

The unprimed fields must also satisfy the balance equations. Hence equations 12.1 and 12.2 are satisfied identically.

For the balance of linear momentum, eq. 3 can be used for  $\operatorname{div} \underline{I}$  in eq. 13, giving

$$\left[ \frac{\alpha_T}{\alpha_x} - \frac{\alpha_p \alpha_x}{(\alpha_t)^2} \right] \rho \vec{a} = \left[ \frac{\alpha_T}{\alpha_x} - \alpha_p \alpha_b \right] \rho \vec{b}. \quad (15)$$

This must hold for all  $\vec{x}$  and  $t$ . Thus, unless the acceleration field  $\vec{a}$  is itself a scalar multiple of the body force  $\vec{b}$  or either  $\vec{a}$  or  $\vec{b}$  is identically zero, it is necessary that

$$\frac{\alpha_T}{\alpha_x} = \frac{\alpha_p \alpha_x}{(\alpha_t)^2} \quad (16)$$

and

$$\frac{\alpha_T}{\alpha_x} = \alpha_p \alpha_b. \quad (17)$$

The most common body force per unit mass is a constant vector proportional to a constant gravity,  $g$ . In this case, any acceleration field which is a scalar multiple of  $\vec{b}$  is at most a rigid body motion. If  $\vec{b} = 0$ , then eq. 17 is not required. If  $\vec{a} = 0$ , as in statics, then eq. 16 is not required.

Now substitute  $\rho \dot{e}$  from the balance of energy eq. 4 into eq. 14 to get

$$\left( \frac{\alpha_p \alpha_e}{\alpha_t} - \frac{\alpha_T}{\alpha_t} \right) \text{Tr } \mathbf{T} \mathbf{L} + \left( \frac{\alpha_p \alpha_e}{\alpha_t} - \alpha_p \alpha_r \right) \rho r - \left( \frac{\alpha_p \alpha_e}{\alpha_t} - \frac{\alpha_q}{\alpha_x} \right) \text{div } \vec{q} = 0 \quad (18)$$

for all  $\vec{x}$  and  $t$ . Again, assuming the various fields in eq. 18 are neither identically zero nor simple scalar multiples of a common field, it is necessary that

$$\alpha_p \alpha_e = \alpha_T \quad (19)$$

$$\frac{\alpha_e}{\alpha_t} = \alpha_r \quad (20)$$

$$\frac{\alpha_p \alpha_e}{\alpha_t} = \frac{\alpha_q}{\alpha_x} \quad (21)$$

Requirements brought about by detonation waves in the explosive can now be included. For this case, both solutions must also satisfy the jump conditions across the wave (eqs. 6-9). An analysis identical to that just given for the balance equations produces only one additional restriction which involves the scale factor  $\alpha_Q$  for the specific energy of the explosive  $Q$

$$\alpha_Q = \frac{\alpha_T}{\alpha_p} \quad (22)$$

Altogether then, the balance equations plus the jump conditions provide six similarity restrictions among the nine scale factors relating the variable fields as defined by eqs. 10.1 through 10.10. Eqs. 16 and 17 are a consequence of the balance of momentum, and eqs. 19, 20 and 21 result from the balance of energy, and the energy jump condition supplies the remaining constraint, eq. 22. The balance of mass and the balance of angular momentum provide no restrictions.

It is convenient for the present application to consider  $\alpha_x$ ,  $\alpha_t$  and  $\alpha_p$  as independent. The six restrictive conditions (eqs. 16-22) can then be used to solve for the remaining scale factors:

$$\alpha_T = \alpha_p \left( \frac{\alpha_x}{\alpha_t} \right)^2 \quad (23.1)$$

$$\alpha_b = \alpha_x / (\alpha_t)^2 \quad (23.2)$$

$$\alpha_e = \left( \frac{\alpha_x}{\alpha_t} \right)^2 \quad (23.3)$$

$$\alpha_r = (\alpha_x)^2 / (\alpha_t)^3 \quad (23.4)$$

$$\alpha_q = \alpha_p \left( \frac{\alpha_x}{\alpha_t} \right)^3 \quad (23.5)$$

$$\alpha_Q = \left( \frac{\alpha_x}{\alpha_t} \right)^2 \quad (23.6)$$

Therefore it can be seen that, considering only the balance equations and the jump conditions, nontrivial similar solutions are allowed with arbitrary scaling of size, time and density. The six remaining scale factors must then satisfy the six equations, 23.1 through 23.6.

## 2-2 ANALYSIS OF SPECIFIC CONSTITUTIVE EQUATIONS

In addition to the balance equations and the jump equations given above, the complete solution for the deformation and flow of any continuous medium depends on the constitutive equations that describe the behavior of that medium. Therefore, while the above similarity requirements (eqs. 23.1 through 23.6) are necessary, the question of their sufficiency has not been answered. Note, however, that they are general and apply to all materials.

The nature and type of equations that describe the material behavior for a given medium and their role in determining similarity requirements is now considered. In order to obtain all constraints due to the constitutive equations, it is necessary to consider various types of such equations to ensure that the complete set of equations, balance and constitutive, give a well-posed problem in a mathematical sense. That is, there should exist unique solutions when appropriate initial and boundary conditions are given. However, the question of uniqueness and existence of solutions to this complete set of equations cannot be answered at any level of generality. Thus, the study of well-known classical theories is utilized where experience has shown that unique solutions do exist.

A first special case considers the mechanical deformation of a linearly compressible hydrostatic medium. All thermodynamic fields are omitted. The stress tensor  $\underline{\underline{\sigma}}$  is assumed to have no shear stress components and is therefore described by the pressure  $p$  and the identity tensor  $\underline{\underline{I}}$ ,

$$\underline{\underline{\sigma}} = -p \underline{\underline{I}} \quad (24)$$

The pressure  $p$  is assumed to depend linearly on the density change

$$p = K_0 (1 - \rho_0 / \rho) \quad (25.1)$$

where  $\rho_0$  is the initial density at zero pressure and  $K_0$  is the bulk modulus. Two different experiments, designated as the primed and the unprimed, are to be compared. Each of these may be in a different material, but each material is modeled by the linearly compressible equation given above. Consequently, for the primed material

$$p' = K_0' (1 - \rho_0' / \rho'). \quad (25.2)$$

Are these two constitutive equations (25.1 and 25.2) consistent with the similarity requirements given by eqs. 23.1 through 23.6, or do they introduce additional restrictions? The answer is easily seen. Since the pressures  $p$  and  $p'$  are related by the parameter  $\alpha_T$  which satisfies eq. 23.1, it

is necessary that the bulk moduli be related by  $\alpha_T$  also

$$\alpha_T = \frac{K_0' (1-p_0'/\rho')}{K_0 (1-p_0/\rho)} = \frac{K_0'}{K_0} = \alpha_p \left( \frac{\alpha_x}{\alpha_t} \right)^2 \quad (26.1)$$

since

$$p_0'/\rho' = \frac{\alpha_p p_0}{\alpha_p \rho} = p_0/\rho \quad (26.2)$$

Therefore, similarity is certainly possible in this case. If the two materials are indeed different, and the two experiments have different distance, time, and density scale factors, then the bulk moduli of the two materials must satisfy the requirement given by eq. 26.1. For two experiments conducted in the same material ( $\alpha_p = 1$  and  $K_0' = K_0$ ), eq. 26.1 can be satisfied only if  $\alpha_t = \alpha_x$ , leaving only one independent similarity parameter, the size scale factor  $\alpha_x$ . From this and eqn. 23.1, the stress and the strain must be the same at homologous points in the two experiments. Hence dynamically similar experiments of different size scale, arbitrary  $\alpha_x = \alpha_t$ , in the same same linearly compressible hydrostatic material must have the following scale factors

$$\alpha_T = 1 \quad (27.1)$$

$$\alpha_b = 1/\alpha_x \quad (27.2)$$

A second example, a calorically perfect heat-conducting gas, illustrates how additional constraints are introduced based upon simple thermodynamic behavior. The stress is again hydrostatic, but in this case the pressure is given by a perfect gas law

$$p = (\gamma-1) \rho e \quad (28)$$

where  $\gamma$  is the perfect gas constant. The heat conduction is assumed to satisfy Fourier's law

$$\vec{q} = -k \text{ grad } \theta \quad (29)$$

where  $\theta$  is the temperature field and  $\text{grad}$  denotes the gradient with respect to the spatial coordinates. Further assume that the internal energy  $e$  and temperature  $\theta$  are related by a constant specific heat  $C_v$  as

$$e = C_v \theta. \quad (30)$$

The heat conduction can then be rewritten in terms of the conductivity  $k$  and the gradient of the internal energy

$$\vec{q} = - \frac{k}{C_v} \text{grad } e. \quad (31)$$

Equations 28 and 31 can be taken as the fundamental constitutive equations, eliminating the need to consider the temperature field. Both eq. 28 and eq. 31 must be compatible with the requirements given by eqs. 23.1 through 23.6. Equation 28 together with eqs. 23.1 and 23.3 give

$$\frac{(\gamma - 1)}{(\gamma' - 1)} = \frac{p}{p'} \frac{p' e'}{p e} = \frac{\alpha_p \alpha_e}{\alpha_T} = 1. \quad (32)$$

Therefore, similarity is impossible unless both experiments are conducted in materials having the same value for the perfect gas constant. This is a well known result in fluid mechanics.<sup>16</sup> Further similarity restrictions on material properties can be obtained using eq. 10.7.

$$\vec{q}' = - \frac{k'}{C_v} \text{grad}' e' = \alpha_q \vec{q} \quad (33)$$

where  $\text{grad}'$  denotes the gradient with respect to  $x'$ . Using eqs. 10.1, 10.5 and 23.3

$$\frac{\text{grad}' e'}{\text{grad } e} = \frac{\alpha_e}{\alpha_x} = \frac{\alpha_x}{(\alpha_t)^2} \quad (34)$$

so that using eqs. 31, 33 and 23.5

$$\left( \frac{k'}{k} \right) \left( \frac{C_v}{C_v} \right) = \alpha_p \frac{(\alpha_x)^2}{\alpha_t} \quad (35)$$

providing an additional similarity requirement.

Equation 35 can be rewritten as follows

$$\left(\frac{k'}{\rho' c_v'}\right) \left(\frac{\rho c_v}{k}\right) = \frac{v' \ell'}{v \ell} \quad (36)$$

using the scale factor for the magnitude of the characteristic velocities  $v$  and  $v'$  (eq. 11.1)

$$\frac{\alpha_x}{\alpha_t} = \frac{v'}{v} \quad (37.1)$$

and the scale factor for characteristic sizes  $\ell$  and  $\ell'$

$$\alpha_x = \frac{\ell'}{\ell} \quad (37.2)$$

Substituting another perfect gas relationship,  $c_v = c_p/\gamma$  and using  $\gamma = \gamma'$  from eq. 32 gives

$$\frac{\rho v \ell c_p}{k} = \frac{\rho' v' \ell' c_p'}{k'} \quad (38)$$

This ratio, the product of the Reynolds number and the Prandtl number referred to as the Péclet number,<sup>17</sup> must be equal at homologous points in the two flows.

The sound speeds in the two different perfect gas media are given by

$$c^2 = \gamma \frac{p}{\rho} \quad (39.1)$$

and

$$c'^2 = \gamma' \frac{p'}{\rho'} \quad (39.2)$$

Now using eq. 23.1, the similarity requirement for stress

$$\frac{p'}{p} = \alpha_T = \alpha_\rho \left( \frac{\alpha_x}{\alpha_t} \right)^2 \quad (40)$$

and the scale factor for density  $\alpha_\rho$ , the ratio of sound speeds can be written

$$\left(\frac{c'}{c}\right)^2 = \frac{\gamma'}{\gamma} \frac{p'}{p} \frac{\rho}{\rho'} = \frac{\gamma'}{\gamma} \left(\frac{\alpha_x}{\alpha_t}\right)^2 \quad (41)$$

Using eq. 36.1 for the velocity ratio gives

$$\left(\frac{v}{c}\right)^2 = \frac{\gamma'}{\gamma} \left(\frac{v'}{c'}\right)^2. \quad (42)$$

Therefore, eq. 32 which requires  $\gamma = \gamma'$  leads to the further requirement that Mach number be equal at homologous points. In this example, had viscosity been included, separate requirements on the Reynolds number and the Prandtl number would have also been obtained<sup>16</sup> in place of the requirements on Péclet number given by eq. 38.

A further reduction occurs if it is now assumed that each of the two similar experiments is in fact conducted in the same material. Then the same material properties apply for each material,  $\alpha_p = 1$ , and eq. 35 for material equivalence gives

$$\alpha_t = (\alpha_x)^2 \quad (43)$$

The six dependent scale factors are then given by

$$\alpha_T = 1/(\alpha_x)^2 \quad (44.1)$$

$$\alpha_b = 1/(\alpha_x)^3 \quad (44.2)$$

$$\alpha_e = 1/(\alpha_x)^2 \quad (44.3)$$

$$\alpha_r = 1/(\alpha_x)^4 \quad (44.4)$$

$$\alpha_q = 1/(\alpha_x)^3 \quad (44.5)$$

$$\alpha_Q = 1/(\alpha_x)^2 \quad (44.6)$$

where the size scale factor  $\alpha_x$  is arbitrary. Note that stress, body forces, internal energy, radiation and heat conduction all scale with various factors based upon the size scale factor  $\alpha_x$ .

The requirement of equation 44.6 implies that, in experiments with explosives, the heat of detonation  $Q$  cannot be the same in two similar experiments. However, consistent with the assumptions given above, and insofar as the thermodynamical constitutive equations stated must also apply to the explosive, the two experiments must have the same thermodynamic material properties for the explosives. These two requirements are in practice mutually exclusive. This conflict arose because of the inclusion of heat conduction effects. That is, when heat conduction effects are significant in experiments with detonating high explosives, similarity between experiments with different size scales cannot be achieved with the same material.

Having examined these two special examples, more general considerations can now be given. Guided by the last example, it is assumed that heat conduction effects can be ignored. With this restriction, consider the question of the complete characterizataion of a medium such as soil. It is expected that prediction of all aspects of explosive cratering may require concepts of compressibility, nonlinearity, yield, fracture, porosity, cohesion and others. As stated by Truesdell and Noll<sup>18</sup> of the concept of dynamic similarity: "The more complicated the constitutive equation, the greater the number of dimensionless numbers that must be controlled in order to assure dynamical similarity. Ultimately the dimensionless response functional itself must be the same for the two materials in order for scaling to be possible."

In agreement with this statement, a third important special case is considered. (Of course, as the previous examples using simple constitutive equation show, similarity can be achieved in different materials if the constitutive equation is sufficiently simple. This is the case in classical fluid mechanics. There is the possibility of at least approximate similarity of some aspects between different real materials, even when their total behavior is rather complicated.) Suppose two experiments of different size scales are to be conducted in the same material and with the same explosive. In this case, is similarity possible? The answer to this question can be given at a general level. Consider the similarity requirements given by eqs. 23.1 through 23.6 but with the assumption that the same media and the same explosive type are used in both experiments. Furthermore assume that heat conduction effects are not

significant. Then it is necessary that  $\alpha_p = 1$ ,  $\alpha_Q = 1$  and from eq. 23.6,  $\alpha_x = \alpha_t$ . Hence there remains only one independent scale factor  $\alpha_x$  giving

$$\alpha_T = 1 \quad (45.1)$$

$$\alpha_b = 1/\alpha_x \quad (45.2)$$

$$\alpha_e = 1 \quad (45.3)$$

$$\alpha_r = 1/\alpha_x \quad (45.4)$$

$$\alpha_Q = 1 \quad (45.5)$$

Therefore, similarity is indeed possible, as long as the constitutive equations are consistent with this scaling. The stress, the strain, the density, the internal energy and the heat of detonation will be the same at homologous points. The body force and the heat-rate-supply term must scale as the reciprocal of the size, and the scale factors for time and distance are equal. Consequently, if  $\alpha_x = 1/10$  so that a 1/10 size scale experiment is to be performed, the body force must be 10 times larger as must be the heat-supply rate. All events will occur in 1/10 the time over 1/10 the distance, and all velocities will be the same.

It is fairly obvious that a large class of constitutive equations will be compatible with similarity at this level. Any relation between the conserved quantities such as the stress, strain, and internal energy will be directly compatible, no matter how complicated or nonlinear. This includes nonlinear elasticity, plasticity, porosity, spall and fracture, the Mie-Gruneisen equation of state, the so-called Jones-Wikins-Lee (JWL) equation of state used for high explosives, and many others. Only invariance to arbitrary  $\alpha_x$  and  $\alpha_t$  is necessary. Thus, it does not include any constitutive behavior not invariant to size scaling and to time scaling. For example, an equation between stress and rate of strain would not be consistent.

This observation is summarized by the following general statement:  
Complete and exact dynamic similarity can be achieved between two different

experiments of arbitrary size scale in the same material as long as the constitutive behavior is 1) rate independent and 2) has no inherent size properties. Of these two requirements, rate independence is probably the most restrictive. It has already been noted that this rules out heat conduction. It is interesting that the property of rate-independence emerges as the significant property that allows non-trivial similarity in very general materials. Whether this restriction is of practical importance, and if so, for which materials, can only be answered by experimentation.

### 2-3 DIMENSIONLESS PARAMETERS

The results of the previous sections can be used to generate dimensionless parameters enabling direct definition and comparison of similar experiments. In particular, the tests in question are to determine the final apparent crater formed by the detonation of a spherical explosive buried in a homogeneous soil. The volume of the crater is determined by the motion history  $\hat{x}(\hat{x}, t)$ . This history is itself determined by the complete set of equations, balance, jump and constitutive, together with the appropriate initial and boundary conditions.

It is recognized that the behavior of the soil is complex and requires complex constitutive equations. Thus it is probable that similarity will not be achieved unless the same soil is used for similar experiments. With this restriction, as shown in the previous sections, similarity is possible assuming only that the constitutive equations describing the soil are independent of the scale factors for size and for time.

A very general class of mechanical constitutive equations are those which Truesdell and Noll<sup>13</sup> have called simple materials. These include all materials for which the stress tensor at any material point at the present time is determined by the past history of the strain at that point. This includes all types of non-linear elastic, elastic-plastic, and visco-elastic materials, whether solid or fluid.

Truesdell and Noll<sup>18</sup> have shown that the complete set of material constants characterizing a simple material can involve only constants that are

dimensionless, or have units of stress or time. If a restriction to rate-independent materials is made, only dimensionless or stress-unit constants can remain. This level of generality still includes all aspects of nonlinear elasticity, rate independent elastic-plastic, and rate independent fracture of any type. It is assumed that the constitutive equations for the soil are included in this general class of constitutive equations.

The explosive is assumed to be modeled by the classical Chapman-Jouget theory, where the combustion products behave as a perfect gas.

With these assumptions a list of pertinent parameters can be given. The explosive behavior is determined by

$Q$  - the heat of detonation per unit mass  
 $\delta$  - the initial density of the explosive.

The soil is characterized by

$\rho$  - the initial soil density  
 $Y$  - a material strength parameter.

The possibility of similarity between different soils will be included in the following analysis. As discussed above, all material properties of the soil are either dimensionless or have units of stress. The material strength  $Y$  listed here is assumed to have stress units. The inclusion of all remaining material constants, whatever their number, will not change any of the arguments to follow and therefore are not included. The perfect gas constant  $r$  for the explosive products is omitted for the same reason. This point will be clarified subsequently.

The ambient air is not considered, and the initial geometry is determined by

$a$  - the explosive charge radius  
 $d$  - the depth of burial

In addition, the solution depends on the body force arising from

$g$  - gravity.

The scale factors for all variables including the above independent parameters are determined by the three independent scale factors  $\alpha_x$ ,  $\alpha_t$ , and  $\alpha_p$ , as in eqs. 23.1-23.6. These three scale factors can be expressed in terms

of the actual physical parameters of the two experiments to be compared. For example

$$a' = \alpha_x a \quad (46.1)$$

so that

$$\alpha_x = \frac{a'}{a} \quad (46.2)$$

Since the mass  $W$  of explosive is given by

$$W = \left(\frac{4\pi}{3}\right) \delta a^3 \quad (46.3)$$

eq. 46.2 can be rewritten as

$$\alpha_x = \left(\frac{W' \delta'}{W \delta}\right)^{1/3} \quad (46.4)$$

Likewise the mass density at each point in the model experiment is related to the full-scale experiment by  $\alpha_\rho$ . Hence  $\rho' = \alpha_\rho \rho$  and  $\delta' = \alpha_\rho \delta$ , giving

$$\alpha_\rho = \frac{\rho'}{\rho} = \frac{\delta'}{\delta} \quad (47.1)$$

Hence eq. 46.4 can also be written

$$\alpha_x = \left(\frac{W' \rho'}{W \rho}\right)^{1/3} \quad (47.2)$$

It is now convenient to determine  $\alpha_t$  in terms of the specific energy  $Q'$  and  $Q$  of the explosives used for the two experiments. In particular,

$$Q' = \alpha_Q Q \quad (48)$$

so that using eqs. 23.6 and 46.4

$$\frac{Q'}{Q} = \alpha_Q = \left(\frac{\alpha_x}{\alpha_t}\right)^2 = \left(\frac{W' \delta'}{W \delta}\right)^{2/3} \left(\frac{1}{\alpha_t}\right)^2 \quad (49)$$

Solving for  $\alpha_t$ ,

$$\alpha_t = \left( \frac{W' \delta}{W \delta'} \right)^{1/3} \left( \frac{Q}{Q'} \right)^{1/2} \quad (50)$$

The scale factors for the other variables can now be determined. Volumes  $V'$  and  $V$  are related by the cube of the scale factor for distance given by eq. 47.2

$$V' = (\alpha_x)^3 V = \frac{W' \rho}{W \rho'} V \quad (51)$$

which leads to the definition of a dimensionless parameter, referred to as a  $\pi$ -group, relating the variables in each experiment

$$\frac{V' \rho'}{W'} = \frac{V \rho}{W} = \pi_1 \quad (52)$$

For any two similar experiments  $\pi_1$  must have the same value. Scale factors for the remaining independent parameters of interest in the two experiments under comparison can also be expressed in terms of the three scale factors  $\alpha_x$ ,  $\alpha_\rho$  and  $\alpha_t$  given by eqs. 47.2, 47.1 and 50. Using eqs. 10.4, 23.2 and 46.4, the scale factor for gravity is

$$g' = \alpha_b g = \frac{\alpha_x}{(\alpha_t)^2} g = \left( \frac{W \delta'}{W' \delta} \right)^{1/3} \frac{Q'}{Q} g \quad (53)$$

This leads to the definition of a second  $\pi$ -group

$$\frac{g'}{Q'} \left( \frac{W'}{\delta'} \right)^{1/3} = \frac{g}{Q} \left( \frac{W}{\delta} \right)^{1/3} = \pi_2 \quad (54)$$

The depth of burial for the two experiments satisfies eq. 10.1

$$d' = \alpha_x d = \left( \frac{W' \delta}{W \delta'} \right)^{1/3} d \quad (55)$$

so let

$$d' \left( \frac{\delta'}{W'} \right)^{1/3} = d \left( \frac{\delta}{W} \right)^{1/3} = \pi_3 \quad (56)$$

The density of the explosive satisfies eq. 10.2,

$$\delta' = \alpha_p \delta = \frac{\rho'}{\rho} \delta \quad (57)$$

as used in eq. 47.1, hence let

$$\frac{\rho'}{\delta'} = \frac{\rho}{\delta} = \pi_4. \quad (58)$$

The material strength parameter  $\gamma$  has stress units. As a consequence, it must transform between the two experiments with the scale factor  $\alpha_T$ :

$$\frac{\gamma'}{\gamma} = \alpha_T = \alpha_p \left( \frac{\alpha_x}{\alpha_t} \right)^2 \quad (59)$$

Using eqs. 46.4, 47.1 and 50

$$\frac{\gamma'}{\gamma} = \frac{\delta' Q'}{\delta Q} \quad (60)$$

The appropriate  $\pi$ -group is given by

$$\frac{\gamma'}{\delta' Q'} = \frac{\gamma}{\delta Q} = \pi_5 \quad (61)$$

All remaining parameters that have been identified are either dimensionless or have units of stress. For example, dimensionless constants include the perfect gas constant  $R$  of the explosive products or dimensionless material constants for the soil. These dimensionless constants can be easily shown to be required to have the same value in similar experiments. Each such parameter defines an additional  $\pi$ -group. Those that have stress units will lead to  $\pi$ -groups that are ratios of the additional parameters to the variable  $\gamma$  identified above. Ultimately the discussion will be restricted to experiments using the same soil. For this case, all additional soil material property  $\pi$ -groups are constant for an entire series of experiments, and there is no need to include them specifically.

The relationships among the scale factors, eqs. 23.1-23.6, applied to the eight parameters, seven independent and one dependent, of a cratering experiment require that the five independent  $\pi$ -groups,  $\pi_1$  through  $\pi_5$ , each have the same value for similar experiments. Conversely, similarity between two

experiments will be achieved when these five  $\pi$ -groups are the same for the two experiments, at least insofar as the original list of seven independent variables is complete. Any additional independent variable will give an additional  $\pi$ -group which must also be the same. These  $\pi$ -groups allow the design of a subscale experiment to model a given full-scale event. Arbitrary values of  $a$ ,  $\rho$  and  $Q$  can be chosen or equivalently, values for the scale factors  $\alpha_x$ ,  $\alpha_y$ , and  $\alpha_z$ . Then there is a subscale similar experiment, having the same values for each of the five  $\pi$ -groups as does the full-scale event.

The original list of eight variables is not independent. The volume  $V$  has previously been identified as depending upon the other seven. Thus the following relationship can be written

$$V = F(g, d, \delta, Y, r, a, Q) \quad (62.1)$$

By using a simple change of variables, eq. 62.1 can be rewritten in terms of the five  $\pi$ -groups,  $\rho$ ,  $a$  and  $Q$

$$\pi_1 = \mathcal{F}(\pi_2, \pi_3, \pi_4, \pi_5, r, a, Q) \quad (62.2)$$

However, as noted above, a given full-scale event can be modeled with a similar experiment for any values of  $\rho$ ,  $a$  and  $Q$  whatsoever. As a consequence, there exists a whole family of similar experiments, where  $\rho$ ,  $a$  and  $Q$  may take on any values whatsoever, and for which  $\pi_1$  through  $\pi_5$  are the same. Thus it can be concluded that  $\rho$ ,  $a$  and  $Q$  can be varied at will, but as long as  $\pi_2$  through  $\pi_5$  are held constant, then  $\pi_1$  must also be constant and depend, at most, upon the other  $\pi$ -groups. Therefore eq. 62.2 can be rewritten

$$\pi_1 = \mathcal{F}(\pi_2, \pi_3, \pi_4, \pi_5) \quad (62.3)$$

where

$$\pi_1 = \frac{V\rho}{W} \quad (63.1)$$

$$\pi_2 = \frac{g}{Q} \left( \frac{W}{\delta} \right)^{1/3} \quad (63.2)$$

$$\pi_3 = d \left( \frac{\delta}{W} \right)^{1/3} \quad (63.3)$$

$$\pi_4 = \rho/\delta \quad (63.4)$$

$$\pi_5 = \frac{Y}{\delta Q} \quad (63.5)$$

Therefore, if  $\pi_2$  through  $\pi_5$  are controlled so that they individually have the same value in two experiments, then similarity is achieved and the group  $\pi_1$  will also have the same value. In this way, the volume of a crater in a large-scale experiment can be determined by performing a small-scale similar experiment, and the scale factors on all parameters are determined by the choice of the three parameters  $\rho$ ,  $a$ ,  $Q$ .

An important special case arises when experiments are conducted in the same soil and with the same explosive. Then both  $\pi_4$  and  $\pi_5$  are constant for the experiments as would any additional  $\pi$ -group for the soil and the explosive giving

$$\pi_1 = \mathcal{Y}(\pi_2, \pi_3) \quad (64)$$

Having picked the size scale factor by choosing charge size, only the depth of burial  $d$  and the gravity  $g$  need to be controlled in order to ensure similarity. For surface bursts (zero depth of burial),  $\pi_3 = 0$  and

$$\pi_1 = \mathcal{Y}(\pi_2) \quad (65)$$

This relation contains all the information about the volume of a crater for a given charge in a given medium. Fixing the value of  $\pi_2$  uniquely determines the value of  $\pi_1$  and the experiments are similar. However, to determine the function  $\mathcal{Y}$ , a set of nonsimilar experiments with various values of  $\pi_2$  must be performed. It is important to note that  $\pi_2$  can be varied either by changing the charge size at fixed  $g$  or by varying  $g$  for a fixed charge size. That is, with variations of gravity alone, using a charge size to suit laboratory experiments, the dependence of volume on charge size can be fully determined using the  $\pi$ -group representation. The additional dependence on  $g$  can also be determined by experiments of this type. The problem of determining

to other dependences upon the non-dimensional groups  $\pi_4$  and  $\pi_5$  and any others of consequence. This illustrates the significance of being able to vary the gravity field strength in cratering experiments.

## SECTION 3 EXPERIMENTAL TECHNIQUE

### 3-1 CENTRIFUGE DESCRIPTION

The Boeing 600 G centrifuge was used in this study. This machine has a dynamic load rating of 60,000 G-kg (66 G-tons) at 620 rpm and was constructed using the aerodynamic housing and main shaft assembly from a Gyrex Model 2133 centrifuge. The rotor was designed and fabricated by the Boeing Company to incorporate symmetric swing baskets allowing testing of non-cohesive soil materials. The arm radius to the fully extended base plate is 139.7 cm with a maximum payload mass of 250 kg on each rotor end. An overall view is shown in Fig. 1 and the details of the swing basket and soil sample container are shown in Fig. 2.

The centrifuge is powered by a 30 horsepower Eaton Dynamatic Model ACM-326-910B drive unit incorporating an adjustable speed, constant torque eddy-current clutch. The unit also has electrical dynamic braking allowing shut-down from maximum rpm in less than 30 seconds. The constant output speed motor and variable drive unit are shock mounted and coupled to the main shaft with a belt to minimize vibration.

The rotor shaft is equipped with 24 slip rings for instrumentation channels, three 220 V.a.c. power slip rings and a hydraulic slip ring which can accommodate either gas or liquid. A pair of motor driven Nikon F2 35-mm still cameras are hub mounted in a stereo configuration. These cameras provide stereophoto coverage of one rotor end with a maximum framing rate of six per second. Since the cameras are mounted at an average radius of 13 cm, they experience centripetal accelerations of up to 60 G at maximum rpm. Semiautomatic single framing is not affected by this loading, however in the continuous motor drive mode, shutter speeds fall out of calibration above 350 rpm (approximate camera loading of 18 G).

This camera installation is under continuing development. In this program it provided a system capable of dynamic stereophoto mapping in the event

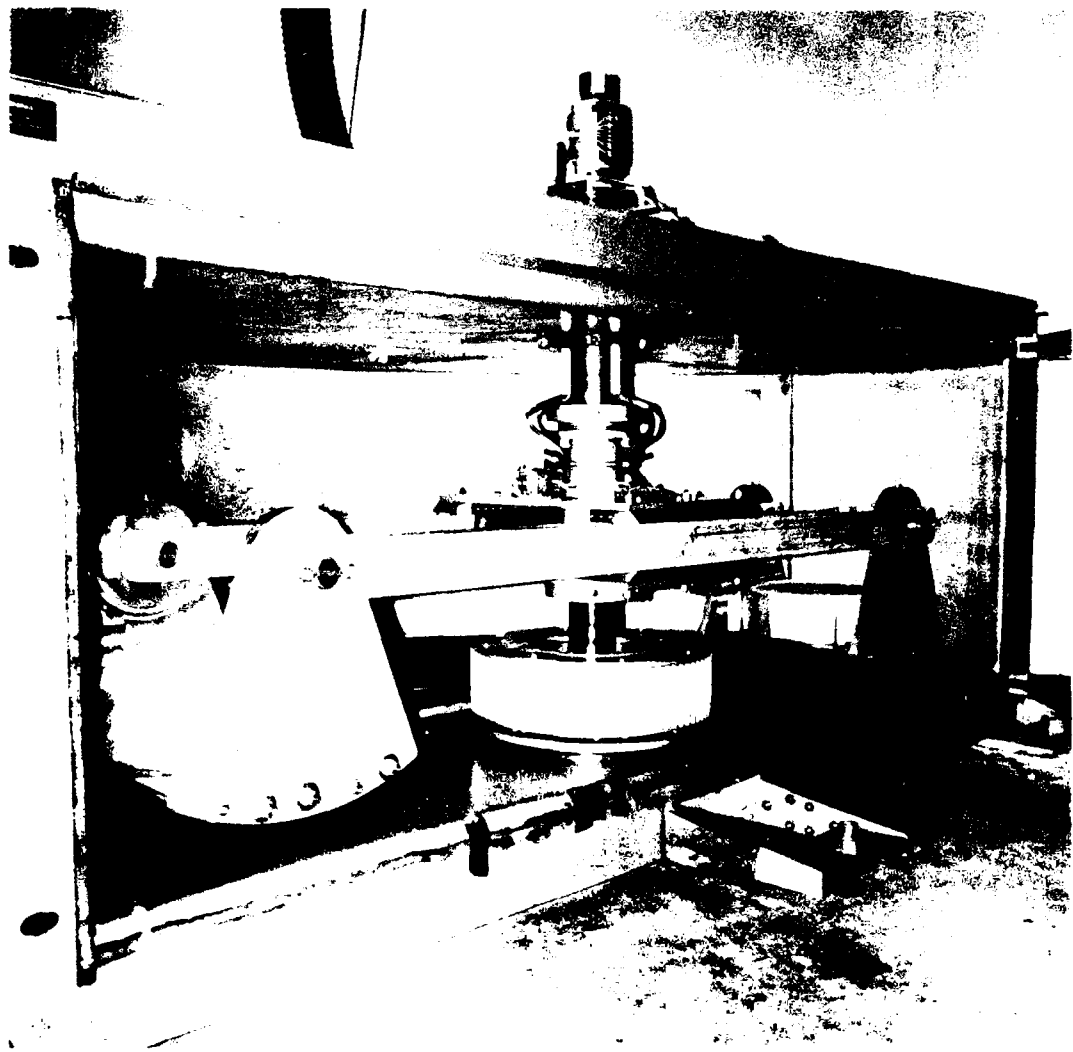


Figure 1. Boeing 600 G centrifuge.

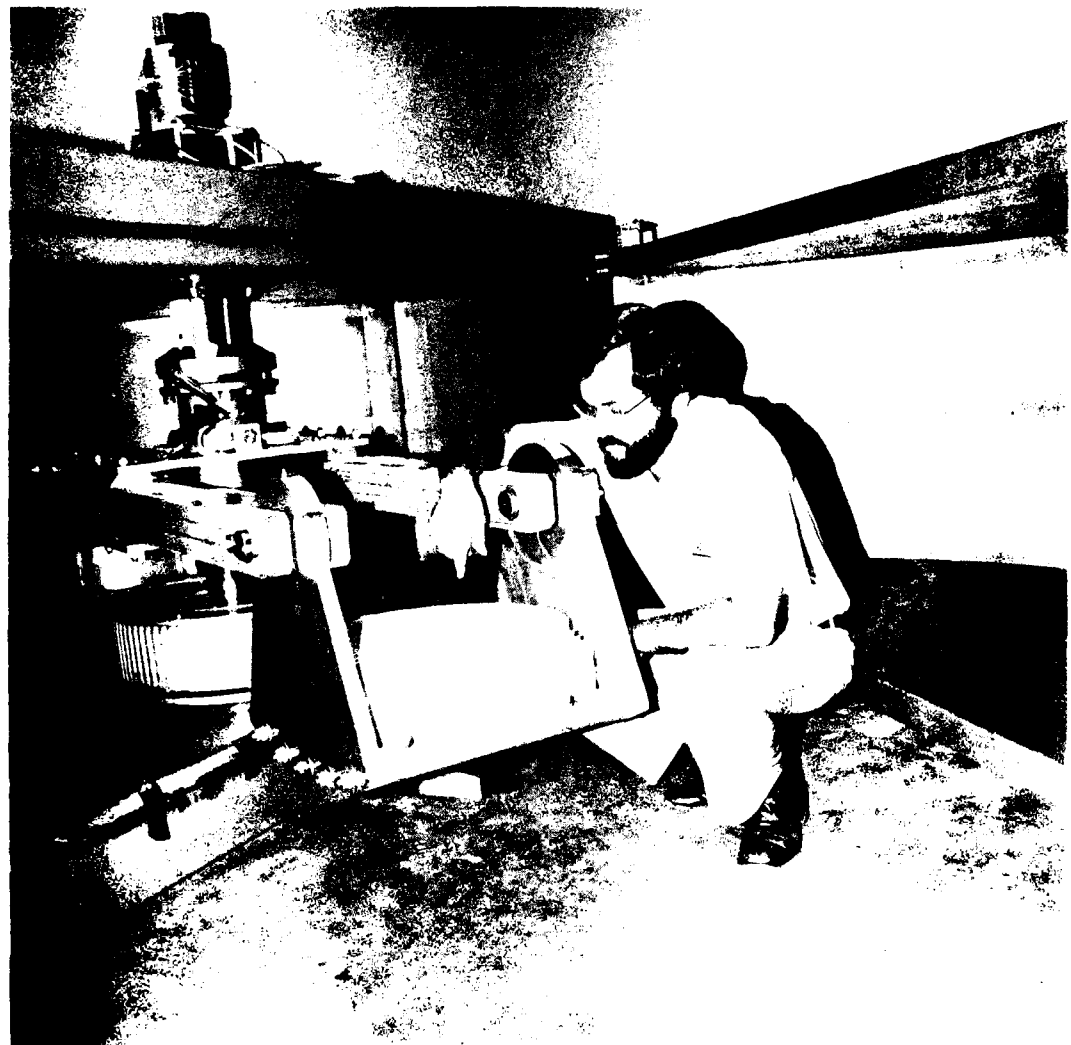


Figure 2. Swing basket showing details of soil containers.

that the formed craters proved to be unstable due to slumping, vibration or windage. For the soil materials tested this was not the case and the cameras were used to confirm earlier tests in which pre-formed craters were spun up successively to check for possible shape changes.

A data reduction technique for stereophotogrammetry was developed for these non-metric cameras under static conditions using object space calibration marks on the soil sample container. The details of this method which are directly applicable to the dynamic system are given in Appendix D. Figs. D1 and D2 show the on-board camera installation in the rotor hub. A 600 watt quartz-halogen lamp provides adequate illumination for films having speed of ASA 125 or greater.

### 3-2 EXPLOSIVE CHARGE DESIGN

To test the hypothesis that increased gravity could be used to scale energy, various explosive charge sizes and materials were required for experiments to be performed at different G levels. The choice of explosive device was influenced by the work of Piekutowski,<sup>5,6</sup> who reported very satisfactory performance from precision devices supplied by the R. Stresau Laboratories, Inc., of Spooner, Wisconsin. For the present work, four different charge sizes were employed. These included the two basic charge sizes used by Piekutowski (1.70-gm lead azide and 0.49-gm PETN) and two larger sizes.

The 0.49-gm composite PETN charge, designated CICS-5 by Stresau consists of two halves of a concentric sphere of PETN pressed around a silver azide initiator, designated CISAS-5. The silver azide is a sphere with radius 0.198 cm. It consists of a maximum amount of 0.130 grams of explosive centrally initiated using a notched 0.0127-cm-diameter tungsten wire to form a spark gap when energized by an electric current. The actual weight of PETN in this device is a nominal 0.360 gram.

The two larger sizes use the same silver-azide initiator with greater amounts of PETN pressed into a concentric spherical configuration. The larger of the two, designated CICS-4, has a total mass of 4.08 gm, approximately an order of magnitude greater than Piekutowski's basic 0.49-gm PETN charge. This

device contains a nominal amount of 3.960 gm of PETN pressed to a nominal density of 1.70 gm/cc. The other composite charge, designated CICS-1.265 contains a nominal 1.22 gm of PETN and has a total mass of 1.34 gm.

The actual charge weights recorded in Appendices A and B are those provided by the R. Stresau Laboratory. It was not possible to confirm these after delivery due to unknown amounts of binder and surface lacquer that are used in fabrication. In addition, it should be noted that the weight of the silver azide in the detonator could vary because of a surface condition in the mold. The silver-azide weight could be as low as 0.120 gm, but was not greater than the nominal 0.130 gm specified. For the purposes of calculations it was assumed to be 0.125 gm.

Piekutowski<sup>6</sup> performed a series of calorimeter tests to measure the energy of detonation in order to arrive at a charge weight of PETN which would liberate an amount of energy equal to that of the 1.70 gram lead azide basic charge. Bomb calorimeter measurements performed in air at one atmosphere provided the heat of combustion, whereas similar tests using argon provided the heat of detonation. His data obtained for the heat of detonation is reproduced in Table 1. The column labeled "Net Heat Release" is the total heat release measured using the argon bomb calorimeter less that produced by the silver azide initiator (calculated to be  $2.34 \times 10^9$  ergs based upon a mean weight of 0.125 gm and the average value for the heat of detonation of silver azide given by Piekutowski to be  $1.88 \times 10^{10}$  ergs/gm). Using this correction for the composite PETN charges, the average heat of detonation for PETN as fabricated in this style charge is  $5.66 \times 10^{10}$  ergs/gm with a coefficient of variation of 7%.

For the three sizes tested by Piekutowski there appears to be some correlation in the experimental scatter due to device size. This is to be expected since there is a certain starting distance before the detonation wave is fully established in the PETN. However, the value of  $5.79 \times 10^{10}$  ergs/gm at maximum density conditions (1.77 gm/cc) quoted by Piekutowski is only 2% greater and within one third of a standard deviation of the value calculated from his calorimeter data. The mass density of the Stresau charges, reported to be approximately 1.70 gm/cc is slightly less than the maximum for PETN and is consistent with the value calculated above of  $5.66 \times 10^{10}$  ergs/gm.

Table 1. Results of bomb calorimeter measurements<sup>6</sup> for various explosive devices.

Unit Number	Charge Type	Mass of Explosive Less Initiator (gm)	Total Heat Release ( $10^{10}$ ergs)	Net Heat Release ( $10^{10}$ ergs)	Heat of Detonation ( $10^{10}$ ergs/gm)
111	PbN <sub>6</sub>	1.7057	2.25	--	1.32
302	PbN <sub>6</sub>	1.7083	2.25	--	1.32
41	PETN	0.4669	3.17	2.94	6.29
22	PETN	0.4628	3.02	2.78	6.01
113	PETN	0.3680	2.25	2.02	5.48
27	PETN	0.3667	2.35	2.12	5.77
104	PETN	0.3621	2.10	1.86	5.14
3	PETN	0.3510	2.13	1.89	5.39
11	PETN	0.3477	2.16	1.92	5.53

The scatter in the energy release data for the 1.70 gram lead azide charges has a coefficient of variation of 1% based upon the four air shots and two argon shots in the bomb calorimeter.<sup>6</sup> The value of 7% for the small PETN charges cited above is probably due to the composite design employing the silver azide initiator. This coefficient of variation would be expected to decrease as the amount of PETN in the composite design is increased, minimizing the effect of a finite initiation distance in the PETN.

These calorimeter results can be used to calculate the effective density  $\delta$ , the energy per unit mass  $Q$ , and the energy per unit volume  $Q_v$  using the following definitions:

$$\delta = \frac{3W}{4\pi a^3} \quad (66)$$

$$Q = E/W \quad (67)$$

$$Q_v = \delta Q \quad (68)$$

where  $W$  is the total charge mass including the initiator,  $a$  is the charge outside radius, and  $E$  is the total heat released during detonation including that due to the initiator. A summary of these material properties for the four charge configurations used in these experiments is given in Table 2.

For surface burst experiments, the explosives were placed at zero depth of burial by carefully excavating a void equal to one-half the charge volume using a micro-vacuum consisting of a piece of 1/8 inch diameter Teflon tubing taped into the nozzle of a standard shop vacuum. The electrical leads were taped to the outside walls of the aluminum soil containers and strung in such a way that no interference resulted when the basket swung up during acceleration. The charges were fired using a standard laboratory d.c. power supply which provides up to 40 A at 40 V through the electrical slip rings.

The charge placement was quite stable and no displacement was ever observed prior to firing when on several occasions the centrifuge was shut down from full speed as a precautionary measure to confirm preshot test conditions. One run resulted in several misfires due to breakdown in the enamel insulation

Table 2. Material properties for the four different explosive charge configurations.

Charge Type	Stressau Designation	Charge Radius a (cm)	Charge Mass W (gm)	Mass Density $\delta$ (gm/cc)	Energy Release E (ergs)	Specific Energy Q (ergs/gm)	Energy Per Unit Volume $Q_V$ (ergs/cc)
1.7 PbN <sub>6</sub>	CILAS-13	0.508	1.70	3.10	2.24E10	1.34E10	4.15E10
0.49 PETN	CICCS-5	0.390	0.49	1.93	2.24E10	4.54E10	8.76E10
1.34 PETN	CICCS-1.265	0.565	1.34	1.78	7.18E10	5.34E10	9.51E10
4.08 PETN	CICCS-4	0.826	4.08	1.73	2.27E11	5.56E10	9.62E10

where it ran over a sharp edge that had formed on the soil container due to sample preparation, causing the charge to be shunted by the aluminum structure. However, the stability of the test configuration allowed two subsequent replacements of the charge on the "X" end of the rotor and one replacement on the "0" end before the problem was uncovered. In all cases the soil showed no evidence of being disturbed, except for minor marks on the surface where the lead wires touched it.

### 3-3 SAMPLE PREPARATION

Techniques to fabricate the Ottawa sand soil samples were based upon the prior experience of Piekutowski,<sup>5,6</sup> who visited the Boeing facility and participated in the test bed preparation for shots 10-X and 10-0 as well as two prior checkout shots using detonator caps.

The procedure was to calibrate the volume of the soil container using water at a known temperature. This, together with the empty weight of each container, provided a basis for determining the average density of the finished soil sample prior to placement of the explosive. The sand was pluviated by pouring it slowly onto a sieve and allowing it to free fall approximately one meter. The chosen sieve size would just allow passage of the larger particles and could be used to direct the placement of the sand. In addition, the sieve was continuously shaken from side-to-side to further disperse the sand allowing it to fall as particles instead of as a fluid stream. In this way each particle comes to an equilibrium resting place with a minimum of interference due to other falling particles. This technique produced the maximum obtainable sand density which was reproducible for a given sand type to within 0.25%.

Three different sands from the Ottawa Silica Company of Ottawa, Illinois, were used. Flintshot was desired so that the data could be compared directly to that of Piekutowski. Due to the commercial unavailability of Flintshot, the first two shots were fired in Sawing sand. Later a supply of Flintshot was obtained from the University of New Mexico Civil Engineering Research Facility (CERF) through the efforts of R. W. Henny of AFWL. However, as shown in Table 3, the size distribution of Sawing sand is quite comparable to that of Flintshot, albeit a bit finer. The third sand used, also referred to in

Table 3. Grain size distribution for three Ottawa sands.

U.S. Sieve Size	30	40	50	70	100	140	200
Opening Size, $\mu$	600	425	300	212	150	106	75
Percent Retained on U.S. Standard Sieve							
Flintshot	28	67					
Sawing Sand	5	74	20	1			
Banding Sand		1	3	33	37	20	6

Table 3, was Banding sand which is considerably finer than the other two and provided a suitable particle size variation.

The actual measured densities obtained for the various Ottawa sands were about 1% less than maximum values reported by Piekutowski<sup>5,6</sup> in his experiments at UDR. This probably reflects a systematic difference in technique between the two facilities. For the smaller centrifuge samples total weight could be obtained directly in one weighing. For the much larger UDR samples, multiple weighings were required and any spill-over was collected, weighed, and subtracted from the total. Also a mechanized sand conveyor with a rotating squirrel cage was used to disperse the sand which provided very uniform results. Other than small errors in the actual volume determination of the soil container, the most significant source of difference is attributable to the surface leveling technique. For the centrifuge studies, a piece of aluminum structural angle was used as a scree to smooth and level the surface. This would level the surface to approximately  $\pm$  0.05 cm which is the size of the larger sand grains which build up on the metal top edge. Generally, two or three passes with the scree were made to obtain the desired surface finish. This is in contrast to a single pass used with a mechanized scree at UDR.

To enhance ejecta definition, the surface was dusted with a light coat of black spray lacquer as suggested by Piekutowski.<sup>19</sup> Care was taken to avoid any cementation due to the lacquer application. This was only applied to the Ottawa sand samples to improve contrast on the otherwise all white surface.

The alluvium soil posed different fabrication problems due to the large percentage of fines. The above technique for Ottawa sand placement was not applicable at all. Instead, soil was poured into the container in 3 to 4 cm thick lifts. After placement of each lift, the sample container was dropped a dozen times onto a platform of wooden 4" x 4"s from a height of approximately 20 cm. Greater height caused the soil to bounce instead of compact.

The container was overfilled to a height of approximately 3 cm above the top edge. At this point both samples for a given run were centrifuged at 600 rpm (500 G) for 10 minutes. The samples were then removed and the surface leveled using the aluminum scree. For the nominal four percent moisture content

alluvium (shots 18-X, 18-0) this technique produced a density of 1.53 gm/cc. The 2.65% moisture content alluvium (shots 17-X, 17-0) measured 1.61 gm/cc.

Samples for shots 16-X and 16-0, which were prepared using the drop technique but not centrifuged, attained a considerably lower density (1.45-1.43 gm/cc) which proved not to be stable. After these shots were fired, the ground zero surface had subsided approximately 0.8 cm. This subsidence probably occurred in two stages, some during spin-up and the remaining amount during the firing of the explosive. It was concluded that it did not all occur during spin-up, since it was greater near the crater than around the container edge. As a result these data points for apparent crater volume were ambiguous due to this subsidence of the ground zero surface (the maximum lip height was below the original level). However, they satisfied the test objective to ensure the reproducibility of the KAFB alluvium. Based upon a reference plane tangent to the minimum surface elevation just outside the crater lip, the two volumes differed by only 6%.

Sample preparation for the UDRI 1-G control shots in alluvium differed in that the centrifuge could not be used to obtain maximum density. Instead, the material was tamped using layers of approximately 3 cm thickness. In this way density of approximately 1.60 gm/cc was obtained. This procedure would cause a tendency toward layering of the sample, but according to Piekutowski<sup>20</sup> no direct evidence was observed, although the scatter was much greater than for his previous shots in Ottawa sand.

The KAFB alluvium was shipped in sealed five gallon cans lined with plastic. The moisture content was approximately 4% for all the cans. Shots 17-X and 17-0 were fired in alluvium that was exposed to laboratory air conditions for two weeks. This material had dried out some and measured 2.65% moisture.

All the soils used in this program were characterized by separate testing performed by Shannon and Wilson, Inc., of Seattle, Washington. The results of their tests provided failure envelopes for confining pressures up to 28.73 tons/ft<sup>2</sup> (27.56 bars) and the associated triaxial loading paths. This data is given in Appendix C. These material properties tests provide reference

conditions for the soils used and this information can be utilized to design future centrifuge tests on these same materials.

### 3-4 TEST PROCEDURE

The symmetric design of the rotor allows firing two shots during the same run. This provides an experimental convenience but is not necessary for dynamic balance as originally envisioned<sup>4</sup> since negligible amounts of material are ejected from the swing baskets (less than 25 gm). Dual shots eliminate the need for a counterweight and do provide a convenient control in sample preparation as well as test conditions and, as such, were always employed. Each shot is designated by the run number followed by the suffix 'R' or 'L' to denote the appropriate rotor end.

The entire test sequence following the mounting of the finished, weighed samples is summarized by the following procedural check list used during the run.

- (1) Firing circuit continuity check.
- (2) Install shorting plugs in centrifuge and firing unit(s).
- (3) Place charges in soil samples.
- (4) Check stray voltage in firing circuit.
- (5) Connect charge leads.
- (6) Close centrifuge aerodynamic housing.
- (7) Remove shorting plugs on centrifuge.
- (8) Close safety door barrier.
- (9) Remove shorting plugs on firing unit.
- (10) Accelerate motor to desired rpm.
- (11) Fire on countdown.

At any time a run could be halted and restarted at the discretion of the test conductor. This occurred on many occasions when a stray washer or small piece of wire produced an explainable sound during spin-up. In addition to the test conductor, there is a centrifuge operator and an ordnance technician. Each operates independently and is responsible for the safety of his aspect of the procedure. Upon the expiration of a five minute period in

evacuate the explosive products following firing, the chamber is reopened. Stereo and documentary photographs are taken immediately prior to any handling of the specimens.

All the craters produced in the dry soils tested in this program appeared to be completely stable and no evidence of subsequent shape change due to vibration, windage or slumping was observed. Therefore, in all cases the craters could be measured using a special profilometer after the centrifuge had stopped. Runs 10 through 13 were measured using the depth gauge of an ordinary machinist's vernier caliper in conjunction with a horizontal reference provided by a 1/2-inch steel machinist's scale positioned above the sample using gauge blocks. These measurements were very tedious and gave rise to the design of a profilometer which was fabricated in time to be used to measure the craters from runs 14 through 17. The profilometer is a scaled-down version of one originally designed by T. J. Nowakowski.<sup>5</sup> It consists of seventy-one, 1/8 inch diameter steel rods spaced in 0.6 cm centers providing coverage of 42 cm which is 90% of the bottom diameter.

The part of the rod which contacts the soil is tapered with a 0.10 cm flat on it. The rod lengths are controlled so that displacement can be measured from either end using a center caliper or a dial gauge. Recently a dial gauge has been fitted to a metal tube which slips over the rod to whom is fabricated to further facilitate reading these rod extensions. The accuracy of a crater and the measurement along a given path is well within  $\pm 0.11$  cm in both the horizontal and the vertical directions. The earlier measurements using the steel scale for a horizontal reference were within  $\pm 0.01$  cm vertically and  $\pm 0.02$  cm horizontally. The accuracy of either technique is limited by the actual contact of contact with the soil surface and required extreme care to maintain consistency from cycle where the temperature variations are as large as 0.50°C in 10 minutes.

This approach of combining different data sources will be able to make comparisons with the existing literature, as well as to make use of well-established experimental techniques.<sup>17</sup> In addition, many results from the content analysis experiments

were so encouraging that additional 1-G control shots were made with the larger PETN charges designed for the centrifuge experiments to complete this comparison.

These additional shots were performed by A. J. Piekutowski of UDRI under separate contract to AFWL. The 1-G test matrix was coordinated by R. W. Henny of AFWL and the explosive charges were provided from the lot fabricated by Stresau Inc. for the high-G work. The details and results of these experiments were supplied by Piekutowski<sup>20</sup> and are given in Appendix B. Tables B3 and B4 give detailed data for the larger PETN charges in Ottawa Flintshot sand. Table B5 provides data on a checkout series in KAFB alluvium using the 1.70 gram lead azide charge design. Tables B6 and B7 give the results for the larger PETN charges in KAFB alluvium.

## SECTION 4 OTTAWA SAND RESULTS

A summary of the ten Ottawa sand centrifuge shots is provided by Table 4. In addition, nine 1-G control shots are shown. These include two 1.70-gm lead azide shots,<sup>5</sup> three 0.49-gm PETN shots,<sup>6</sup> and four shots performed expressly to evaluate the behavior of the larger PETN charges at 1 G.<sup>20</sup> Complete data tables as well as stereo photographs and crater profiles are given in Appendix A for the centrifuge shots. Appendix B contains data tables for the 1-G control shots. All of these shots used a half-buried spherical explosive charge configuration in a homogeneous soil. For all of these zero-depth-of-burial results, the crater can be shown to depend upon only a single non-dimensional parameter,  $\pi_2$ , referred to as a gravity-scaled yield parameter derived in Section 2.3, quoted in eq. 54, and based on an earlier dimensional analysis.<sup>4</sup> Application to these experiments is discussed below.

### 4-1 PARTICLE SIZE DEPENDENCE

Similarity requirements for explosive cratering experiments in identical materials are satisfied if all linear dimensions are reduced by a factor equal to the reciprocal of the gravity field strength (eq. 45.2). In the case of a granular soil, the question arises as to whether the particle size is small on the scale of the experiment allowing the soil to be treated as a continuum with no inherent size effect. In general, since the particle size distribution determines the constitutive behavior of a given soil, a conflict would arise if particle size were to be scaled. This is a non-trivial question and cannot be answered in general for a material without appropriate testing, since the possibility of an inherent size property (such as flaw size, or pore size, etc.) can control the phenomenon under investigation.

Two shots were conducted to explore grain size effects for noncohesive dry sands. Banding sand was used for shots 12-X and 13-X which are to be compared with shots 12-0 and 13-0, fired in Flintshot. Shots 12-0 and 12-X were fired at 451 G, whereas shots 13-0 and 13-X were fired at 306 G. As shown in Table 3, the average particle size of the Banding sand was approximately one-third that of the Flintshot sand. Earlier work by Piekutowski,<sup>19</sup> using 1.70

Table 4. Ottawa sand cratering data summary.

Shot Number	g	ρ	c	ω	ε	Q	δ	a	d	v	r	h	π	π <sub>v</sub>	π <sub>r</sub>	π <sub>h</sub>	
	Gravity (G)	Sand Type	Sand Density (gm/cc)	Charge Type	Charge Mass (gm)	Energy Release (erg)	Specific Energy (erg/gm)	Mass Density (gm/cc)	Charge Radius (cm)	Depth of Burst (cm)	Radius (cm)	Depth (cm)	$\frac{g}{Q} \left( \frac{W}{\delta} \right)^{\frac{1}{2}}$	$\frac{V_0}{W}$	$r \left( \frac{D}{W} \right)^{\frac{1}{2}}$		
10-X	463	SAWING	1.774	Pb N <sub>6</sub>	1.70	2.24E10	1.32E10	3.10	0.508	0	27.1	3.87	0.89	2.82E-5	28.3	3.93	0.903
10-C	463	SAWING	1.781	PETN	0.49	2.24E10	4.54E10	1.93	0.390	0	17.1	3.56	0.71	6.35E-6	61.8	5.46	1.090
11-X	451	FLINTSHOT	1.776	PETN	1.34	7.18E10	5.34E10	1.78	0.565	0	35.1	4.38	0.99	7.54E-6	46.7	4.82	1.090
11-O	451	FLINTSHOT	1.781	PETN	1.34	7.18E10	5.34E10	1.78	0.565	0	38.0	4.31	0.97	7.54E-6	50.5	4.74	1.070
12-X	451	BANDING	1.677	PETN	4.08	2.27E11	5.56E10	1.73	0.825	0	96.3	6.33	1.28	1.06E-5	39.6	4.71	0.952
12-O	451	FLINTSHOT	1.778	PETN	4.08	2.27E11	5.56E10	1.73	0.826	0	101.0	6.41	1.31	1.06E-5	44.0	4.86	0.993
13-X	306	BANDING	1.677	PETN	4.08	2.27E11	5.56E10	1.73	0.826	0	119.0	6.65	1.56	7.19E-6	48.9	4.94	1.160
13-O	306	FLINTSHOT	1.782	PETN	4.08	2.27E11	5.56E10	1.73	0.826	0	126.0	6.88	1.37	7.19E-6	55.0	5.22	1.040
15-X	10	FLINTSHOT	1.784	PETN	0.49	2.24E10	4.54E10	1.93	0.390	0	94.8	6.40	1.26	1.37E-7	343.0	9.83	1.930
15-O	10	FLINTSHOT	1.784	PETN	0.49	2.24E10	4.54E10	1.93	0.390	0	95.2	6.40	1.27	1.37E-7	344.0	9.83	1.950
UDRI-9*	1	FLINTSHOT	1.802	Pb N <sub>6</sub>	1.70	2.24E10	1.32E10	3.10	0.508	0	436.0	10.20	2.29	6.08E-8	462.0	10.40	2.330
UDRI-22	1	FLINTSHOT	1.802	Pb N <sub>6</sub>	1.70	2.24E10	1.32E10	3.10	0.508	0	420.0	10.10	2.35	6.08E-8	445.0	10.30	2.400
UDRI-117	1	FLINTSHOT	1.802	PETN	0.49	2.24E10	4.54E10	1.93	0.390	0	274.0	8.76	2.06	1.37E-8	1002.0	13.50	3.170
UDRI-120	1	FLINTSHOT	1.796	PETN	0.49	2.24E10	4.54E10	1.93	0.390	0	292.0	8.88	2.13	1.37E-8	1064.0	13.70	3.280
UDRI-146	1	FLINTSHOT	1.796	PETN	0.49	2.24E10	4.54E10	1.93	0.390	0	284.0	8.89	2.02	1.37E-8	1035.0	13.70	3.110
UDRI-642	1	FLINTSHOT	1.802	PETN	1.34	7.18E10	5.34E10	1.78	0.565	0	640.0	11.80	2.50	1.67E-8	861.0	13.00	2.760
UDRI-644	1	FLINTSHOT	1.802	PETN	1.34	7.18E10	5.34E10	1.78	0.565	0	706.0	12.00	2.66	1.67E-8	949.0	13.20	2.940
UDRI-643	1	FLINTSHOT	1.802	PETN	4.08	2.27E11	5.56E10	1.73	0.826	0	167.0	16.30	3.39	2.35E-8	741.0	12.40	2.580
UDRI-645	1	FLINTSHOT	1.802	PETN	4.08	2.27E11	5.56E10	1.73	0.826	0	175.0	16.40	3.54	2.35E-8	773.0	12.50	2.700

• Last Date, Measurements 5/6/20

gram lead azide charges resulted in a factor of 2 difference in the apparent crater volume obtained for the two materials. For these 1-G tests, the crater volume for the Banding sand at maximum density ( $\rho = 1.744$ ) was 192 cc, approximately 55% less than the Flintshot crater volume. The corresponding crater volumes from the centrifuge tests for both the 306-G shots and the 451-G shots were only 6% and 5% smaller, respectively, for the Banding sand as shown in Table 5. Note that the maximum density obtainable for the Banding sand in the high-G shots was somewhat less than that obtained for the 1-G shot; however the former was a stable density and there was no settling observed. This lower density could reflect a slightly different size distribution since the UDRI sand was from a different lot. In addition, the finer sand is harder to pluviate since it is less uniformly graded.

An observation from these few shots is that for increased  $\pi_2$  (large yield or large gravity) the influence of particle size variation on crater size decreases. This indicates that material strength effects become less important for large  $\pi_2$ . Secondly, it confirms that the Ottawa sand can be treated as a continuum for the laboratory scale high-G experiments. This also suggests that particle grain size can be varied to achieve some desired behavior without violating the scale of the experiment. For the case of saturated sand, perhaps grain size could be scaled independently from experiment size to obtain the correct pore water response.

#### 4-2 CONSTANT $\pi_2$ TEST

A critical test has been defined to evaluate the applicability of using a centrifuge to achieve similarity with a given half buried explosive in a given soil material. This test involves measuring crater characteristics due to charges of different size under different gravity while holding the value of  $\pi_2 = (g/Q)(W/\delta)^{1/3}$  constant. Then, if the crater characteristics for a soil material are functions only of  $\pi_2$ , the material models used in deriving the  $\pi$ -group representation are adequate (Section 2). Furthermore, this allows charge size effects to be determined by tests in which gravity alone is varied.

For  $\pi_2 = \text{constant}$ , the charge weight for a given explosive varies as  $1/g^3$ , fixing the relationship between  $W$  and  $g$  for fixed  $\pi_2$ . To test this

Table 5. Variation of crater volume due to particle size effects.

	Ottawa Flintshot Sand			Ottawa Banding Sand			Banding volume Flintshot volume
	Shot Number	Density (gm/cc)	Apparent Volume (cc)	Shot Number	Density (gm/cc)	Apparent Volume (cc)	
1-G, 1.7-gm PbN <sub>6</sub>	UDRI-9 <sup>5</sup> UDRI-22 <sup>5</sup>	1.802	428.	UDRI-265 <sup>19</sup>	1.774	192.	0.45
306-G, 4-gm PETN	13-0	1.782	126.	13-X	1.677	119.	0.94
451-G, 4-gm PETN	12-0	1.778	101.	12-X	1.677	96.3	0.95

relationship, two different charge sizes of the same type explosive charge were fired at different values of gravity as determined by the ratio of charge masses. When the test matrix was devised, it was assumed that for the same explosive, charge properties would not depend upon size and therefore the gravity ratio ( $g_1/g_2$ ) for a given charge mass ratio ( $W_1/W_2$ ) would be simply

$$\frac{g_1}{g_2} = \left( \frac{W_2}{W_1} \right)^{1/3} \quad (69)$$

To first order, this assumption is valid; but, as the data in Table 2 demonstrate, the presence of the silver azide initiator does influence the value of all the pertinent charge properties for the composite PETN charges. Taking this into consideration, the prescribed gravity ratio for constant  $\pi_2$  can be expressed as follows

$$\frac{g_1}{g_2} = \frac{Q_1}{Q_2} \left[ \left( \frac{\delta_1}{\delta_2} \right) \left( \frac{W_2}{W_1} \right) \right]^{1/3} \quad (70)$$

Before any conclusions regarding the application of centrifuge results to the prediction of full-scale 1-G events can be made for a given material, the constant  $\pi_2$  test must be shown to hold for different charge size experiments performed on the centrifuge with gravity test conditions as prescribed by eq. 70.

For the Flintshot Ottawa sand, three experiments were performed to evaluate compliance with the constant  $\pi_2$  test. Shots 11-X and 11-0 were performed at 451 G to confirm reproducibility using the nominal 1.34 gm PETN charges. Shot 13-0, a 4.08 gm PETN charge fired at 306 G, provided a comparable value of  $\pi_2$  for which the cratering efficiency  $\pi_v$ , the non-dimensional crater radius,  $\pi_r$ , and the non-dimensional crater depth,  $\pi_h$ , all compare favorably with those obtained for shots 11-X and 11-0. The slightly larger values of the dependent variables associated with shot 13-0 are consistent with the lesser value of  $\pi_2$ , 7.19E-6, as opposed to 7.54E-6, for the shots 11-0 and 11-X. These results indicate that, to well within experimental scatter, similarity was achieved.

#### 4-3 SCALING RULES

The set of dimensionless  $\pi$ -groups provides a basis for comparing various high-G and 1-G results at differing energy levels. As the previous analysis shows, experiments at a constant  $\pi_2$  give the same value of the crater dependent groups,  $\pi_v$ ,  $\pi_r$  and  $\pi_h$ . Thus a single experiment at a given  $\pi_2$  furnishes a scaling rule for all similar experiments. However, it furnishes no information on nonsimilar experiments, such as varying energy and hence size at fixed gravity. These scaling rules are discovered experimentally by varying  $\pi_2$  in a series of experiments.

Figures 3, 4, and 5 show each of the dependent groups  $\pi_v$ ,  $\pi_r$  and  $\pi_h$ , respectively, versus  $\pi_2$  for all shots included in Table 4. As can be seen, all the results can be adequately represented by a power law fit, such as the following for cratering efficiency  $\pi_v$ :

$$\pi_v \pi_2^\alpha = k_v = \text{const} \quad (71)$$

and for crater radius,

$$\pi_r \pi_2^\beta = k_r = \text{const} \quad (72)$$

and for crater depth,

$$\pi_h \pi_2^\gamma = k_h = \text{const} \quad (73)$$

These then are the form of the function  $\mathcal{F}$  as given in (65).

Expanding eq. 71 using the definition of the  $\pi$ -groups gives the explicit form for crater volume:

$$V = k_v \left( \frac{W}{E} \right) \left[ \frac{g}{Q} \left( \frac{W}{E} \right)^{1/3} \right]^{-\alpha} \quad (74.1)$$

where, from the experimental results, a least squares, straight line fit gives the following values for the constants, where the uncertainty shown for the exponent  $\alpha$  is the standard error of estimate (68% confidence):

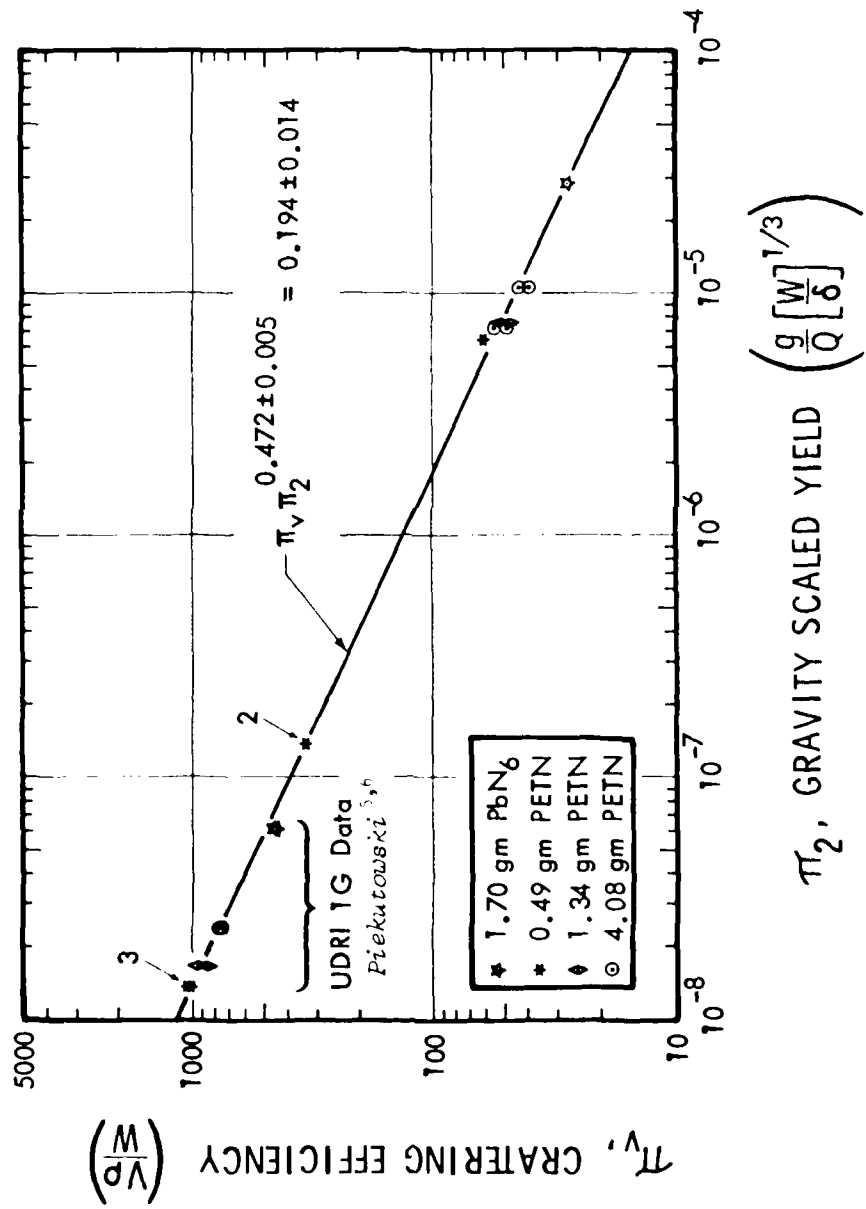


Figure 3. Surface burst scaling rule for apparent crater volume in Ottawa sand.

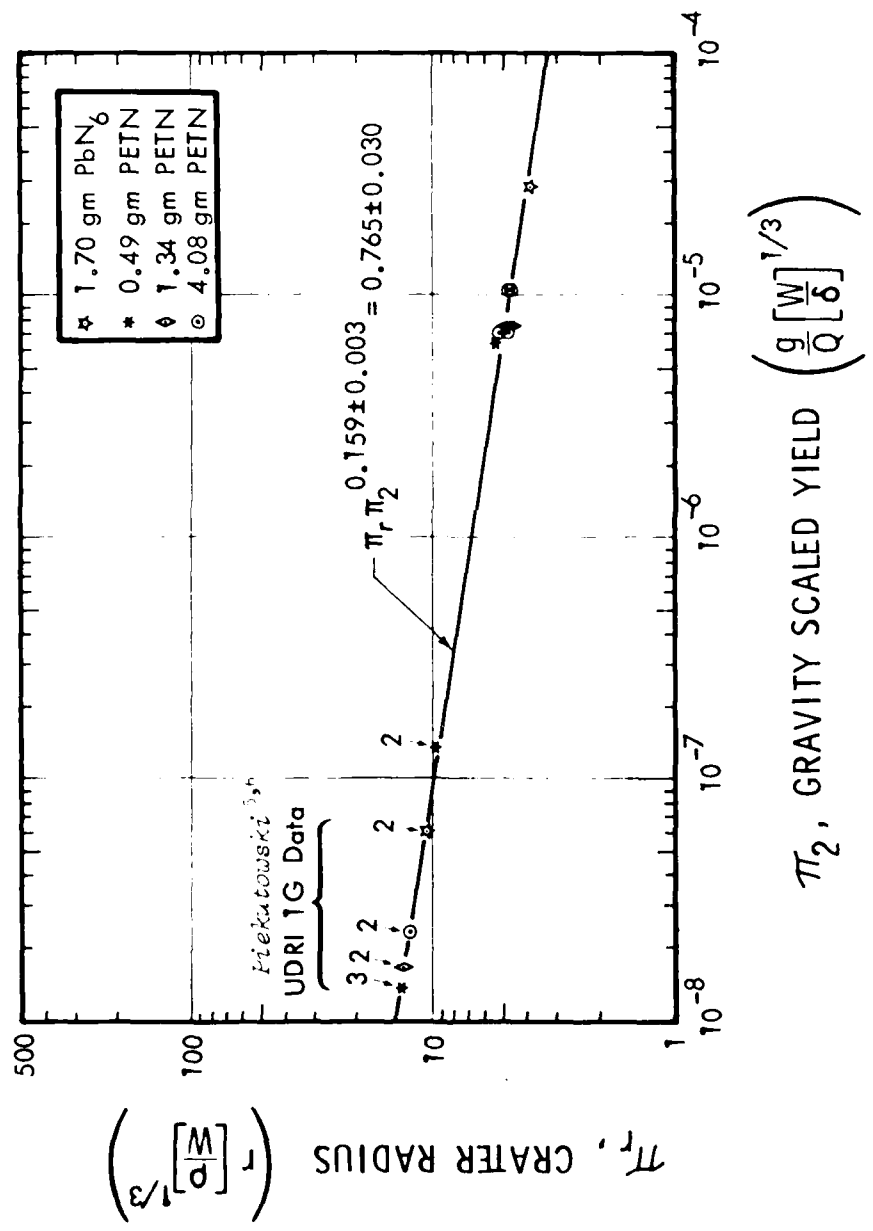


Figure 4. Surface burst scaling rule for apparent crater radius in Ottawa sand.

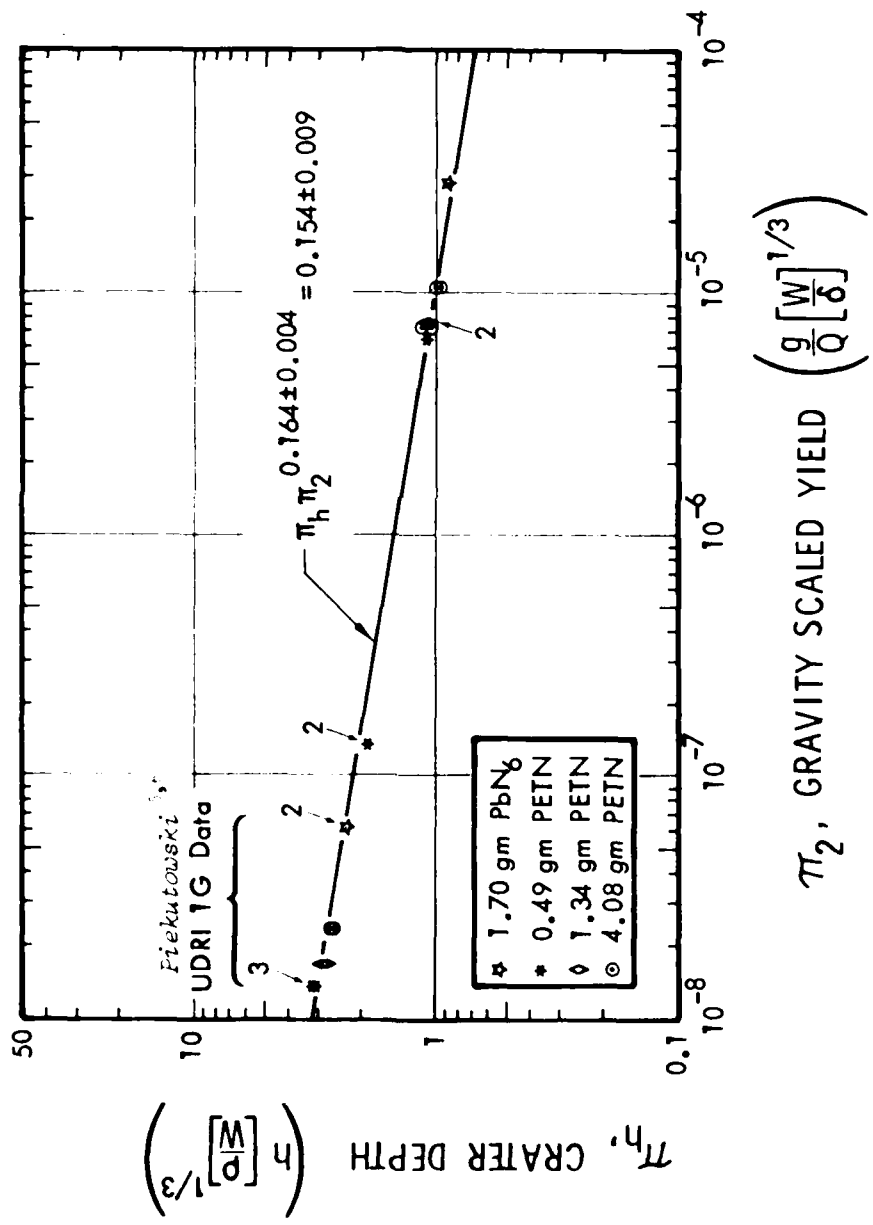


Figure 5. Surface burst scaling rule for apparent crater depth in Ottawa sand.

$$V = (0.194 \pm 0.014) \left( \frac{W}{\rho} \right) \left[ \frac{g}{Q} \left( \frac{W}{\delta} \right)^{1/3} \right]^{-0.472 \pm 0.005} \quad (74.2)$$

Likewise, from the best fit for the crater radius,

$$r = (0.765 \pm 0.030) \left( \frac{W}{\rho} \right)^{1/3} \left[ \frac{g}{Q} \left( \frac{W}{\delta} \right)^{1/3} \right]^{-0.159 \pm 0.003} \quad (75)$$

and the best fit for the crater depth,

$$h = (0.154 \pm 0.009) \left( \frac{W}{\rho} \right)^{1/3} \left[ \frac{g}{Q} \left( \frac{W}{\delta} \right)^{1/3} \right]^{-0.164 \pm 0.004} \quad (76)$$

The dependence of the crater dimensions in Ottawa sand on all of the independent variables is given by these expressions.

The so-called yield exponents, the power dependence on the charge mass with all other variables fixed, are determined for Ottawa sand from these results and shown with uncertainties corresponding to one standard error:

$$V \propto W^{(1-\alpha/3)} = W^{0.842 \pm 0.002} \quad (77)$$

$$r \propto W^{(1-\beta)/3} = W^{0.280 \pm 0.001} \quad (78)$$

$$h \propto W^{(1-\gamma)/3} = W^{0.279 \pm 0.002} \quad (79)$$

If  $\alpha$ ,  $\beta$ , and  $\gamma$  had all come out to be zero, then the familiar cube root scaling would be applicable. In general, this is not the case. These exponents can be considered to be material properties.

Alternatively, consider fixed charge size and type at varying gravity. Then eqs. 74, 75 and 76 reduce to

$$V \propto g^{-\alpha} = g^{-0.472 \pm 0.005} \quad (80)$$

$$r \propto g^{-\beta} = g^{-0.159 \pm 0.002} \quad (81)$$

$$h \propto g^{-\gamma} = g^{-0.164 \pm 0.004} \quad (82)$$

giving the gravity dependence at fixed charge size. This clearly supports the contention of the previous analyses that the dependence of crater formation upon charge size can be determined by experiments using fixed charge size but varying g. The shot 10-X at 463 G using 1.70 gm of lead azide directly simulates a 169-ton mass of lead azide at 1 G or a mass of 2.86 kilotons of TNT at 1 G.

It should be noted that the variable  $\pi_4$  is different for some of the tests plotted in Figures 3, 4, and 5. However, the experimental results indicate that  $\pi_V$ ,  $\pi_r$  and  $\pi_h$  do not depend upon this parameter. All points fall on the same straight line when plotted versus  $\pi_2$ , with no systematic variation for various  $\pi_4$ . The dependence of the various physical parameters actually varied in this series of experiments is accounted for solely by those occurring in  $\pi_2$ .

In summary, eqs. 74, 75 and 76 are referred to as scaling rules for dynamically nonsimilar experiments. They are functional relationships for arbitrary values of  $\pi_2$  and hence for arbitrary size experiments. Such relationships are expected to have different functional forms for different soil materials. These scaling rules should not be confused with scaling relationships based upon dynamically similar experiments where size is varied while holding the value of  $\pi_2$ , as well as other pertinent  $\pi$ -groups, constant. In the latter case, all the geometrical features are identical, differing only as the size scale factor  $\alpha_x$ . In the former, geometric shape variations are expected and generally are the case as  $\pi_2$  is varied.

The important observation for all three crater-size parameters shown in Figs. 3, 4, and 5 is that the slope of the line determined by varying charge size at constant 1-G conditions is in excellent agreement with the slope of the line determined by varying gravity for identical charges. This provides a very convincing argument that large yield can be simulated with small charges at elevated gravity. Furthermore, it confirms the use of  $\pi_2$  as the sole parameter to correlate the effects of gravity and charge size and type on the several forms  $\pi_Y$ ,  $\pi_r$  and  $\pi_h$  of the dependent parameters. The parameter  $\pi_3$  for depth of burial was held constant and equal to zero. No data were obtained on the variation with respect to this parameter.

The non-dimensional form of the gravity-scaled yield parameter  $\pi_2$  very adequately accounts for the large differences in the properties of the various explosives. For the composite PETN charges, the mass-averaged values given by eqs. 66 and 67 were used for specific energy  $Q$  and for charge density  $\delta$ . As can be seen in Table 2, the lead-azide properties and the PETN properties differ by a factor of 4 on specific energy and a factor of 2 on charge density. The various values for the four different explosive charge types used cover the entire range encountered for common chemical high explosives. The density parameter  $\pi_4$  was varied by a factor of 2, but no dependence on this variation was detected.

This result, based upon the utility of the  $\pi_2$  parameter, provides a basis for the definition of an equivalent charge, thereby relaxing the similarity requirement given by eq. 45.5—that the same explosive type is necessary for similar experiments in the same soil. This has a particular significance for large-scale simulation using the centrifuge. In general, the large charges used in the field consist of secondary, explosives which are initiated using negligible amounts of primary explosives. In scaling down to laboratory size, the amount of primary necessary for initiation becomes significant in relation to the amount of secondary changing the overall explosive properties, as is illustrated in Table 2. On the basis of the above results, a small-scale equivalent charge of a different type can be designed to simulate the large prototype explosive.

## SECTION 5 JOHNIE BOY SIMULATION

Six high-G shots were performed in this series. The first pair (16-X, 16-0) confirmed the reproducibility of centrifuge results in KAFB alluvium. However, in spite of only 6% variation in crater volume, considerable subsidence of the ground zero surface indicated that the sample fabrication technique was inadequate. The second pair of shots (17-X, 17-0) using an improved sample preparation method as discussed in Section 3-3 indicated that the KAFB alluvium satisfied the constant  $\pi_2$  test of Section 4-2 confirming the applicability of centrifuge scaling methods. The final two shots (18-X, 18-0) were used to provide a simulation of the JOHNIE BOY 500-ton event.

Seven 1-G control shots were made by Piekutowski<sup>20</sup> to provide additional data expanding the range of the gravity-scaled yield parameter,  $\pi_2$ . The results of both the 1-G data and the high-G centrifuge data are summarized in Table 6. Detailed records of the six high-G shots are contained in Appendix A: Tables A7 through A9 and Figs. A7 through A9. The 1-G shot records are in Appendix B: Tables B5 through B7 and Figs. B5 through B7.

### 5-1 KAFB ALLUVIUM SCALING RULES

Results shown in Figs. 6, 7, and 8 based upon the limited data generated for the surface burst KAFB alluvium behavior must be considered preliminary. Of the six high-G shots only two are shown (17-X and 17-0). The crater shapes determined for 16-X and 16-0 were based upon an assumed ground zero plane which subsided 0.8 cm during firing. Shots 18-X and 18-0 were performed at finite depth of burial. The seven 1-G shots showed considerable scatter indicating possible non-uniform sample preparation as discussed in Section 3-3. Further tests should be conducted on samples prepared in the centrifuge and fired at low  $\pi_2$  to see if scatter can be reduced.

A least squares straight-line fit to the data indicates that the slope is considerably less than that determined for Ottawa sand in the previous section. In addition to this lesser slope, the craters are smaller than their

Table 6. KAFB alluvium cratering data summary.

Shot Number	Gravity G	D	W	E	Q	δ	a	d	V	r	h	π <sub>z</sub>	π <sub>v</sub>	π <sub>z</sub>	π <sub>v</sub>
		Soil Type	Soil Density (gm/cm <sup>3</sup> )	Charge Type	Charge Mass (gm)	Energy Release (erg)	Specific Energy (erg/gm)	Mass Density (gm/cc)	Charge Radius (cm)	Depth of Burst (cm)	Volume (cc)	Radius (cm)	Depth (cm)	g (W/Q) <sup>1/3</sup>	h (W/W) <sup>1/3</sup>
16-X	4.51		1.449	PETN	1.34	7.18E10	5.34E10	1.78	0.565	0	48.1	4.70	1.91	7.54E-6	52.0
16-O	4.51		1.420	PETN	1.34	7.18E10	5.34E10	1.78	0.565	0	51.0	4.78	2.08	7.54E-6	54.4
17-X	4.51		1.607	PETN	1.34	7.18E10	5.34E10	1.78	0.565	0	30.2	4.22	1.35	7.54E-6	36.2
17-O	3.06		1.609	PETN	4.08	2.27E11	5.36E10	1.73	0.826	0	98.5	6.23	1.97	7.19E-6	38.1
18-X	34.5		1.576	PETN	1.34	7.18E10	5.34E10	1.78	0.565	0.845	176.0	6.08	2.76	5.77E-6	136.0
18-O	34.5		1.570	PETN	1.34	7.18E10	5.34E10	1.78	0.565	0.362	77.7	5.37	2.26	5.77E-6	91.0
UDRI-646	1		1.622	Pb No	1.70	2.24E10	1.32E10	3.10	0.508	0	58.7	6.47	1.85	6.08E-8	56.0
UDRI-647	1		1.581	Pb No	1.70	2.24E10	1.32E10	3.10	0.508	0	72.4	6.90	1.95	6.08E-8	67.3
UDRI-648	1		1.600	Pb No	1.70	2.24E10	1.32E10	3.10	0.508	0	45.0	5.84	1.75	6.08E-8	42.4
UDRI-649	1		1.571	PETN	1.34	7.18E10	5.34E10	1.78	0.565	0	103.0	6.88	2.40	1.57E-8	121.0
UDRI-652	1		1.587	PETN	1.34	7.18E10	5.34E10	1.78	0.565	0	66.6	6.44	2.00	1.57E-8	78.9
UDRI-650	1		1.555	PETN	4.08	2.27E11	5.56E10	1.73	0.826	0	196.0	8.28	2.86	2.35E-8	74.7
UDRI-651	1		1.584	PETN	4.08	2.27E11	5.56E10	1.73	0.826	0	175.0	8.52	2.80	2.35E-8	67.9

UDRI Data, Photoevents

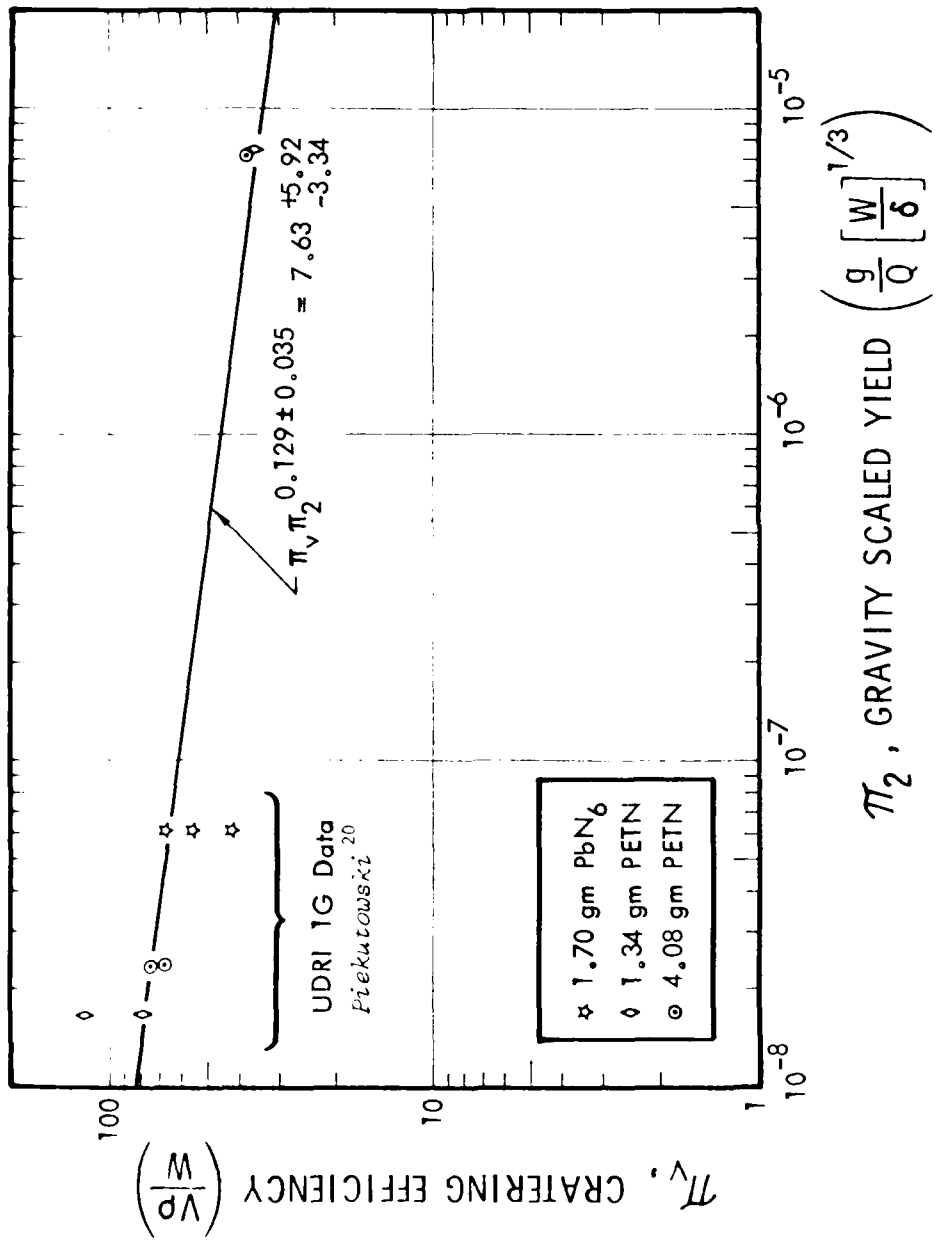


Figure 6. Surface burst scaling rule for apparent crater volume in KAFB alluvium.

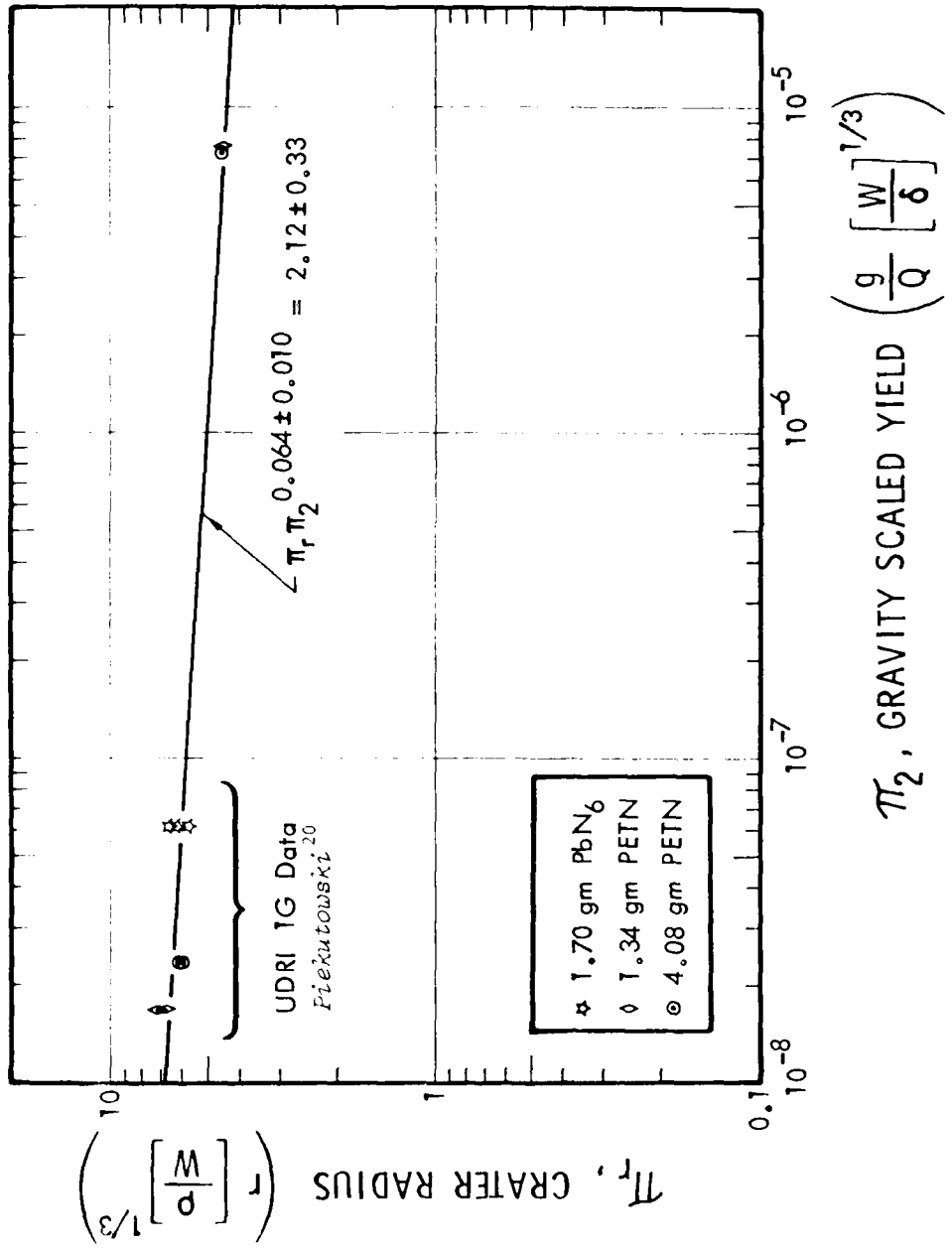
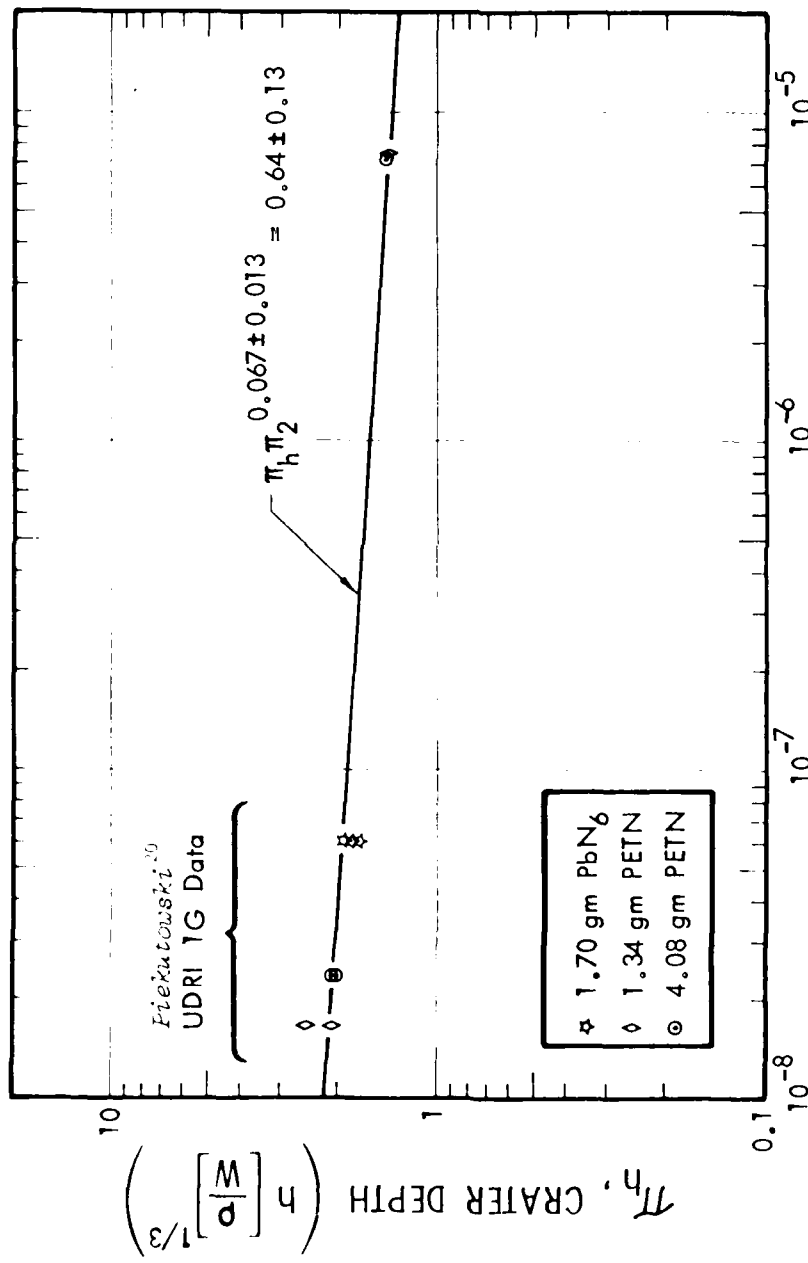


Figure 7. Surface burst scaling rule for apparent crater radius in KAFB alluvium.



$$\pi_2, GRAVITY SCALED YIELD \left( \frac{g}{Q} \left[ \frac{W}{\delta} \right]^{1/3} \right)$$

Figure 2. Surface burst scaling rule for apparent crater depth in KAFB alluvium.

Ottawa sand counterparts. For  $\pi_2 = 3.0E-8$  (approximately 1-G conditions) there is exactly an order of magnitude difference in cratering efficiency between the two soils as shown by comparing Figs. 3 and 6; whereas for  $\pi_2 = 2.0E-5$ , the cratering efficiencies are equal. Extrapolating to values of  $\pi_2$  greater than this gives larger cratering efficiency in the KAFB alluvium than in the Ottawa sand. However, these observations need to be confirmed by additional centrifuge shots to fill in the range of  $\pi_2$  between  $1.0E-7$  and  $1.0E-5$  as well as for values greater than  $1.0E-5$ .

## 5-2 NUCLEAR-PETN EQUIVALENCE

It was shown in Section 2-2 that centrifuge experiments rigorously satisfy similarity requirements only when performed using identical soil material and the same explosive type. As a practical matter the above test results show that the requirement for the use of an identical explosive can be relaxed to the use of an equivalent explosive charge. This was demonstrated in Section 4-3 where the effects due to different charge properties were accounted for by the  $\pi_2$  parameter.

To perform a centrifuge simulation of the JOHNIE BOY nuclear event, an equivalent high explosive charge was determined. This task was performed by R. T. Allen of PacTech under separate contract to the Defense Nuclear Agency. Allen<sup>10</sup> devised a hypothetical full scale equivalent PETN charge size based upon the so-called MINE THROW technique.<sup>7,8</sup> He claimed a suitable equivalence based upon two criteria. The first was to match the kinetic energy transferred into the ground beyond a range of 360 centimeters. The second was to reproduce the shape of the flow field using a suitable depth of burial for the equivalent PETN charge.

The energy coupling is essentially complete after the first few milliseconds and hence can be conveniently calculated using a finite difference wave propagation code. The standard for the actual JOHNIE BOY event was the nuclear calculation performed by Maxwell et al.<sup>9</sup> Allen's results indicated that the hypothetical full scale charge would be a PETN sphere of radius 188 cm buried at a depth of 120 cm. This corresponds to a PETN mass of 49.3 metric tons ( $49.3E6$  gm) with a total energy release of  $2.80E18$  erg. This gives a

nuclear equivalence factor of 13.4% based upon the JOHNIE BOY nominal energy release of 500 metric tons of TNT nuclear equivalent (2.095E19 erg).

The calculated energy partitioning for the JOHNIE BOY event is shown in Fig. 9 along with Allen's results for the coupled kinetic energy due to the 49.3 ton PETN sphere. The best equivalent depth of burial (120 cm) based on these calculations produced a flow field characterized by the motion of the reference hemispherical surface initially located at a radius of 360 cm. Its motion at 3.6 msec is shown in Fig. 10 along with an identical reference surface from the JOHNIE BOY calculation for comparison.

Allen chose a test condition of 345 G based upon eq. 69 using an explosive charge size of 1.2 gm PETN. That is

$$g = \left[ \frac{49.3E6}{1.2} \right]^{1/3} = 345. \quad (83)$$

Therefore the charge was to be buried at

$$\frac{1}{345} (120 \text{ cm}) = 0.348 \text{ cm.} \quad (84)$$

A second shot was fired on the same centrifuge run as a backup. For this it was decided to increase the actual depth of burial to approximately 1.5 times the charge radius or 0.845 cm. This was to provide a determination of the sensitivity of flow-field equivalence to depth of burial and to bracket the desired result. The results of these charge equivalence calculations were presented at a program review meeting<sup>11</sup> prior to the selection of the actual alluvium soil material which was eventually used for the simulation experiments.

### 5-3 EVALUATION OF RESULTS

The results of the centrifuge simulation are scaled to full size using the similarity relationship given by eq. 45.2 as  $g_1 L_1 = g_2 L_2$ . These are compared directly to the actual JOHNIE BOY crater profile<sup>8</sup> as shown in Fig. 11. With the exception of the aspect ratio, the two shots 18-0 and 18-X bracket the JOHNIE BOY crater volume, radius, and depth as anticipated. The aspect ratio was slightly larger in both cases. As shown in Fig. 12, the results of the

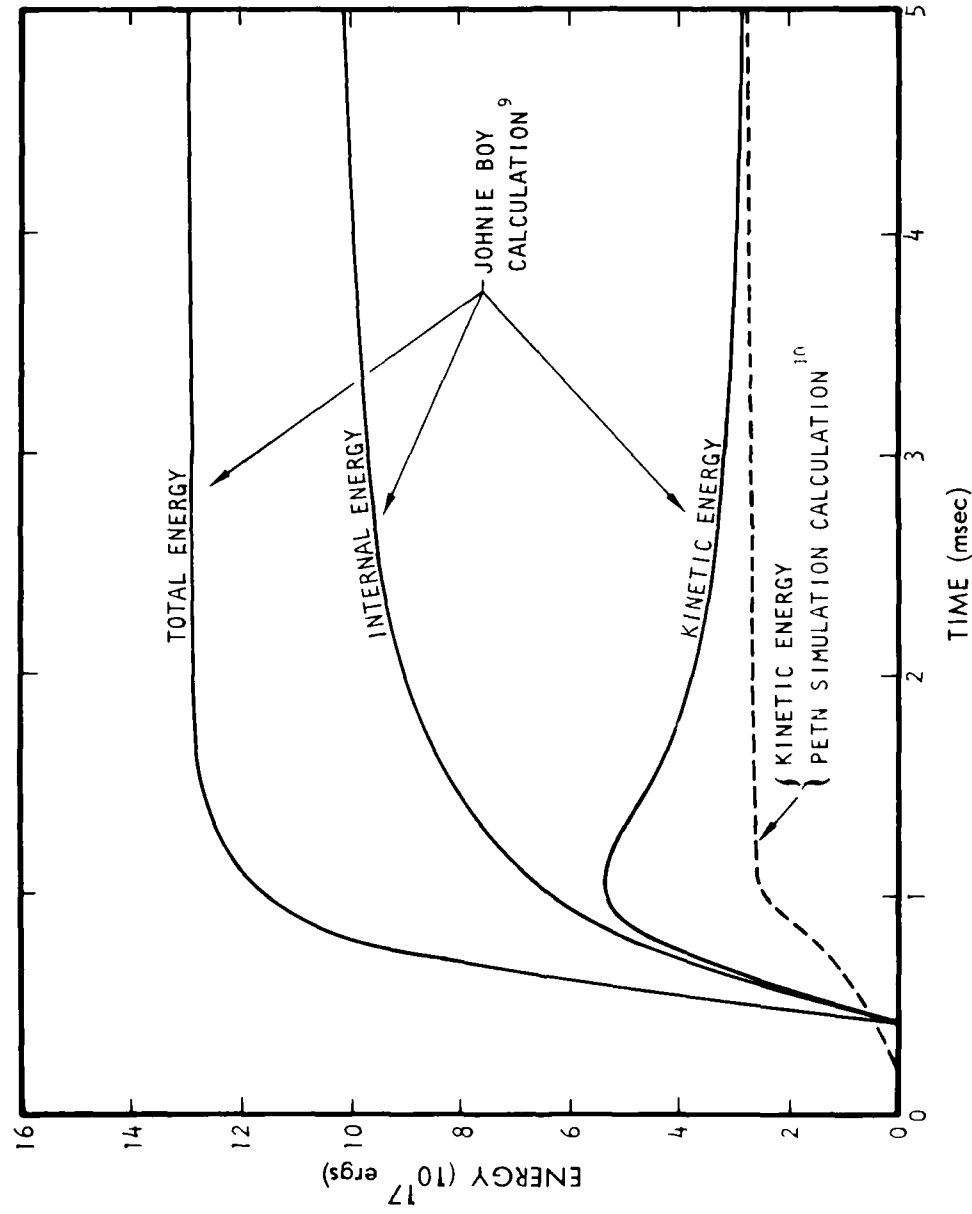


Figure 9. Comparison of kinetic energy coupling between JOHNIE BOY nuclear calculation and the PETN simulation calculation.

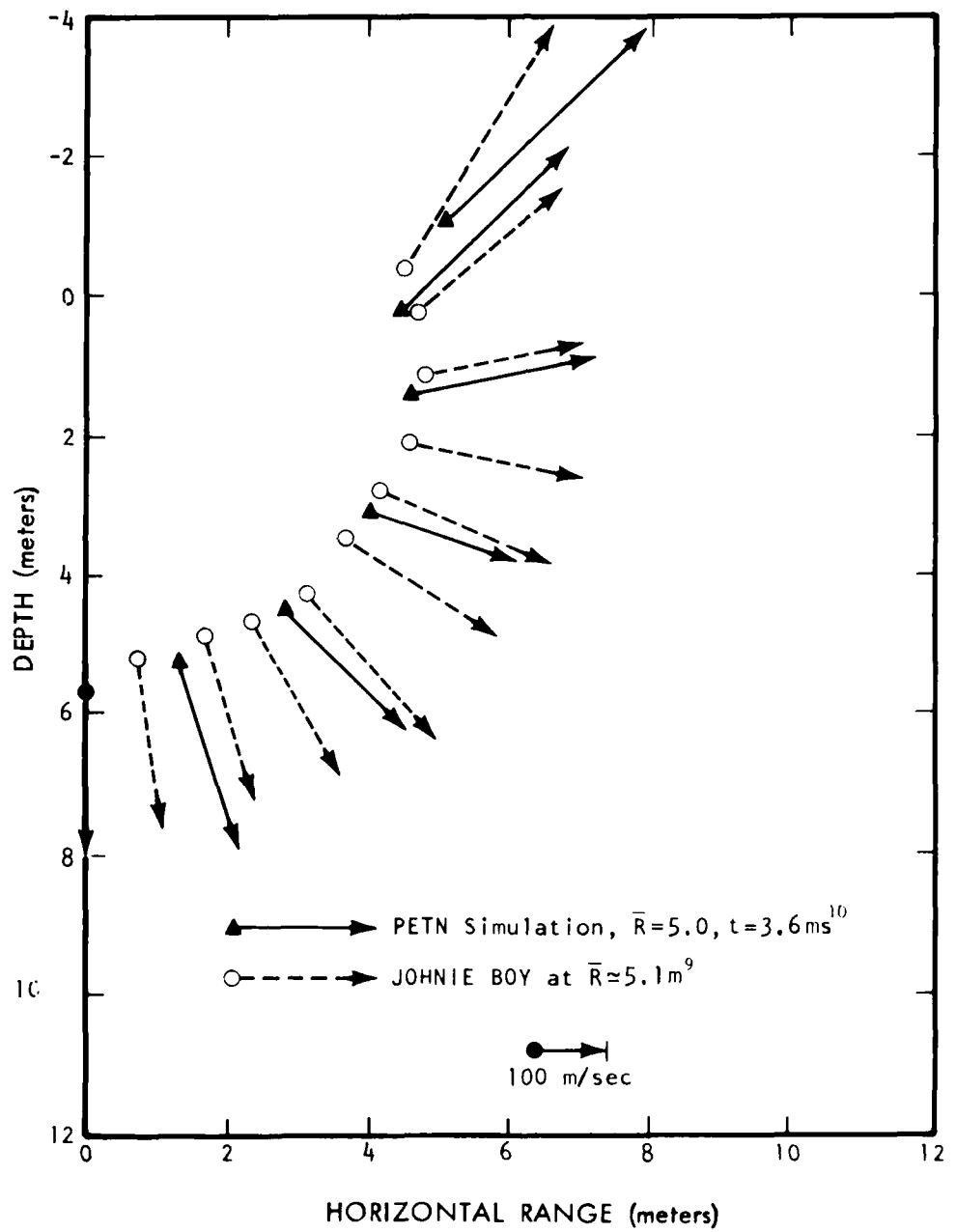
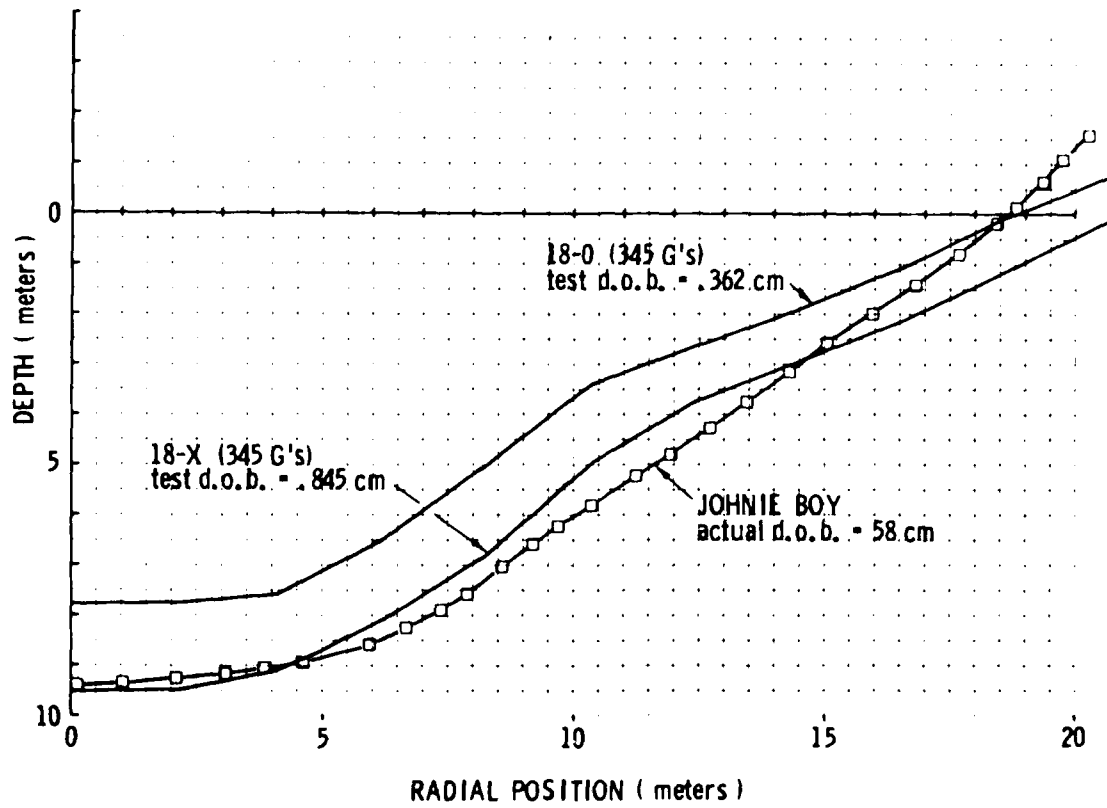
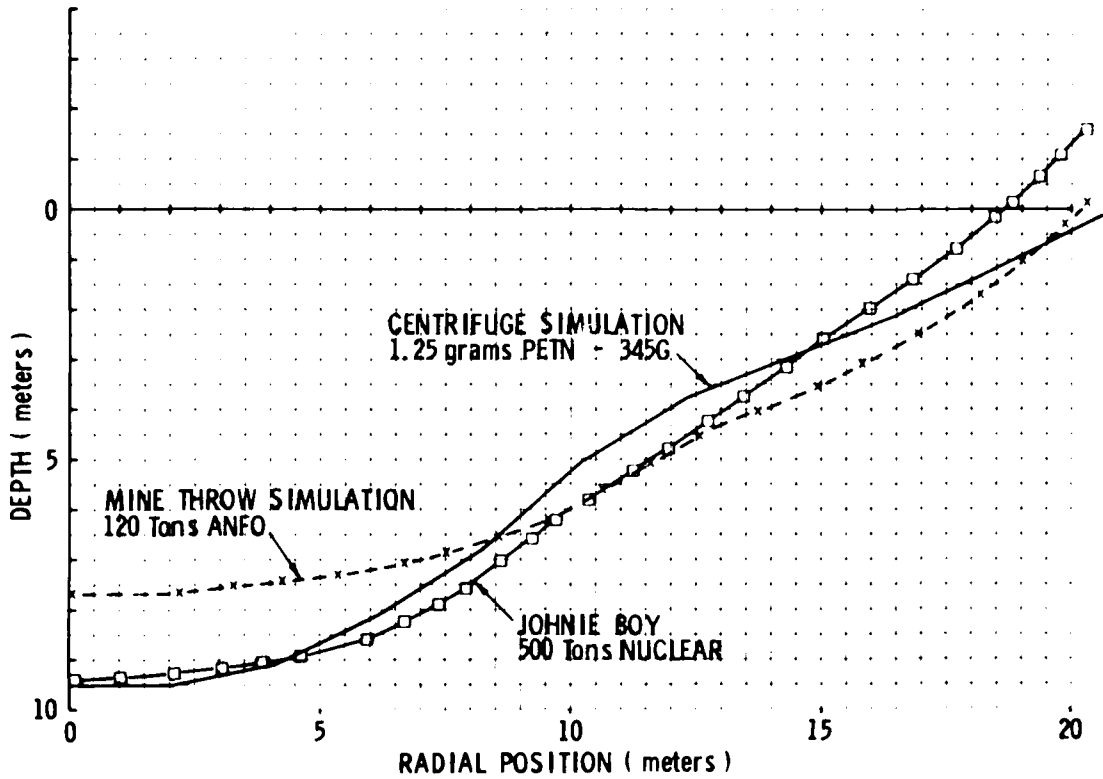


Figure 10. Flow field comparison of JOHNIE BOY versus PETN simulation.



JOHNIE BOY Actual event <sup>8</sup>		18-0 (345 G's) Test d.o.b. = .362 cm		18-X (345 G's) Test d.o.b. = .845 cm	
VOLUME (meters <sup>3</sup> )	4110	3190	- 22 %	4760	+ 16 %
RADIUS (meters)	18.6	18.5	- 1 %	21.0	+ 13 %
DEPTH (meters)	9.3	7.8	- 16 %	9.5	+ 2 %
ASPECT RATIO	2.0	2.37	+ 19 %	2.21	+ 11 %

Figure 11. Results of the centrifuge simulation showing sensitivity to equivalent burial depth.



JOHNNIE BOY <sup>8</sup> 500 tons nuclear		CENTRIFUGE SIMULATION 1.25 grams		MINE THROW <sup>8</sup> SIMULATION 120 tons ANFO	
VOLUME ( meters <sup>3</sup> )	4110	4760	+ 16 %	4893	+ 19 %
RADIUS ( meters )	18.6	21.0	+ 13 %	20.2	+ 8 %
DEPTH ( meters )	9.3	9.5	+ 2 %	7.6	- 19 %
ASPECT RATIO	2.0	2.21	+ 11 %	2.66	+ 33 %

Figure 12. Comparison of JOHNIE BOY crater simulation experiments, centrifuge result and full scale MINE THROW event.

centrifuge simulation appear to be equally as good as those from the MINE THROW event,<sup>8</sup> a full-scale, high-explosive field event which used 120 tons of ANFO to simulate the JOHNIE BOY crater. It is important to note that the ANFO charge was not spherical, but contoured to match the JOHNIE BOY pressure history at a specific isobaric contour.

The centrifuge simulation of a shallow buried nuclear event was complicated by the necessity to first devise a chemical explosive equivalence. Therefore, this was done as objectively as possible by an independent calculation. The results of this calculation represented the design of a full-scale simulation of JOHNIE BOY using the 49.3-ton sphere of PETN. It was this hypothetical event that was simulated at small scale in the centrifuge. Uncertainties in the nuclear equivalence could be responsible for any discrepancies in shape.

Another aspect of the simulation that needs to be considered as a possible source of volume discrepancy is the requirement for reconstituting a soil sample in the centrifuge that reproduces the average in situ properties for the JOHNIE BOY site. JOHNIE BOY site soil density was reported to be 1.85 gm/cc based upon measurements using the sand displacement method in a test pit.<sup>21</sup> The moisture content at the 2.5 foot depth was 3%.<sup>21</sup> Attempts to reproduce this reported value for density with the KAFB alluvium test samples were not successful; the largest attained was on the order of 1.60 gm/cc, a value more typical of desert alluvium. The moisture content of the centrifuge soil sample was 4.1%.

The  $\pm 20\%$  difference in crater volume for the two shots is well within the combined uncertainties in the definition of the JOHNIE BOY shot,<sup>22</sup> the HE-equivalence determination, and the experimental accuracy.

A significant shape difference between the actual JOHNIE BOY crater and the centrifuge craters is due to the change in slope halfway up the crater wall for the latter. This not only leads to a slightly larger radius, but it is also noteworthy that the lip height is less for the centrifuge craters.

Three factors could contribute to these shape differences. A spherical chemical charge might not adequately model the late time low pressure expansion of the JOHNIE BOY event. Another possibility is that the model soil did not possess the same cohesion near the surface as the prototype soil. A third possibility is that there may have been more compaction of the model soil near the crater attributable to lower initial density than that reported for the prototype.

It is interesting to note that the surface burst shots (centrifuge runs 16 and 17) also exhibited the discontinuity in slope which can be seen quite prominently in the photographs given in Fig. A7 through A9. The UDRI 1-G control shots in KAFB alluvium (also surface burst) exhibited a shelf at approximately the same depth, as can be seen in Fig. B5 through B7, and the lip heights were even less than those from the centrifuge experiments.

Considering these potential sources of observed discrepancies, the agreement of the two centrifuge shots with the actual JOHNIE BOY crater as shown by Fig. 11 is very satisfactory. These results strongly support the theoretical premise derived in Section 2 that small-yield shallow-buried nuclear cratering events can be simulated at small scale in the laboratory using conventional explosives in a centrifuge.

## SECTION 6 CONCLUSIONS

- (1) A similarity analysis was performed for explosive cratering phenomena using the balance equations and the jump equations of continuum mechanics in their general form. Specific constraints on centrifuge modeling brought about by various types of constitutive equations representing material behavior were identified separately. These results show that non-trivial dynamic similarity can be achieved using a centrifuge with arbitrary scaling of size, density and time. Furthermore, complete and exact dynamic similarity can be obtained between two different experiments of arbitrary size scale in the same material as long as the constitutive behavior is rate independent and has no inherent size properties.
- (2) A scaling rule for surface bursts in dry Ottawa sand was developed based upon high-G experiments, which was in excellent agreement with the large body of 1-G work performed by Piekutowski<sup>6</sup>. The crater volume depends upon the charge mass or energy (holding all other variables fixed) to the  $0.842 \pm 0.002$  power, the crater radius to the  $0.280 \pm 0.001$  power, and the crater depth to the  $0.279 \pm 0.002$  power for charge mass well into the kiloton range.
- (3) The observation for all three crater-size parameters shown in Figs. 3, 4, and 5 is that the slope of the line determined by varying charge size at constant 1-G conditions is in excellent agreement with the slope of the line determined by varying gravity for identical charges. This result provides convincing evidence that large yield craters can be simulated with small charges at elevated gravity.
- (4) A non-dimensional gravity-scaled yield parameter,  $\pi_2 = g/0 (W/L)^{1/3}$ , based upon explosive properties and gravity, gave quantitative agreement with four different composite chemical explosives over a range of gravity between 1 G and 451 G. The various material properties for the different charge types used covers the entire range encountered for common chemical high explosives. This provides a basis for the definition of an equivalent charge. It further suggests the possibility that a

nuclear-high-explosive equivalence can be determined directly using centrifuge experiments in conjunction with available data for nuclear craters.

- (5) Preliminary results for experiments performed using KAFB alluvium indicate that the yield dependence is considerably different than that for dry Ottawa sand. This scaling behavior needs to be characterized by additional centrifuge experiments.
- (6) A subscale simulation of the full-scale 500-ton JOHNIE BOY crater was satisfactorily achieved using the centrifuge test method. A nuclear-PETN charge equivalence was calculated<sup>10</sup> to provide a hypothetical full-scale equivalent PETN spherical center-initiated charge configuration which was then simulated at subscale on the centrifuge. Two centrifuge shots bracketed the desired result. The experimental agreement between model and prototype for the size of the apparent crater were within +17% and -22% on volume, +13% and -1% on radius, +2% and -16% on depth, and +19% and +11% on aspect ratio.
- (7) The centrifuge proved to be an effective tool for modeling explosive cratering phenomena in dry granular soils. No measurable Coriolis effects were observed. Experimental reproducibility was within  $\pm 4\%$  on volume and  $\pm 2\%$  on both radius and depth. Centrifuging the soil samples prior to test provides an effective way to reconstitute in situ material properties in a reproducible manner.

SECTION 7  
REFERENCES

1. Scott, R. F. and N. R. Morgan, "Feasibility and Desirability of Constructing a Very Large Centrifuge for Geotechnical Studies," NSF Report 760-1/0 prepared under Grant ENG 75-18871, National Science Foundation, Washington, D. C., March 31, 1977. (See Bibliography which contains 151 pertinent references.)
2. Pokrovsky, G.I. and I. S. Fyodorov, Centrifugal Model Testing in the Construction Industry, Volumes I and II, "Niedra" Publishing House, Moscow, 1969. (Draft Translation prepared by Building Research Establishment Library Translation Service, Great Britain, August 1975.)
3. Viktorov, V. V. and R. D. Stepenov, "Modeling of the Action of an Explosion with Concentrated Charge in Homogeneous Ground," Inzh. Sb. 28, 87-96, 1960. (Translation: Sandia Report SCL-T-392, Albuquerque, NM 87115, 1969.)
4. Schmidt, R. M., "A Centrifuge Cratering Experiment: Development of a Gravity Scaled Yield Parameter," in Impact and Explosion Cratering (D. J. Roddy, R. O. Pepin and R. B. Merrill, eds.) Pergamon Press, New York, 1977.
5. Piekutowski, A. J., "Laboratory-Scale High-Explosive Cratering and Ejecta Phenomenology Studies," AFWL-TR-72-155, Air Force Weapons Laboratory, Albuquerque, NM, April 1974.
6. Piekutowski, A. J., "A Comparison of Cratering Effects for Lead Azide and PETN Explosive Charges," AFWL-TR-74-182, Air Force Weapons Laboratory, Albuquerque, NM, May 1975.
7. McKay, M. et al., "Development and Preliminary Tests of a Cratering and Ground Motion Simulation Technique," Defense Nuclear Agency Report DNA 3262F, Washington, D.C., Febr. 1974.
8. Stubbs, T. F., et al., "MINE THROW I--A Cratering and Ground Motion Simulation Technique," Defense Nuclear Agency Report DNA 3365F, Washington, D.C., July 1974.
9. Maxwell, D., et al., "JOHNIE BOY Crater Calculations," Defense Nuclear Agency Report DNA 3048F, Washington, D.C., April 1973.
10. Allen, R. T. and E. S. Gaffney, "Centrifuge Simulation of Large Yield Cratering Events," Final Report Defense Nuclear Agency Contract DNA 001-77-C-0116, Washington, D.C., Dec. 1977.
11. Allen, R. T., Oral presentation, Centrifuge Experiment Program Review Meeting, DNA Hdqrs., Alexandria, VA, 21 Sept. 1977.
12. Crowley, B. K., Scaling Criteria for Rock Dynamic Experiments, Symposium on Engineering with Nuclear Explosives, Vol. 1, p. 545-559, The American Nuclear Society and the United States Atomic Energy Commission, Las Vegas, NV, 1970.

13. Killian, R. G. and Germain, L. S., Scaling of Cratering Experiments - an Analytical and Heuristic Approach to the Phenomenology, Impact and Explosion Cratering, p. 1165-1190 (D. J. Roddy, R. O. Pepin and R. B. Merrill, eds.) Pergamon Press, New York, 1977.
14. Truesdell, C. and R. Toupin, "The Classical Field Theories," Handbuch der Physik, edited by S. Flugge, Springer-Verlag, Berlin, 1960, Vol. III/7.
15. Langhaar, H. L., Dimensional Analysis and Theory of Models, John Wiley & Sons, Inc., New York, 1951.
16. Serrin, J., "Mathematical Principles of Classical Fluid Mechanics," Handbuch der Physik, edited by S. Flugge, Springer-Verlag, Berlin, 1959, Vol. III/1, p. 243.
17. Oswatitsch, K., Physikalische Grundlagen der Stromungslehre, Handbuch der Physik, Vol. VIII/1, p. 60, edited by S. Flugge, Springer Verlag, 1959.
18. Truesdell, C. and W. Noll, "The Non-Linear Field Theories of Mechanics," Handbuch der Physik, edited by S. Flugge, Springer-Verlag, Berlin, 1965, Vol. III/3, p. 1.
19. Piekutowski, A. J., Personal Communication, May 1977.
20. Piekutowski, A. J., Personal Communication, Dec. 1977.
21. Goode, T. B. and A. L. Mathews: "Soils Survey"; Project 1.11, Operation Sun Beam, POR-2285, U.S. Army Waterways Experiment Station, Vicksburg, MS, March 1963.
22. Pinkston, J. M., Jr., "Earth Motion Measurements," Project 1.2, Operation Sun Beam, POR-2281, U. S. Army Waterways Experiment Station, Vicksburg, MS, Dec. 1963.

APPENDIX A  
CENTRIFUGE SHOT RECORDS

This section contains all the data for the elevated gravity centrifuge experiments. A table is given for each run which includes the test conditions for the two shots performed at the opposing rotor ends. Following each table is a figure which contains a comparison plot for the two craters as well as a set of stereo pairs for each and other documentary photographs. Run 14 was a demonstration shot using modeling clay and although the results were not discussed in this report it was included for future reference.

PRECEDING PAGE BLANK-NOT FILMED

Table A1. Ottawa sand centrifuge cratering data.

SHOT NUMBER	10-X	10-0
DATE	9 Aug. 77	9 Aug. 77
PURPOSE	charge comparison	charge comparison
CHARGE DESCRIPTION	CILAS-13 (B-1)	CICS-5 (B-1)
CHARGE WT. (gm)	1.7000 PbN <sub>6</sub>	.125 AgN <sub>3</sub> /.3601 PETN
CHARGE RADIUS (cm)	.508	.391
CHARGE CONFIGURATION	half-buried sphere	half-buried sphere
TEST BED MATERIAL	Ottawa Sawing Sand	Ottawa Sawing Sand
TEST BED DENSITY (gm/cc)	1.774	1.781
MOISTURE CONTENT	nom 0%	nom 0%
TEST BED GEOMETRY	homogeneous	homogeneous
CENTRIFUGE SPEED (rpm)	576	576
GROUND ZERO RADIUS (cm)	125	125
CENTRIFUGAL ACCELERATION (G's)	463	463
CRATER DIAMETER (cm)	7.74	7.12
CRATER RADIUS (cm)	3.87	3.56
MAX CRATER DEPTH (cm)	.89	.71
CRATER ASPECT RATIO (r/h)	4.35	5.01
CRATER VOLUME (cc)	27.05	17.14
LIP DIAMETER (cm)	10.16	8.64
LIP HEIGHT (cm)	.29	.25
LIP VOLUME (cc)	--	--

MEAN CRATER PROFILE

AVERAGE OF 4 RADIALS FOR EACH CRATER

RANGE (cm)	DEPTH (cm)	DEPTH (cm)
0.0	0.775	0.673
0.64	0.883	0.705
1.27	0.892	0.711
1.91	0.845	0.660
2.54	0.667	0.470
3.18	0.451	0.159
3.56	--	0.000
3.81	0.108	--
3.87	0.000	--
4.32	--	-0.245
5.08	-0.288	--

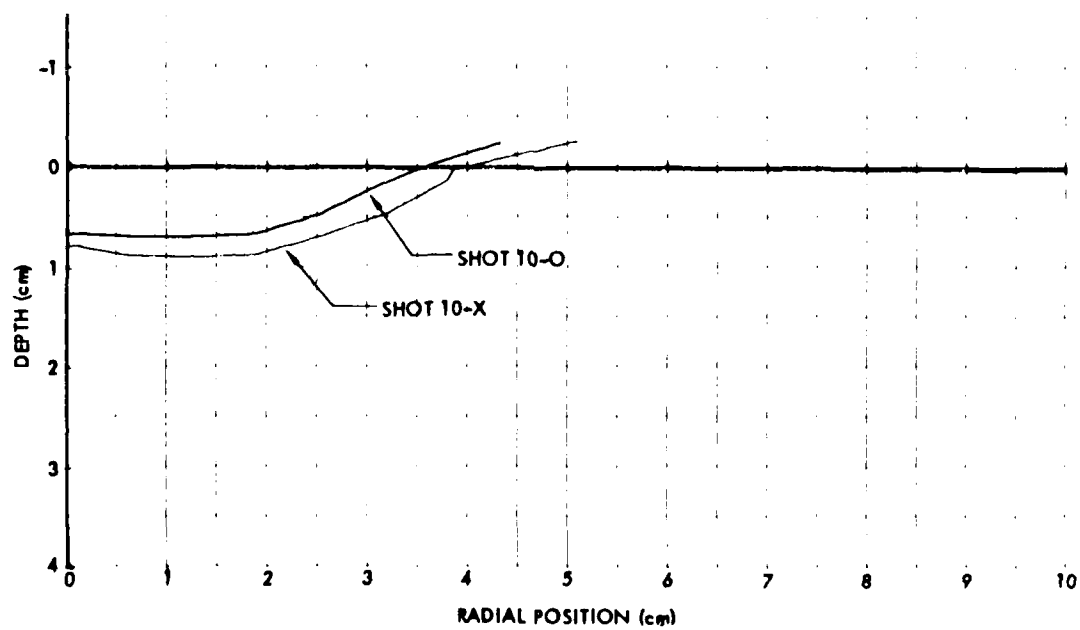


Figure A1. Comparison of crater 10-X (above) with crater 10-O (below).

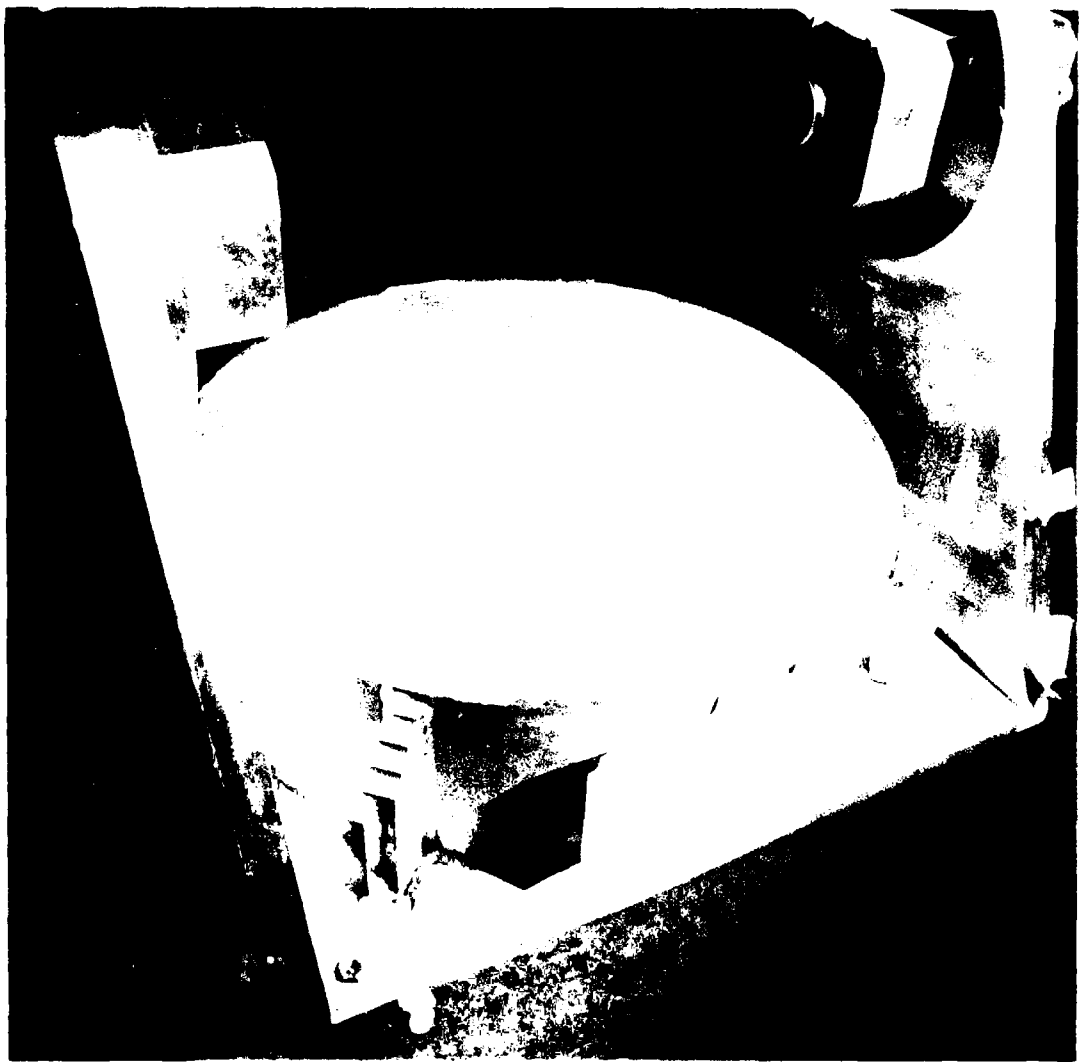


Figure A1. (Continued, crater 10-X).

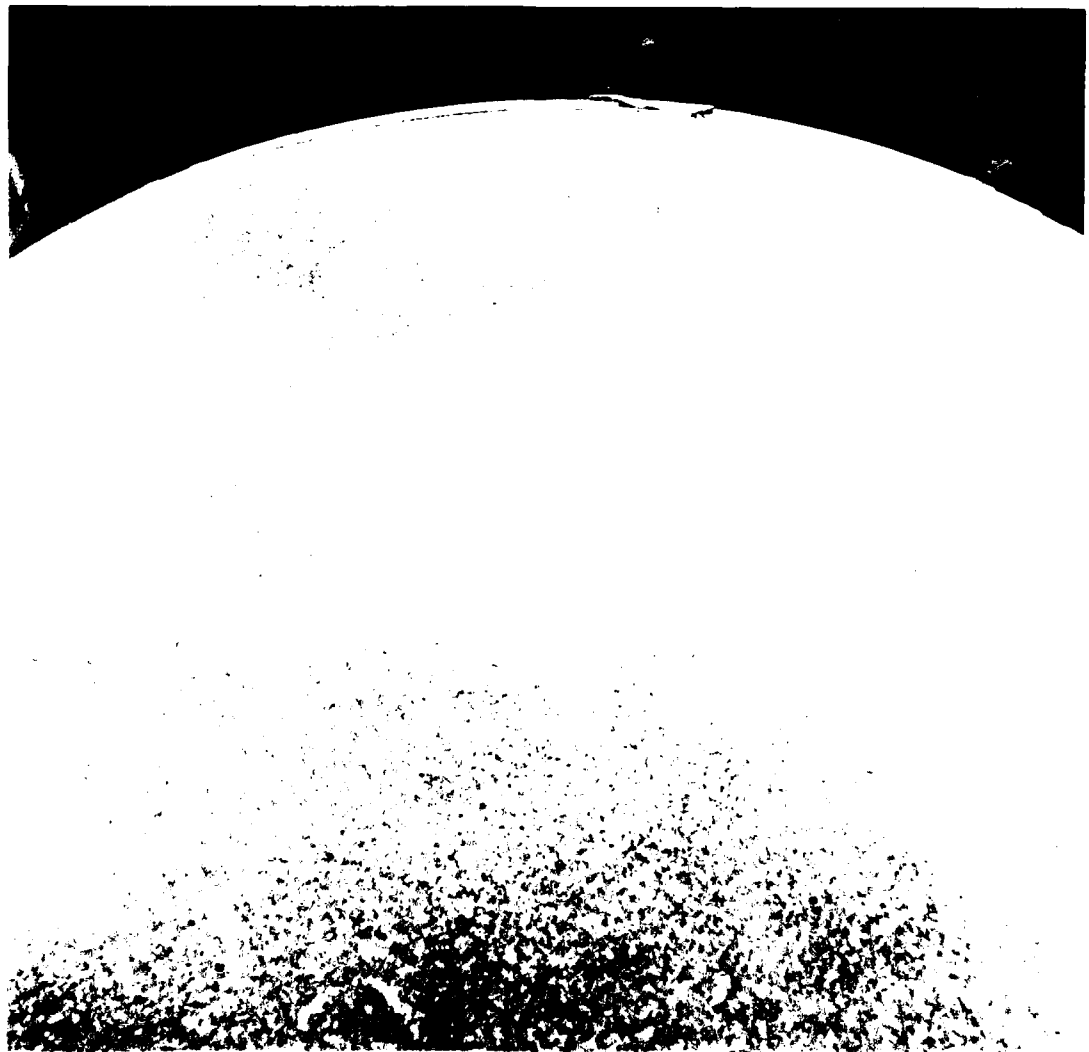


Figure A1. (Continued, crater 10-0).

Table A2. Ottawa sand centrifuge cratering data.

SHOT NUMBER	11-X	11-0
DATE	18 Aug. 77	18 Aug. 77
PURPOSE	reproducibility	reproducibility
CHARGE DESCRIPTION	CICS-1.265 (B-1)	CICS-1.265 (B-2)
CHARGE WT. (gm)	.125 AgN <sub>3</sub> /1.2302 PETN	.125 AgN <sub>3</sub> /1.2248 PETN
CHARGE RADIUS (cm)	.565	.565
CHARGE CONFIGURATION	half-buried sphere	half-buried sphere
TEST BED MATERIAL	Ottawa Flintshot	Ottawa Flintshot
TEST BED DENSITY (gm/cc)	1.776	1.781
MOISTURE CONTENT	nom 0%	nom 0%
TEST BED GEOMETRY	homogeneous	homogeneous
CENTRIFUGE SPEED (rpm)	568	568
GROUND ZERO RADIUS (cm)	125	125
CENTRIFUGAL ACCELERATION (G's)	451	451
CRATER DIAMETER (cm)	8.76	8.62
CRATER RADIUS (cm)	4.38	4.31
MAX CRATER DEPTH (cm)	.99	.97
CRATER ASPECT RATIO (r/h)	4.42	4.44
CRATER VOLUME (cc)	35.07	37.95
LIP DIAMETER (cm)	11.56	11.68
LIP HEIGHT (cm)	.33	.33
LIP VOLUME (cc)	--	--

MEAN CRATER PROFILE

AVERAGE OF 4 RADIALS FOR EACH CRATER

<u>RANGE (cm)</u>	<u>DEPTH (cm)</u>	<u>DEPTH (cm)</u>
0.0	0.991	0.927
0.64	0.908	0.965
1.27	0.775	0.902
1.91	0.819	0.927
2.54	0.794	0.895
3.18	0.654	0.705
3.81	0.394	0.394
4.38	0.000	--
4.57	--	0.000
5.78	-0.330	--
5.84	--	-0.330

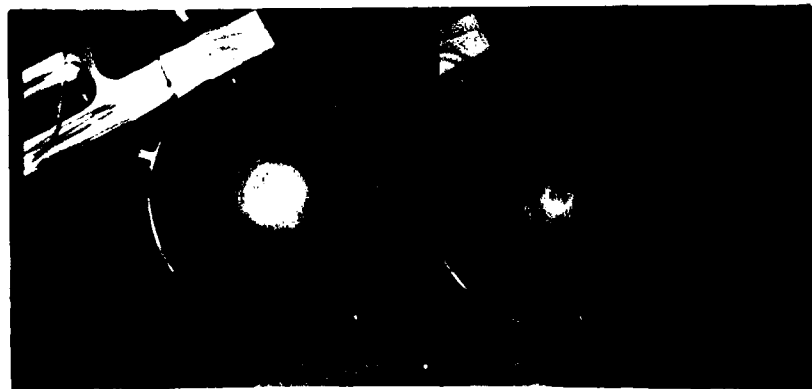
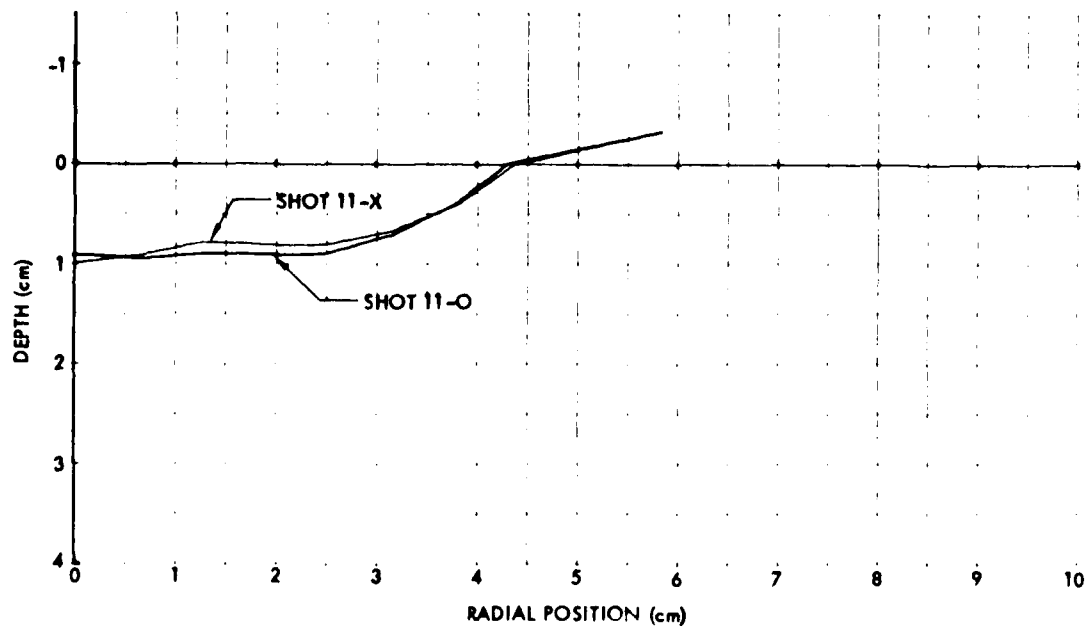


Figure A2. Comparison of crater 11-X (above) with crater 11-0 (below).

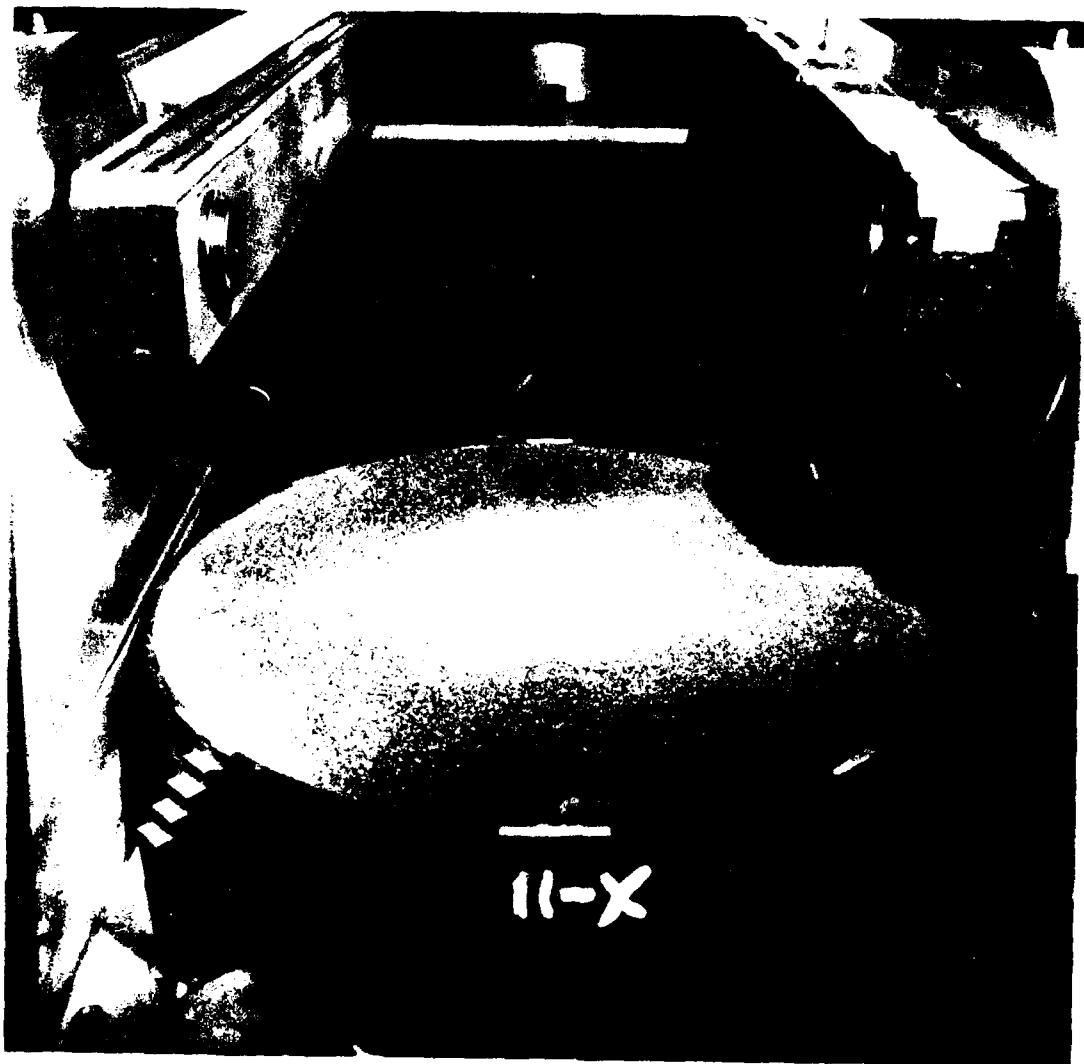


Figure A2. (Continued, crater 11-X).

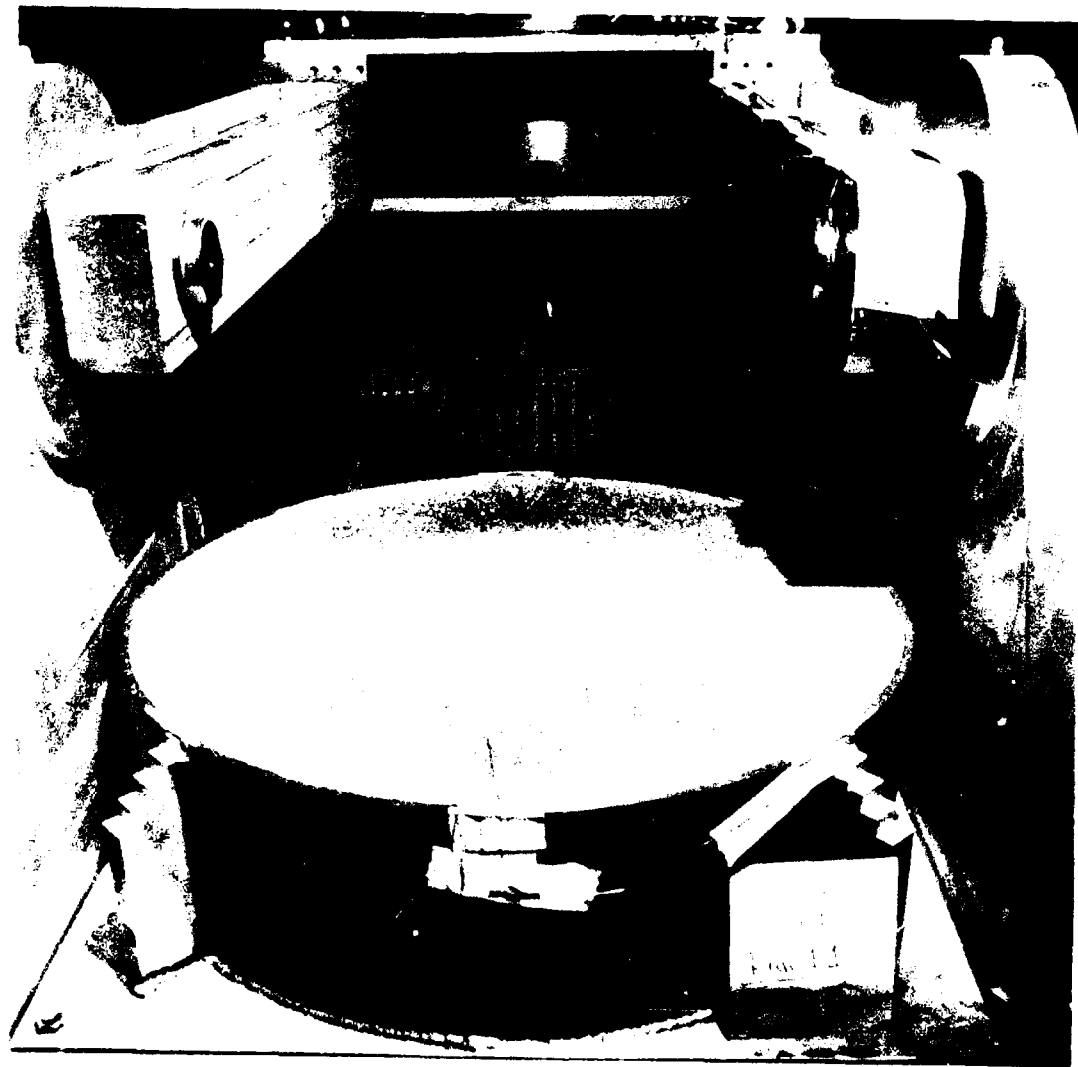


Figure A2. (Continued, crater 11-0).

Table A3. Ottawa sand centrifuge cratering data.

SHOT NUMBER	12-X	12-0
DATE	26 Aug. 77	26 Aug. 77
PURPOSE	Particle Size	Particle Size
CHARGE DESCRIPTION	CICS-4 (B-2)	CICS-4 (B-1)
CHARGE WT. (gm)	.125 AgN <sub>3</sub> /3.9441 PETN	.125 AgN <sub>3</sub> /3.9600 PETN
CHARGE RADIUS (cm)	.826	.826
CHARGE CONFIGURATION	half-buried sphere	half-buried sphere
TEST BED MATERIAL	Ottawa Banding Sand	Ottawa Flintshot
TEST BED DENSITY (gm/cc)	1.677	1.778
MOISTURE CONTENT	nom 0%	nom 0%
TEST BED GEOMETRY	homogeneous	homogeneous
CENTRIFUGE SPEED (rpm)	568	568
GROUND ZERO RADIUS (cm)	125	125
CENTRIFUGAL ACCELERATION (G's)	451	451
CRATER DIAMETER (cm)	12.66	12.82
CRATER RADIUS (cm)	6.33	6.41
MAX CRATER DEPTH (cm)	1.28	1.31
CRATER ASPECT RATIO (r/h)	4.95	4.89
CRATER VOLUME (cc)	96.32	101.45
LIP DIAMETER (cm)	16.00	16.00
LIP HEIGHT (cm)	.43	.44
LIP VOLUME (cc)	65.18	72.19

MEAN CRATER PROFILE

AVERAGE OF 8 RADIALS FOR EACH CRATER

RANGE (cm)	DEPTH (cm)	DEPTH (cm)
0.0	1.041	1.283
0.64	1.191	1.280
1.27	1.251	1.283
1.91	1.172	1.235
2.54	1.194	1.191
3.18	1.114	1.159
3.81	1.041	1.070
4.45	0.873	0.918
5.08	0.641	0.667
5.72	0.327	0.368
6.35	-0.013	0.176
6.99	-0.283	-0.238
7.62	-0.425	-0.406
8.26	-0.410	-0.438
8.89	-0.302	-0.337
9.53	-0.200	-0.260
10.16	-0.149	-0.171
10.80	-0.089	-0.127

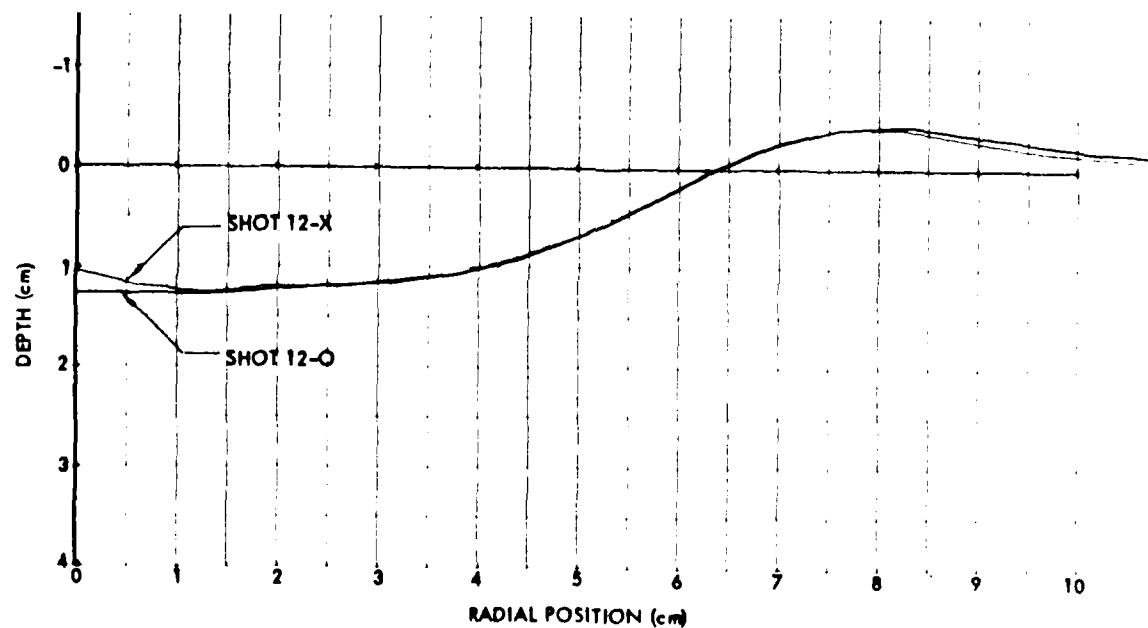


Figure A3. Comparison of crater 12-X (above) with crater 12-O (below).

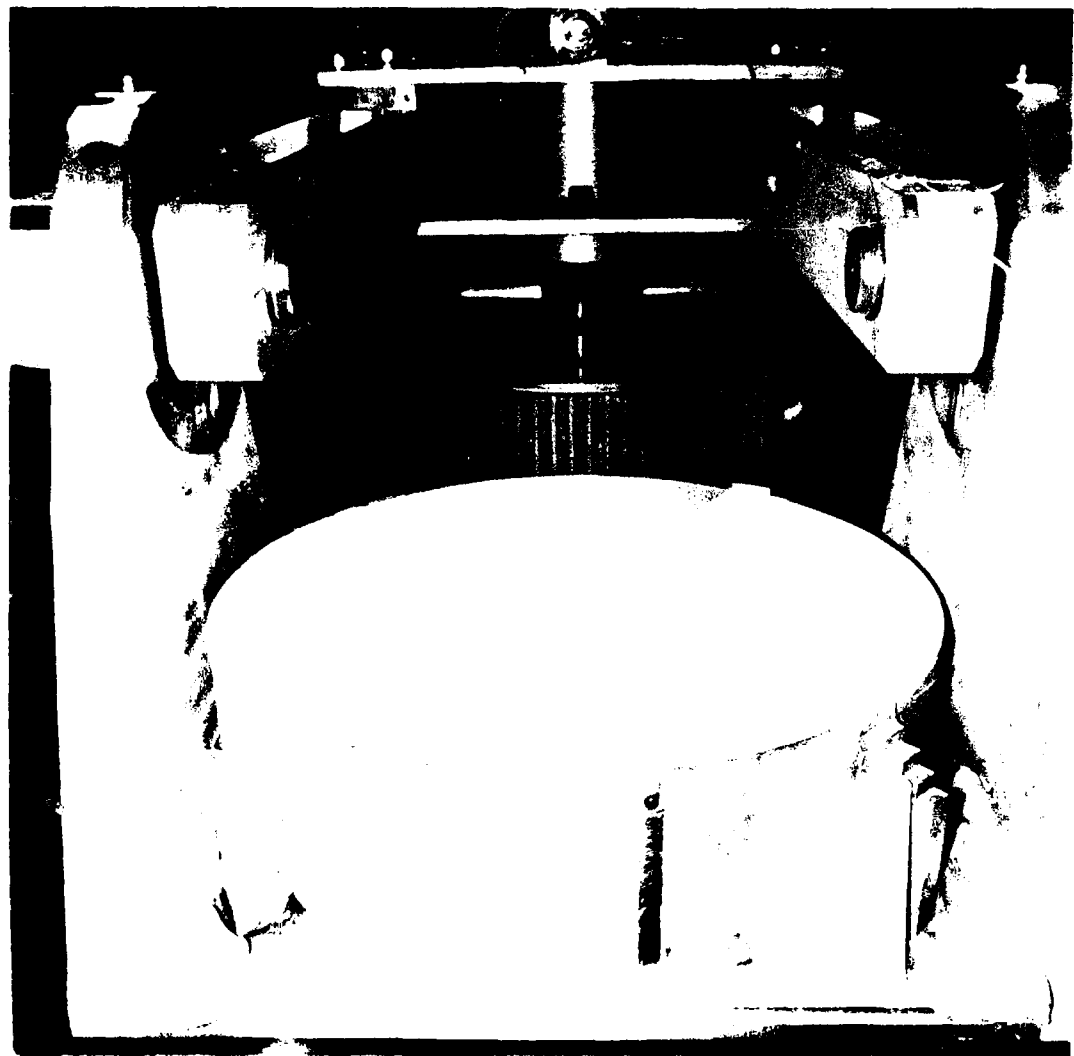


Figure A3. (Continued, crater 12-X).

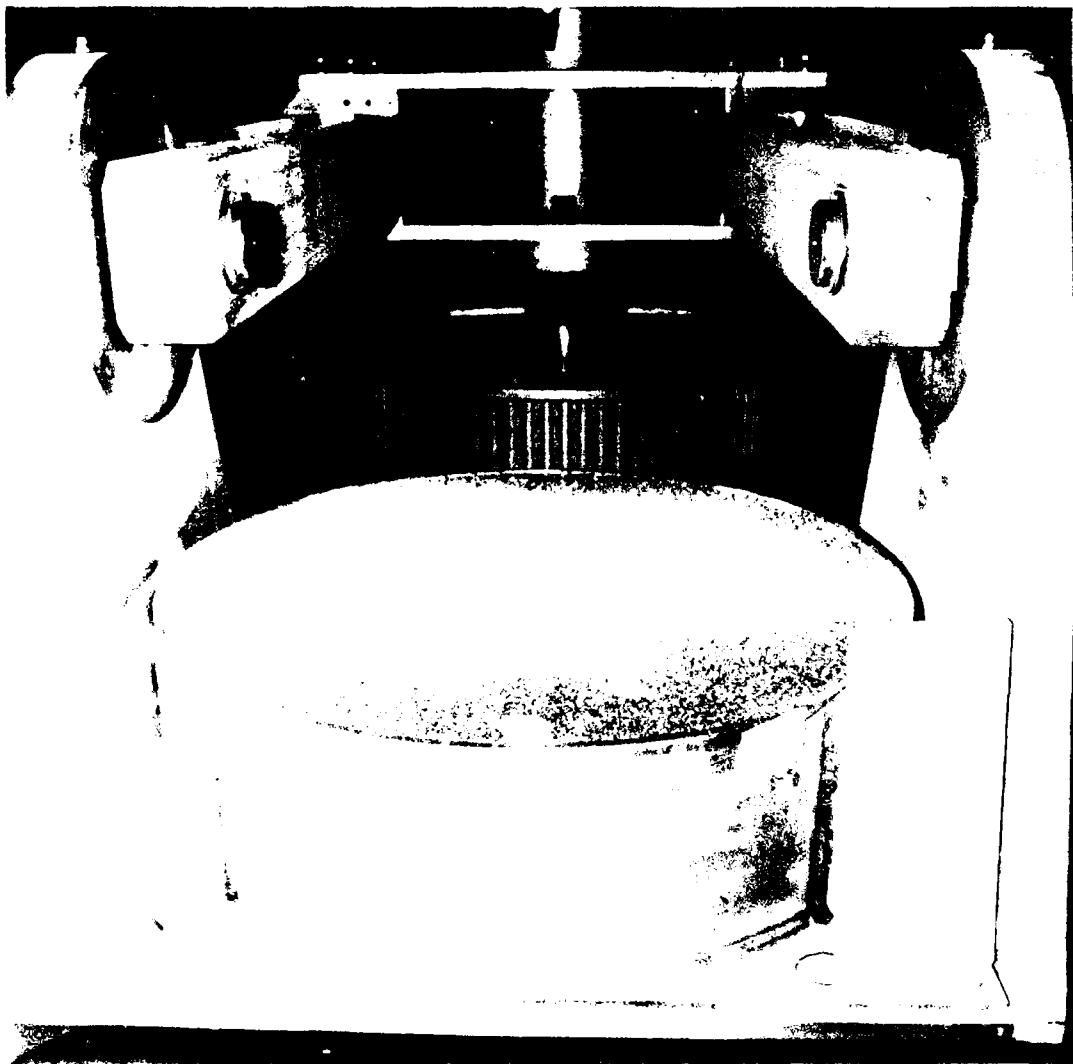


Figure A3. (Continued, crater 12-0).

Table A4. Ottawa sand centrifuge cratering data.

SHOT NUMBER	13-X	13-0
DATE	31 Aug. 77	31 Aug. 77
PURPOSE	particle size	$\pi_2$ test
CHARGE DESCRIPTION	CICS-4 (B-3)	CICS-4 (B-4)
CHARGE WT. (gm)	.125 AgN <sub>3</sub> /3.9477 PETN	.125 AgN <sub>3</sub> /3.9491 PETN
CHARGE RADIUS (cm)	.826	.826
CHARGE CONFIGURATION	half buried sphere	half buried sphere
TEST BED MATERIAL	Ottawa Banding Sand	Ottawa Flintshot
TEST BED DENSITY (gm/cc)	1.677	1.782
MOISTURE CONTENT	nom 0%	nom 0%
TEST BED GEOMETRY	homogeneous	homogeneous
CENTRIFUGE SPEED (rpm)	468	468
GROUND ZERO RADIUS (cm)	125	125
CENTRIFUGAL ACCELERATION (G's)	306	306
CRATER DIAMETER (cm)	13.30	13.76
CRATER RADIUS (cm)	6.65	6.88
MAX CRATER DEPTH (cm)	1.56	1.37
CRATER ASPECT RATIO (r/h)	4.26	5.02
CRATER VOLUME (cc)	119.30	125.57
LIP DIAMETER (cm)	17.20	16.40
LIP HEIGHT (cm)	.44	.44
LIP VOLUME (cc)	65.47	71.54

MEAN CRATER PROFILE

AVERAGE OF 8 RADIALS FOR EACH CRATER

<u>RANGE (cm)</u>	<u>DEPTH (cm)</u>	<u>DEPTH (cm)</u>
0.0	1.562	0.978
0.64	1.467	1.222
1.27	1.394	1.340
1.91	1.359	1.368
2.54	1.356	1.330
3.18	1.299	1.276
3.81	1.191	1.235
4.45	1.038	1.114
5.08	0.819	0.876
5.72	0.498	0.575
6.35	0.143	0.260
6.99	-0.156	-0.051
7.62	-0.362	-0.292
8.26	-0.419	-0.400
8.89	-0.359	-0.416
9.53	-0.254	-0.346
10.16	-0.181	-0.251
10.80	-0.130	-0.165

AD-A087 849

BOEING AEROSPACE CO SEATTLE WA

F/6 19/1

CENTRIFUGE CRATER SCALING EXPERIMENT I. DRY GRANULAR SOILS.(U)  
FEB 78 R M SCHMIDT, K A HOLSSAPLE

DNA001-77-C-0169

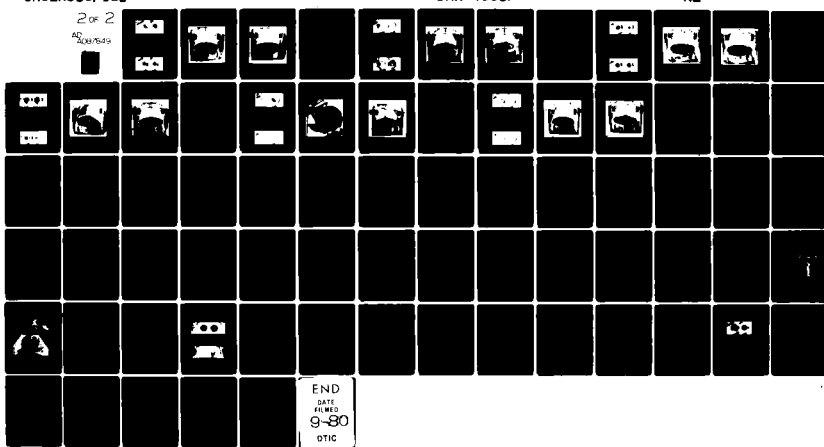
UNCLASSIFIED

DNA-4568F

NL

2 of 2

82-0849



END  
DATE  
9-80  
OTIC

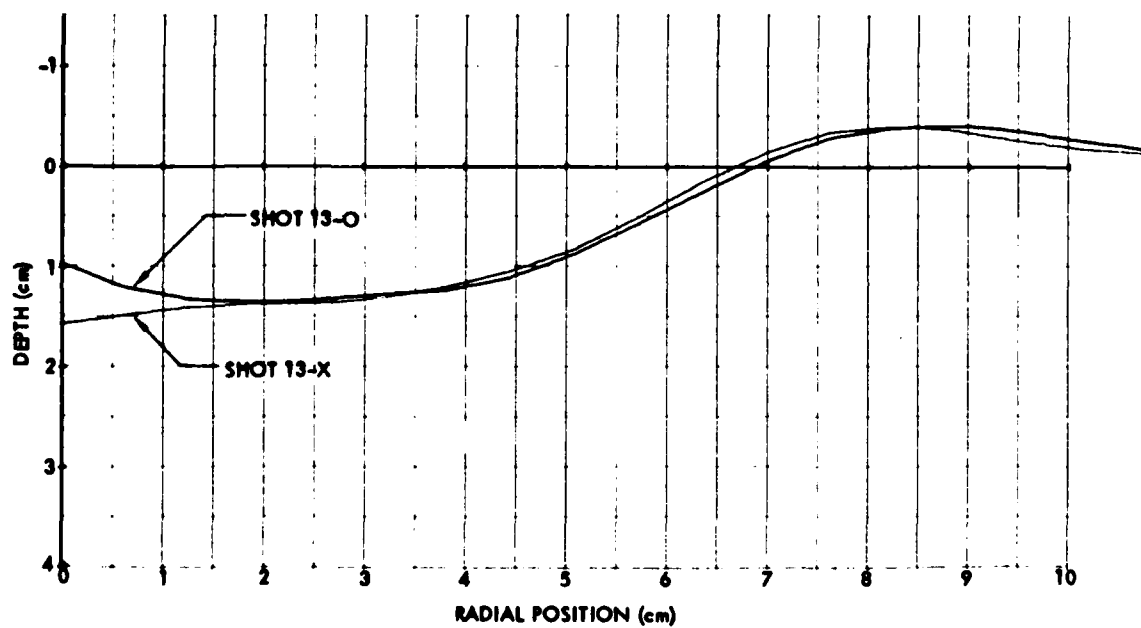


Figure A4. Comparison of crater 13-X (above) with crater 13-0 (below).



Figure A4. (Continued, crater 13-X).

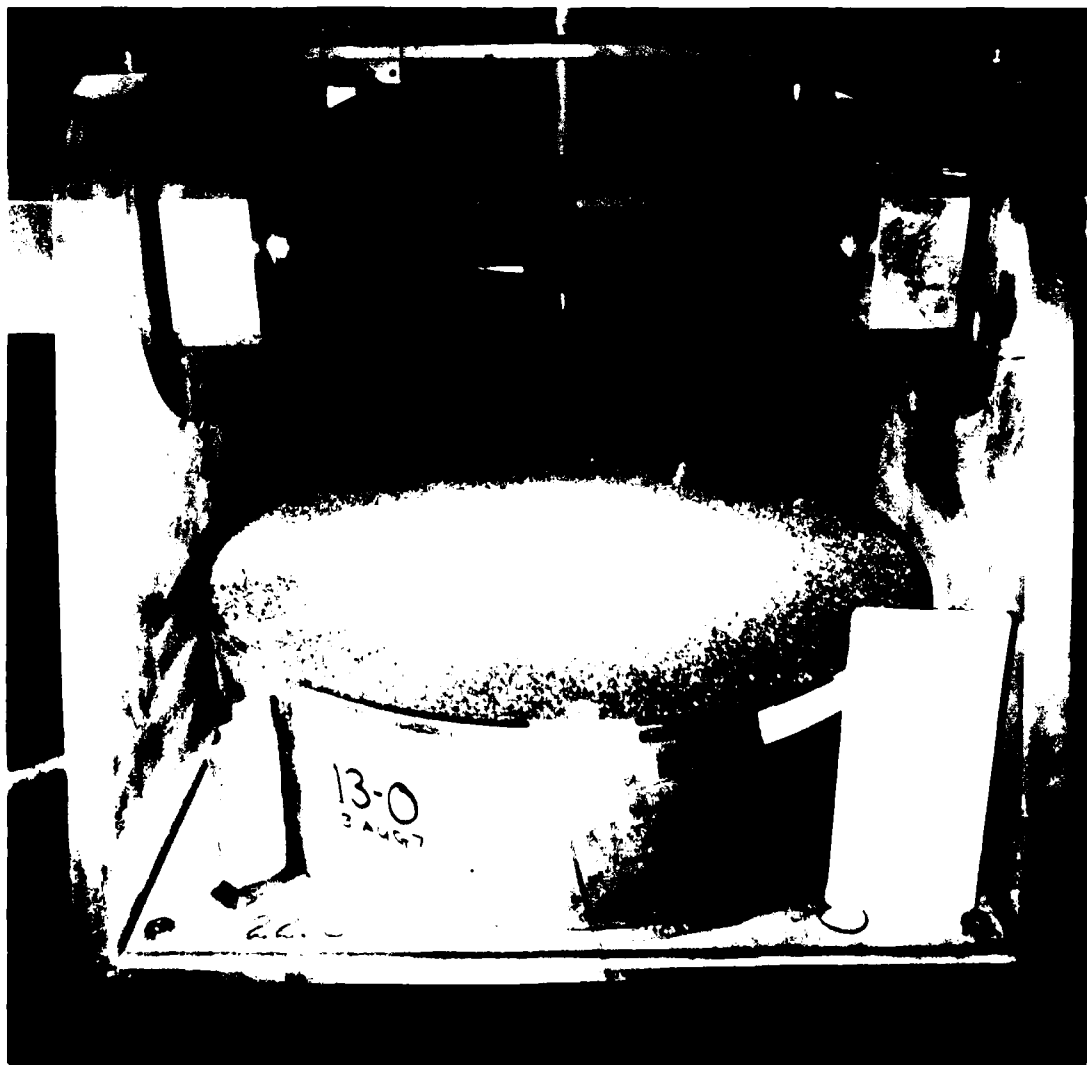


Figure A4. (Continued, crater 13-0).

Table A5. "Permaplast" clay centrifuge cratering data.

SHOT NUMBER	14-X	14-0
DATE	19 Sept. 77	19 Sept. 77
PURPOSE	$\pi_2$ test	$\pi_2$ test
CHARGE DESCRIPTION	CICS-4 (B-5)	CICS-1.265 (B-3)
CHARGE WT. (gm)	.125 AgN <sub>3</sub> /3.9401 PETN	.125 AgN <sub>3</sub> /1.2281 PETN
CHARGE RADIUS (cm)	.826	.565
CHARGE CONFIGURATION	half buried sphere	half buried sphere
TEST BED MATERIAL	"Permaplast" Clay	"Permaplast" Clay
TEST BED DENSITY (gm/cc)	1.53	1.53
MOISTURE CONTENT	--	--
TEST BED GEOMETRY	homogeneous	homogeneous
CENTRIFUGE SPEED (rpm)	471	571
GROUND ZERO RADIUS (cm)	124.5	124.5
CENTRIFUGAL ACCELERATION (G's)	309	454
CRATER DIAMETER (cm)	11.8	8.34
CRATER RADIUS (cm)	5.91	4.17
CRATER DEPTH (cm)	4.23	2.59
CRATER ASPECT RATIO (r/h)	1.40	1.61
CRATER VOLUME (cc)	244.	75.4 (+3)
LIP DIAMETER (cm)	14.4	10.1
LIP HEIGHT (cm)	1.22	.90
LIP VOLUME (cc)	79.3	35.0
MEAN CRATER PROFILE	AVERAGE OF 4 RADIALS FOR EACH CRATER	
RANGE (cm)	DEPTH (cm)	DEPTH (cm)
0.0	4.231	2.594
0.6	3.986	2.526
1.2	3.942	2.397
1.8	3.826	2.226
2.4	3.575	1.923
3.0	3.196	1.440
3.6	2.948	0.774
4.2	2.366	-0.045
4.8	1.590	-0.749
5.4	0.800	-0.824
6.0	-0.136	-0.430
6.6	-0.829	-0.046
7.2	-1.223	-0.049
7.8	-0.859	-0.059
8.4	-0.212	-0.061
9.0	0.008	-0.063
9.6	0.022	-0.065
10.2	0.033	-0.075

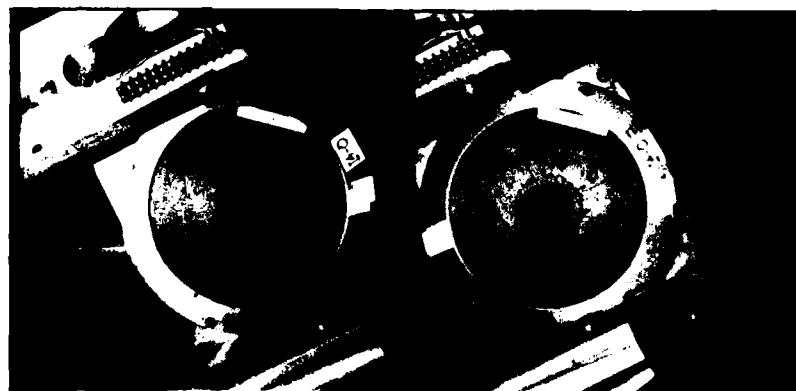
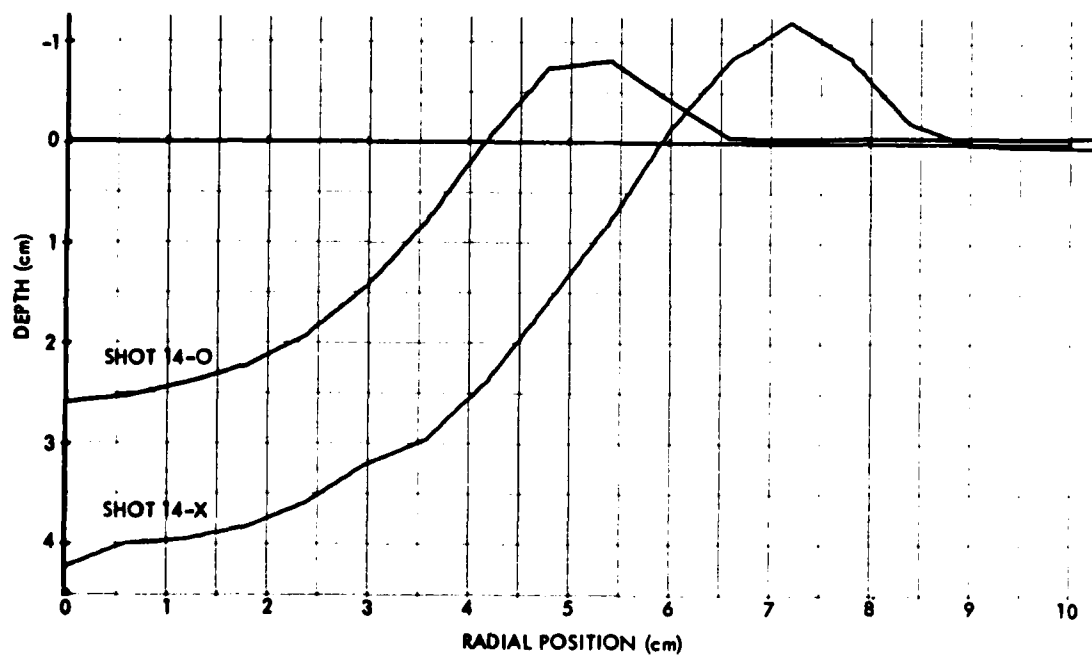


Figure A5. Comparison of crater 14-X (above) with crater 14-0 (below).



Figure A5. (Continued, crater 14-X).

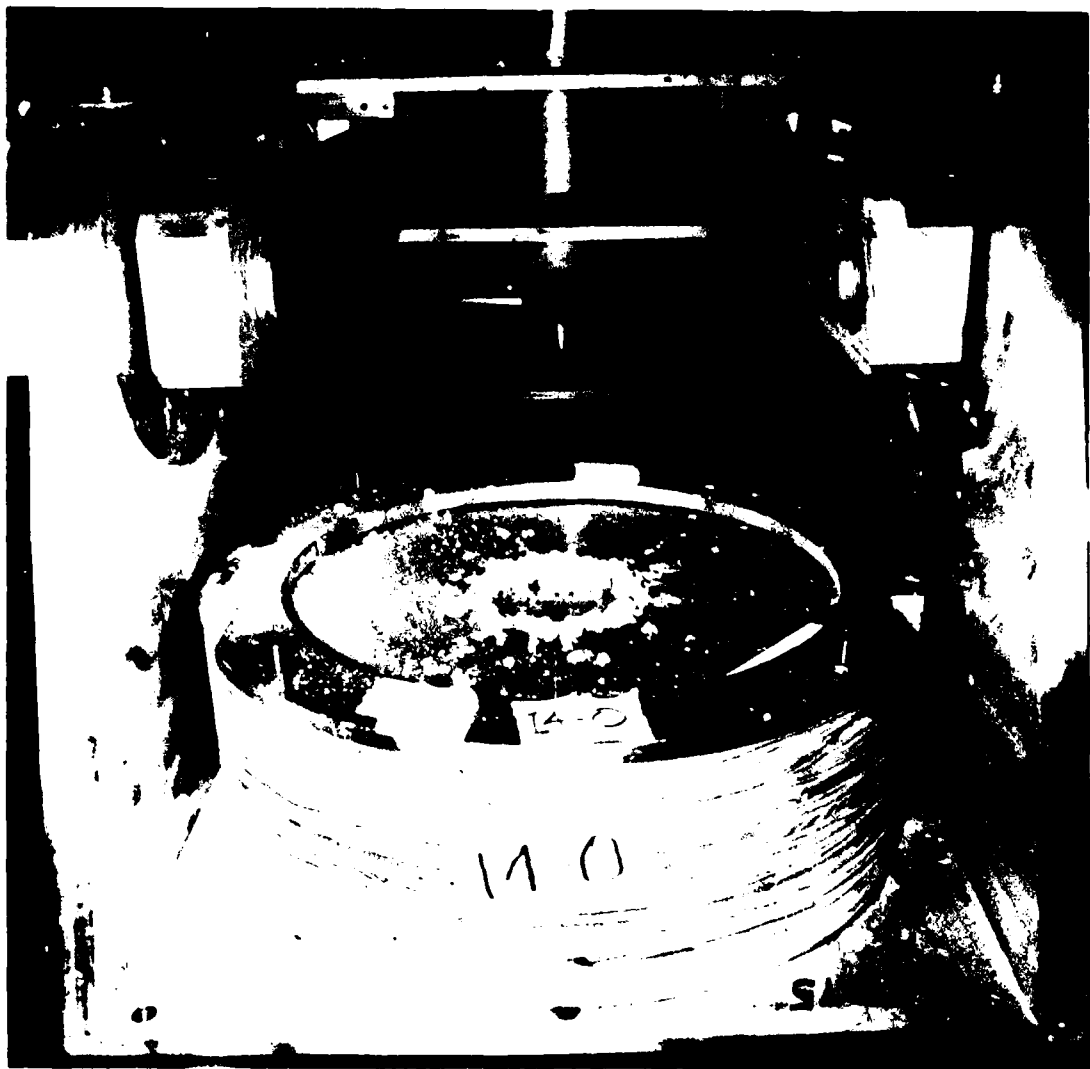


Figure A5. (Continued, crater 14-0).

Table A6. Ottawa sand centrifuge cratering data.

SHOT NUMBER	15-X	15-0
DATE	14 Oct. 77	14 Oct. 77
PURPOSE	scaling/reproducibility	scaling/reproducibility
CHARGE DESCRIPTION	CICS-5 (B-3)	CICS-5 (B-4)
CHARGE WT. (gm)	.125 AgN <sub>3</sub> / .3591 PETN	.125 AgN <sub>3</sub> / .3598 PETN
CHARGE RADIUS (cm)	.390	.390
CHARGE CONFIGURATION	half buried sphere	half buried sphere
TEST BED MATERIAL	Ottawa Flintshot	Ottawa Flintshot
TEST BED DENSITY (gm/cc)	1.784	1.784
MOISTURE CONTENT	nom 0%	nom 0%
TEST BED GEOMETRY	homogeneous	homogeneous
CENTRIFUGE SPEED (rpm)	84.6	84.6
GROUND ZERO RADIUS (cm)	125	125
CENTRIFUGAL ACCELERATION (G's)	10	10
CRATER DIAMETER (cm)	12.80	12.80
CRATER RADIUS (cm)	6.40	6.40
MAX CRATER DEPTH (cm)	1.26	1.27
CRATER ASPECT RATIO (r/h)	5.08	5.04
CRATER VOLUME (cc)	94.77	95.18
LIP DIAMETER (cm)	15.60+	15.60+
LIP HEIGHT (cm)	.35	.33
LIP VOLUME (cc)	85.66	78.87

MEAN CRATER PROFILE

AVERAGE OF 8 RADIALS FOR EACH CRATER

<u>RANGE (cm)</u>	<u>DEPTH (cm)</u>	<u>DEPTH (cm)</u>
0.0	1.045	1.130
0.6	1.089	1.122
1.2	1.189	1.206
1.8	1.239	1.236
2.4	1.261	1.267
3.0	1.221	1.222
3.6	1.107	1.107
4.2	0.933	0.918
4.8	0.689	0.686
5.4	0.412	0.421
6.0	0.148	0.147
6.6	-0.075	-0.074
7.2	-0.259	-0.252
7.8	-0.351	-0.326
8.4	-0.348	-0.320
9.0	-0.300	-0.294
9.6	-0.232	-0.217
10.2	-0.169	-0.162

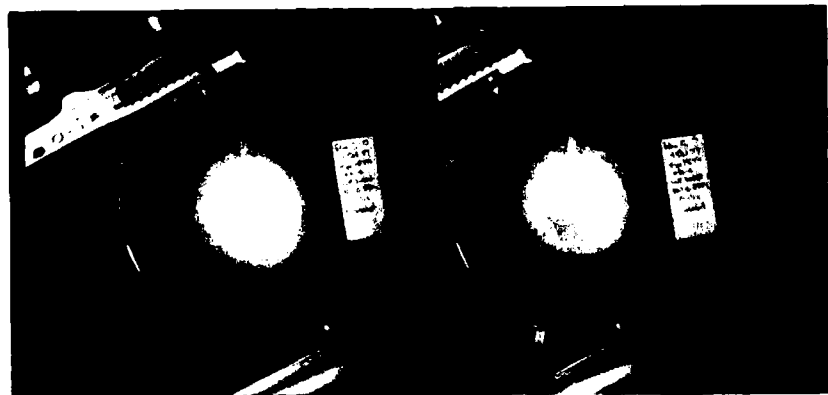
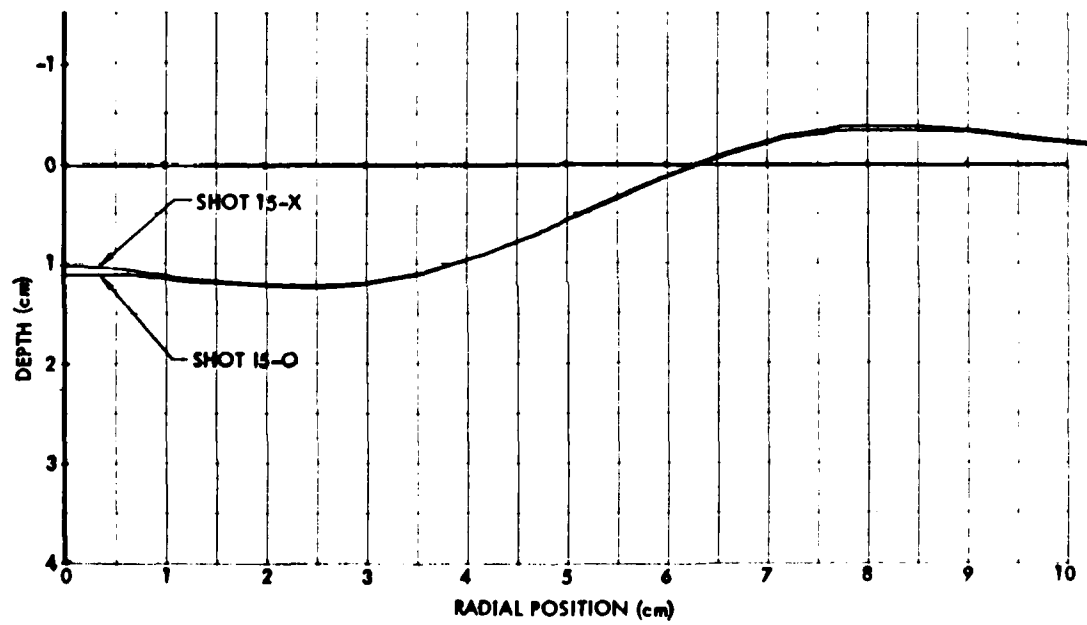
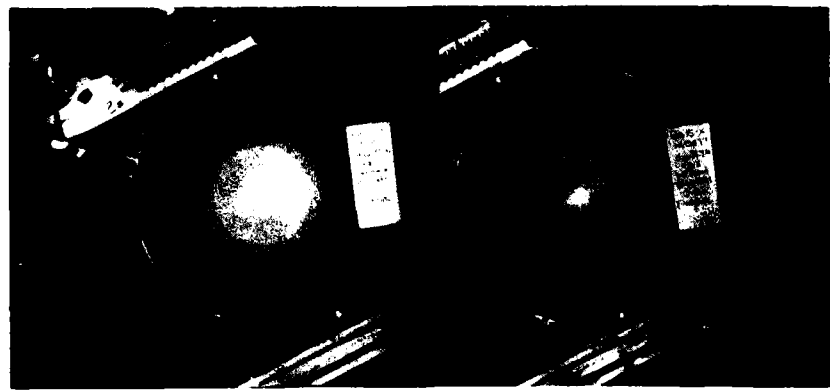


Figure A6. Comparison of crater 15-X (above) with crater 15-0 (below).



Figure A6. (Continued, crater 15-X).

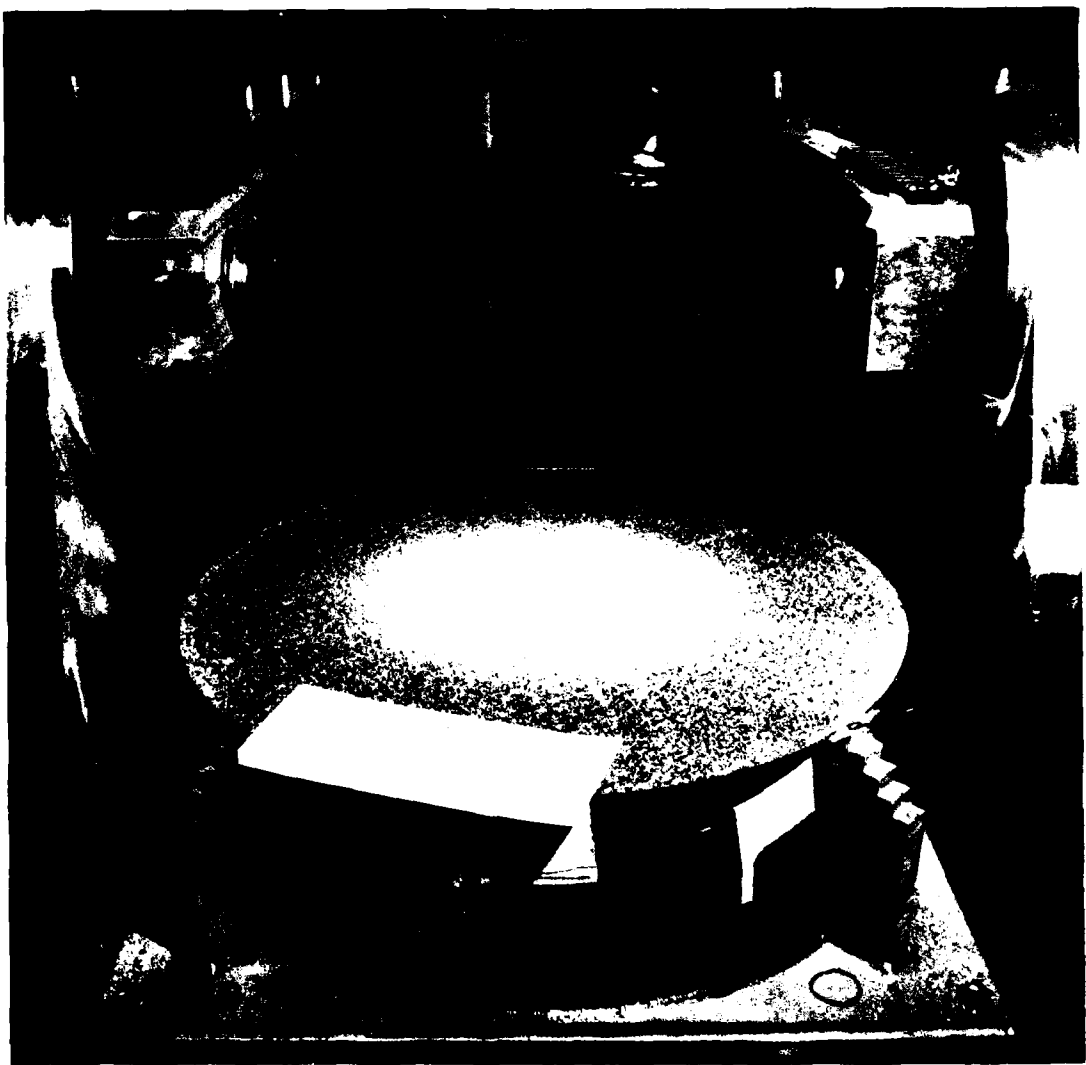


Figure A6. (Continued, crater 15-0).

Table A7. KAFB alluvium centrifuge cratering data.

SHOT NUMBER	16-X	16-0
DATE	3 Nov. 77	3 Nov. 77
PURPOSE	reproducibility	reproducibility
CHARGE DESCRIPTION	CICS-1.265 (B-9)	CICS-1.265 (B-11)
CHARGE WT. (gm)	.125 AgN <sub>3</sub> /1.2295 PETN	.125 AgN <sub>3</sub> /1.2353 PETN
CHARGE RADIUS (cm)	.565	.565
CHARGE CONFIGURATION	half buried sphere	half buried sphere
TEST BED MATERIAL	KAFB Desert Alluvium	KAFB Desert Alluvium
TEST BED DENSITY (gm/cc)	1.449	1.429
MOISTURE CONTENT	4.1%	4.1%
TEST BED GEOMETRY	homogeneous	homogeneous
CENTRIFUGE SPEED (rpm)	568	568
GROUND ZERO RADIUS (cm)	125	125
CENTRIFUGAL ACCELERATION (G's)	451	451
CRATER DIAMETER (cm)	9.40	9.56
CRATER RADIUS (cm)	4.70	4.78
MAX CRATER DEPTH (cm)	1.91	2.08
CRATER ASPECT RATIO (r/h)	2.46	2.30
CRATER VOLUME (cc)	48.11	50.95
LIP DIAMETER (cm)	10.80	10.80
LIP HEIGHT (cm)	.18	.15
LIP VOLUME (cc)	--	--

MEAN CRATER PROFILE

AVERAGE OF 4 RADIALS FOR EACH CRATER

<u>RANGE (cm)</u>	<u>DEPTH (cm)</u>	<u>DEPTH (cm)</u>
0.0	1.908	2.075
0.6	1.942	2.037
1.2	1.862	1.861
1.8	1.550	1.512
2.4	0.898	0.980
3.0	0.681	0.669
3.6	0.434	0.487
4.2	0.173	0.223
4.8	-0.035	0.008
5.4	-0.179	-0.144
6.0	-0.142	-0.108
6.6	-0.067	-0.029
7.2	-0.027	-0.008
7.8	-0.013	0.000
8.4	-0.012	0.006
9.0	-0.013	0.000
9.6	-0.013	0.003
10.2	-0.010	-0.004

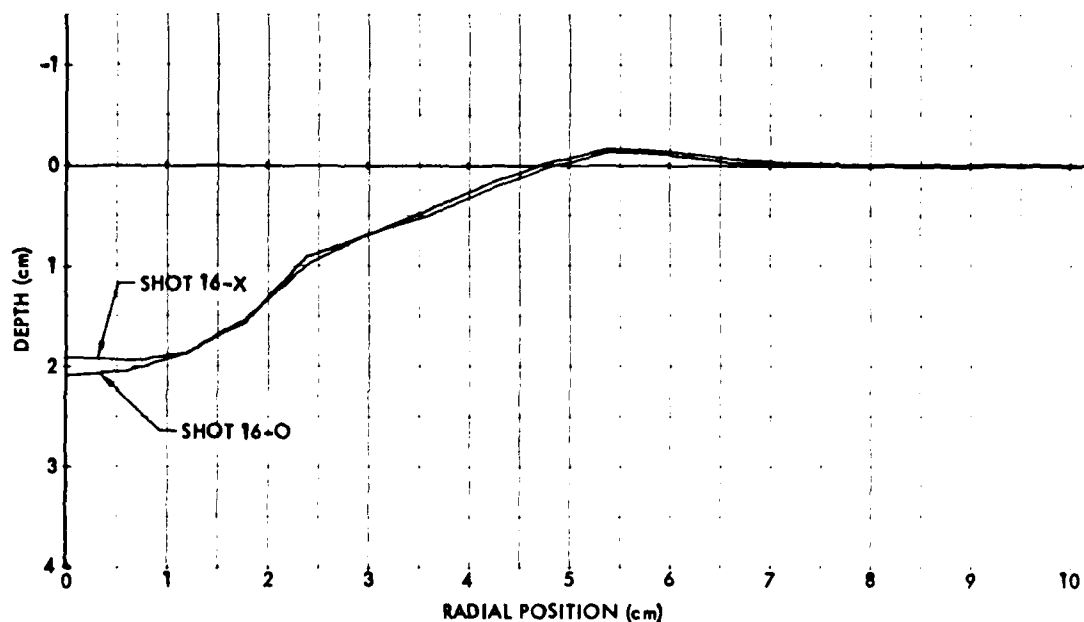


Figure A7. Comparison of crater 16-X (above) with crater 16-0 (below).

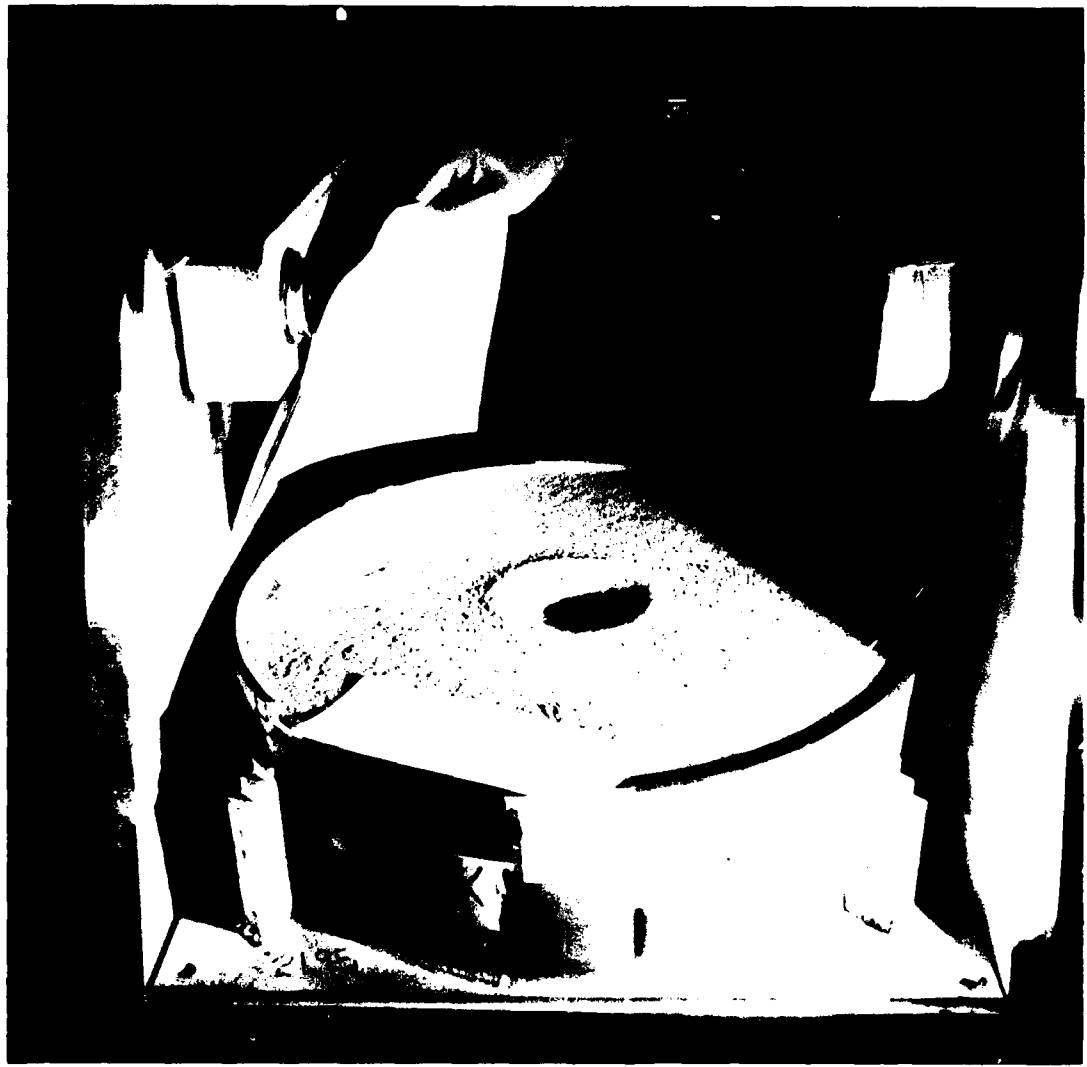


Figure A7. (Continued, crater 16-X).

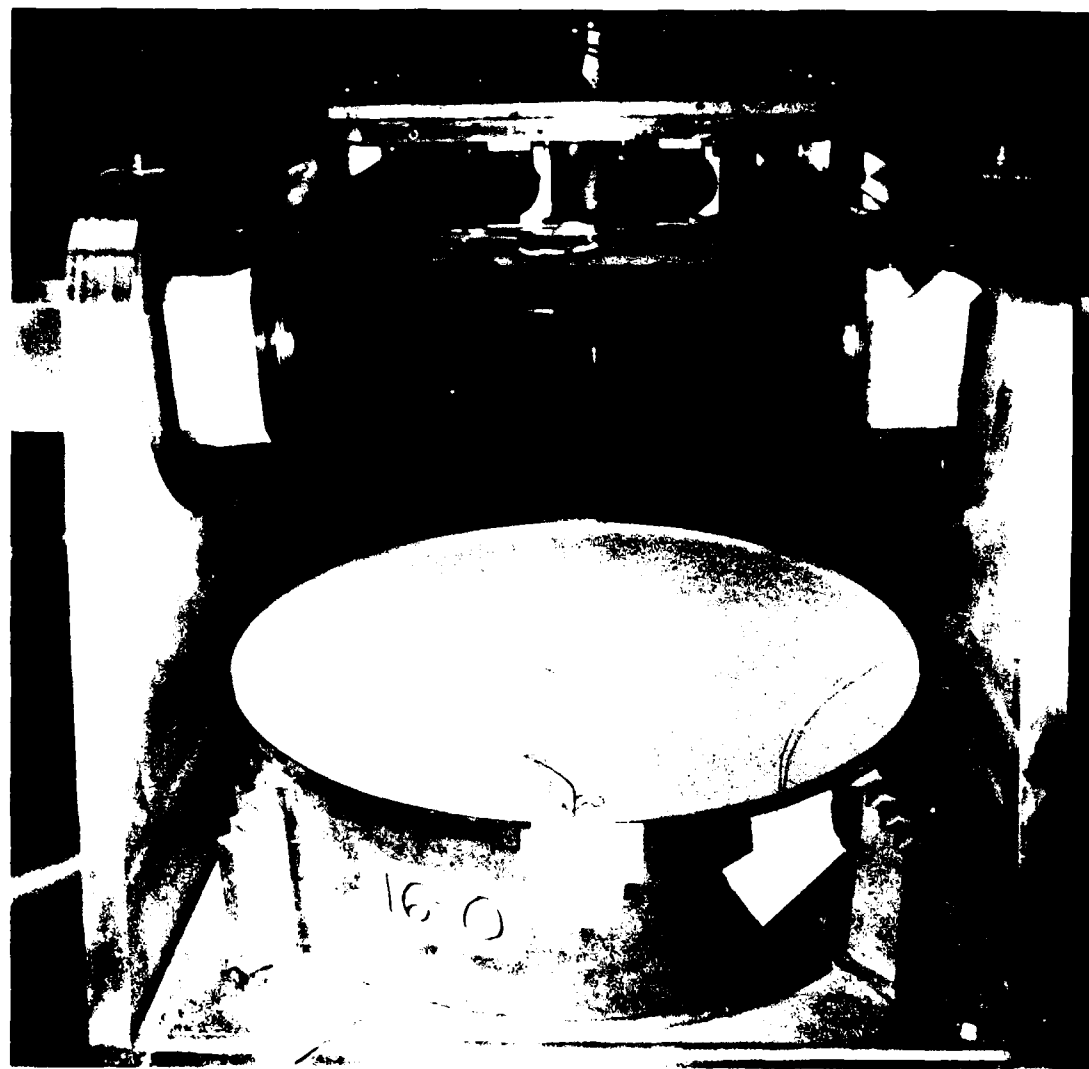


Figure A7. (Continued, crater 16-0).

Table A8. KAFB alluvium centrifuge cratering data.

SHOT NUMBER	17-X	17-0
DATE	18 Nov. 77	18 Nov. 77
PURPOSE	$\pi_2$ test	$\pi_2$ test
CHARGE DESCRIPTION	CICS-1.265 (B-15)	CICS-4 (B-11)
CHARGE WT. (gm)	.125 AgN <sub>3</sub> /1.2281 PETN	.125 AgN <sub>3</sub> /3.9395 PETN
CHARGE RADIUS (cm)	.565	.826
CHARGE CONFIGURATION	half buried sphere	half buried sphere
TEST BED MATERIAL	KAFB Alluvium	KAFB Alluvium
TEST BED DENSITY (gm/cc)	1.607	1.609
MOISTURE CONTENT	2.65%	2.65%
TEST BED GEOMETRY	homogeneous	homogeneous
CENTRIFUGE SPEED (rpm)	568	468
GROUND ZERO RADIUS (cm)	125	125
CENTRIFUGAL ACCELERATION (G's)	451	306
CRATER DIAMETER (cm)	8.44	12.45
CRATER RADIUS (cm)	4.22	6.23
MAX CRATER DEPTH (cm)	1.35	1.97
CRATER ASPECT RATIO (r/h)	3.13	3.16
CRATER VOLUME (cc)	30.23	96.50
LIP DIAMETER (cm)	10.60	15.00
LIP HEIGHT (cm)	.26	.33
LIP VOLUME (cc)	21.34	63.25
MEAN CRATER PROFILE	AVERAGE OF 8 RADIALS FOR EACH CRATER	
<u>RANGE (cm)</u>	<u>DEPTH (cm)</u>	<u>DEPTH (cm)</u>
0	1.227	1.986
.6	1.355	1.937
1.2	1.342	1.947
1.8	0.917	1.797
2.4	0.613	1.547
3.0	0.488	1.183
3.6	0.263	0.954
4.2	0.013	0.781
4.8	-0.201	0.578
5.4	-0.250	0.335
6.0	-0.161	0.090
6.6	-0.094	-0.139
7.2	-0.060	-0.315
7.8	-0.042	-0.339
8.4	-0.025	-0.274
9.0	-0.016	-0.209
9.6	-0.009	-0.155
10.2	-0.008	-0.113

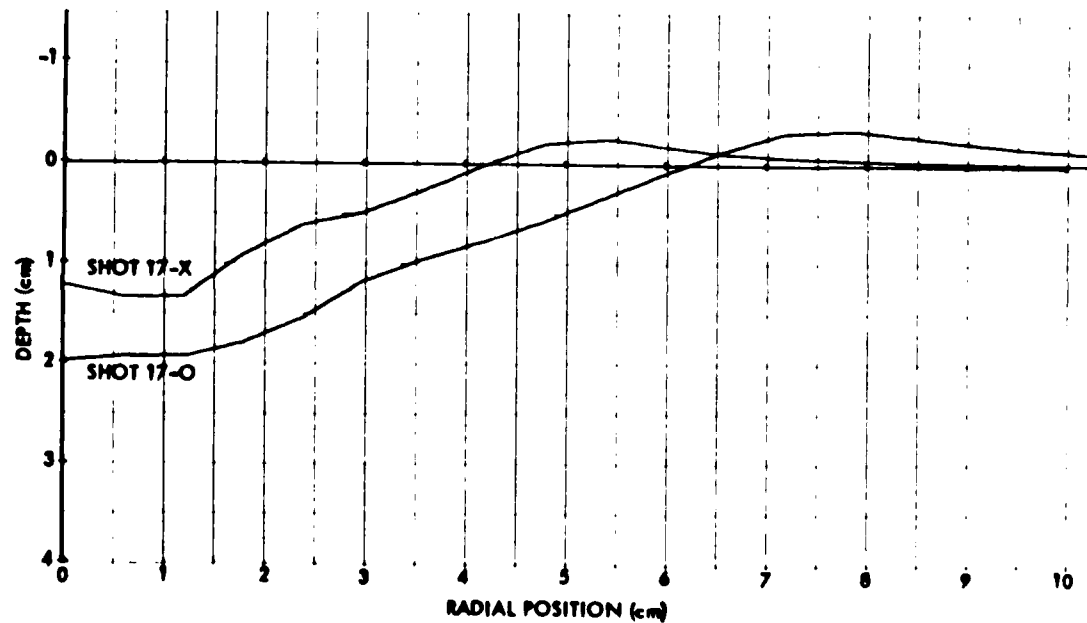


Figure A8. Comparison of crater 17-X (above) with crater 17-0 (below).



Figure A8. (Continued, crater 17-X).

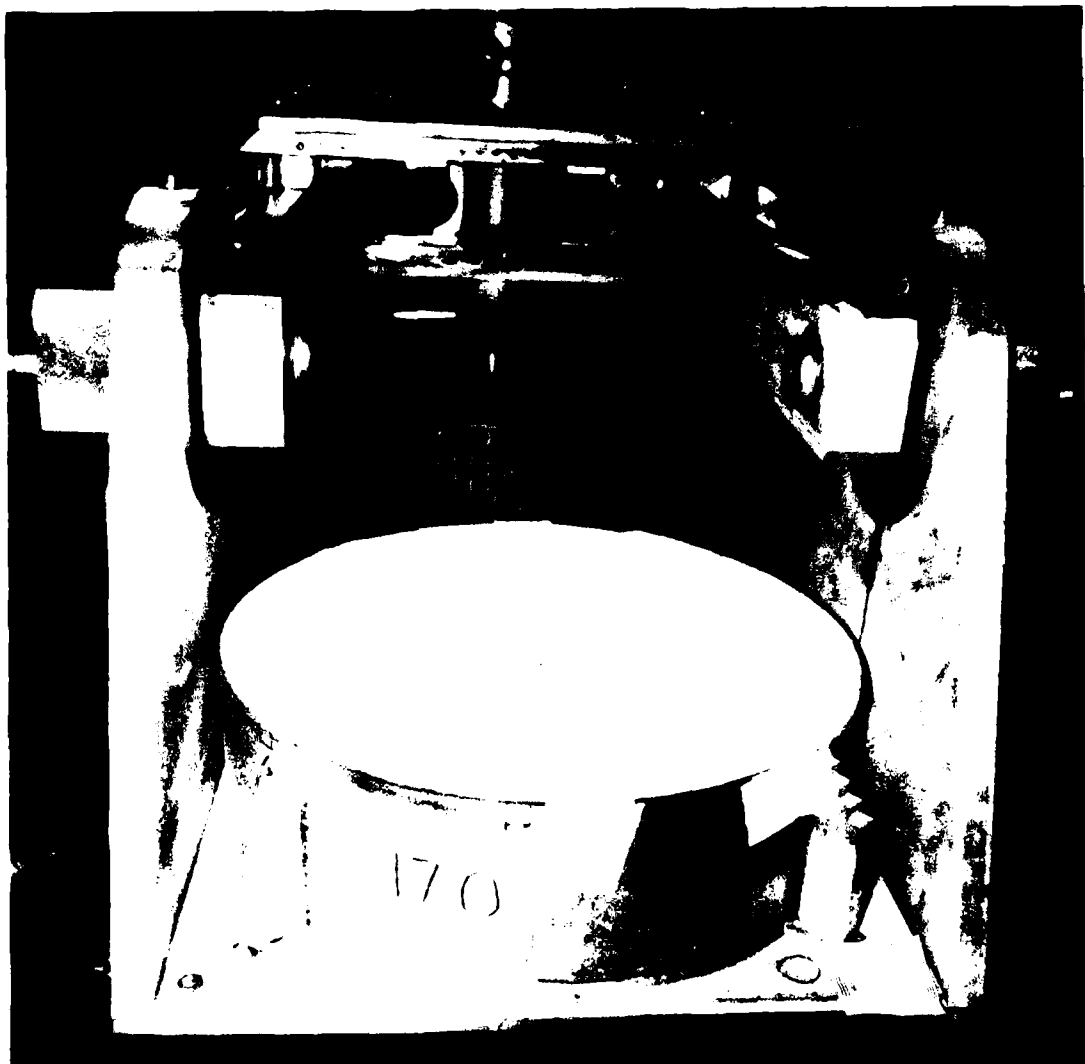


Figure A8. (Continued, crater 17-0).

Table A9. KAFB alluvium centrifuge cratering data.

SHOT NUMBER	18-X	18-0
DATE	2 Dec. 77	2 Dec. 77
PURPOSE	Johnnie Boy Simulation 2	Johnnie Boy Simulation 1
CHARGE DESCRIPTION	CICS-1.265 (B-17)	CICS-1.265 (B-16)
CHARGE WT. (gm)	.125 AgN <sub>3</sub> /1.2243 PETN	.125 AgN <sub>3</sub> /1.2251 PETN
CHARGE RADIUS (cm)	.565	.565
CHARGE CONFIGURATION	.845 cm DOB (sphere)	.362 cm DOB (sphere)
TEST BED MATERIAL	KAFB Alluvium	KAFB Alluvium
TEST BED DENSITY (gm/cc)	1.576	1.570
MOISTURE CONTENT	4.2%	4.1%
TEST BED GEOMETRY	homogeneous	homogeneous
CENTRIFUGE SPEED (rpm)	497	497
GROUND ZERO RADIUS (cm)	125	125
CENTRIFUGAL ACCELERATION (G's)	345	345
CRATER DIAMETER (cm)	12.16	10.74
CRATER RADIUS (cm)	6.08	5.37
MAX CRATER DEPTH (cm)	2.76	2.26
CRATER ASPECT RATIO (r/h)	2.20	2.38
CRATER VOLUME (cc)	116.04	77.74
LIP DIAMETER (cm)	15.00	13.20
LIP HEIGHT (cm)	.37	.32
LIP VOLUME (cc)	53.89	35.18

MEAN CRATER PROFILE

AVERAGE OF 8 RADIALS FOR EACH CRATER

<u>RANGE (cm)</u>	<u>DEPTH (cm)</u>	<u>DEPTH (cm)</u>
0.0	2.762	2.257
0.6	2.760	2.252
1.2	2.643	2.201
1.8	2.352	1.891
2.4	1.970	1.454
3.0	1.449	0.982
3.6	1.086	0.761
4.2	0.852	0.554
4.8	0.615	0.312
5.4	0.333	0.017
6.0	0.033	-0.219
6.6	-0.218	-0.322
7.2	-0.369	-0.273
7.8	-0.365	-0.171
8.4	-0.244	-0.113
9.0	-0.162	-0.074
9.6	-0.112	-0.046
10.2	-0.069	-0.023

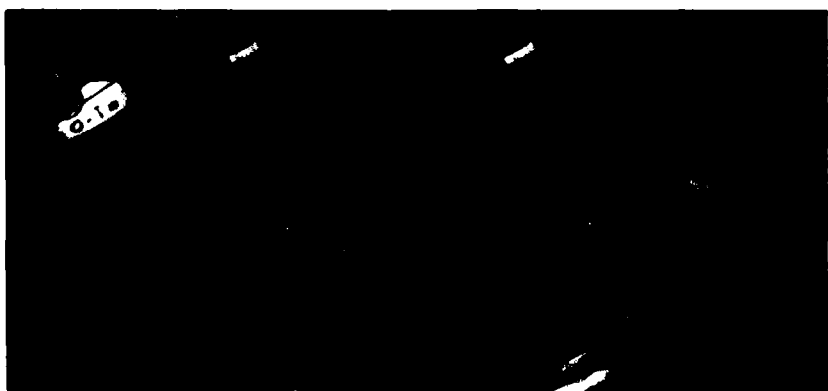
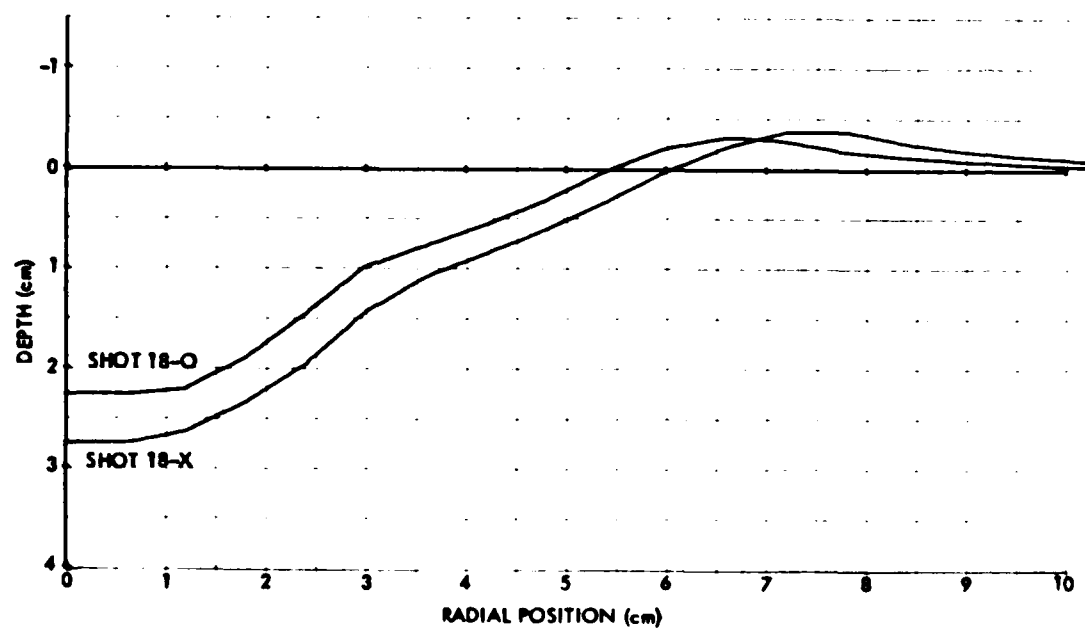


Figure A9. Comparison of crater 18-X (above) with crater 18-O (below).



Figure A9. (Continued, crater 18-X).



Figure A9. (Continued, crater 18-0).

APPENDIX B  
UDRI 1-G CONTROL SHOT RECORDS

This section is a compilation of various 1-G cratering data generated by A. J. Piekutowski of UDRI. The data for the larger PETN shots in both the Ottawa sand and the KAFB alluvium was generated in direct support of this program through arrangements with R. W. Henny of AFWL. The data for the 1.7 gm lead azide and the 0.4 gm PETN shots in Ottawa sand are from references 5 and 6. The other data was transmitted as a personal communication from A. J. Piekutowski.<sup>20</sup>

PRECEDING PAGE BLANK-NOT FILMED

Table B1. Ottawa sand 1G control shots, 1.7 grams lead azide.

SHOT NUMBER	UDRI-9	UDRI-22
DATE	20 Jan. 72	9 Feb. 72
PURPOSE	AFWL-TR-72-155	AFWL-TR-72-155
CHARGE DESCRIPTION	CILAS-13 (22)	CILAS-13 (106)
CHARGE WT. (gm)	1.6961 PbN <sub>6</sub>	1.7096 PbN <sub>6</sub>
CHARGE RADIUS (cm)	.508	.508
CHARGE CONFIGURATION	half buried sphere	half buried sphere
TEST BED MATERIAL	Ottawa Flintshot	Ottawa Flintshot
TEST BED DENSITY (gm/cc)	1.802	1.802
MOISTURE CONTENT	nom. 0%	nom. 0%
TEST BED GEOMETRY	homogeneous	homogeneous
CRATER DIAMETER (cm)	20.4	20.2
CRATER RADIUS (cm)	10.2	10.1
MAX. CRATER DEPTH (cm)	2.29	2.35
CRATER ASPECT RATIO (r/h)	4.45	4.30
CRATER VOLUME (cc)	436.	420.
LIP DIAMETER (cm)	260.	26.
LIP HEIGHT (cm)	.669	.763
LIP VOLUME (cm <sup>3</sup> )	321.	461.

MEAN CRATER PROFILE

AVERAGE OF 8 RADIALS FOR EACH CRATER

<u>RANGE (cm)</u>	<u>DEPTH (cm)</u>	<u>DEPTH (cm)</u>
0.0	1.963	1.950
1.0	1.988	2.069
2.0	2.181	2.306
3.0	2.288	2.350
4.0	2.263	2.300
5.0	2.131	2.106
6.0	1.894	1.825
7.0	1.513	1.413
8.0	1.094	0.975
9.0	0.550	0.463
10.0	0.094	0.038
11.0	-0.338	-0.406
12.0	-0.581	-0.650
13.0	-0.669	-0.763
14.0	-0.575	-0.675
15.0	-0.431	-0.531
16.0	-0.338	-0.431
17.0	-0.250	-0.319
18.0	-0.163	-0.244
19.0	-0.088	-0.181
20.0	-0.069	-0.188
21.0	-0.050	-0.175
22.0	-0.025	-0.119
23.0	-0.013	-0.106
24.0	0.000	-0.106

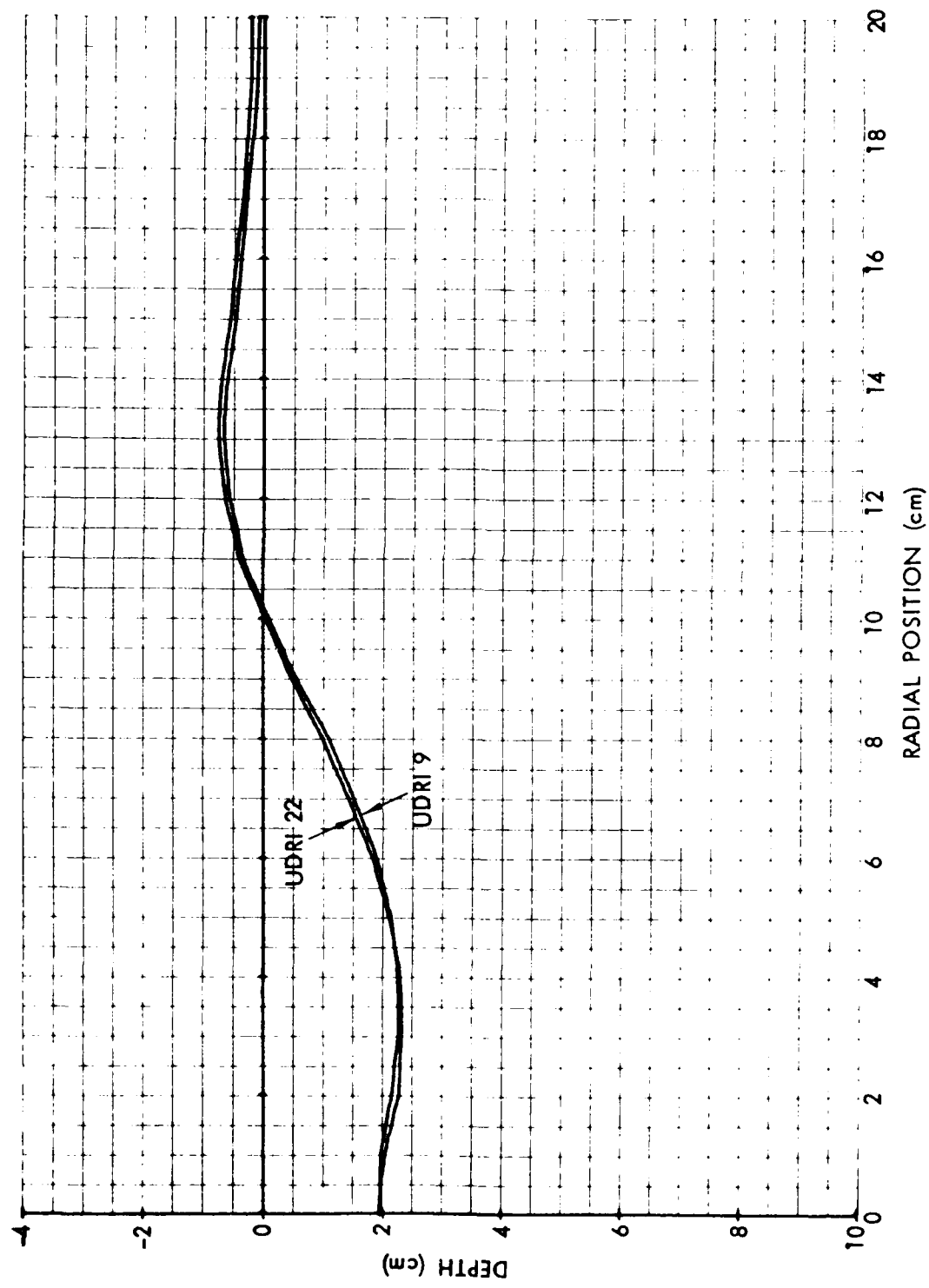


Figure B1. Comparison of crater 9 with crater 22.

Table B2. Ottawa sand 1G control shot, 0.4 gram PETN.

SHOT NUMBER	UDRI-146
DATE	24 Aug. 73
PURPOSE	AFWL-TR-74-182
CHARGE DESCRIPTION	CICS-5 (103)
CHARGE WT. (gm)	.125 AgN <sub>3</sub> /.3609 PETN
CHARGE RADIUS (cm)	.390
CHARGE CONFIGURATION	half buried sphere
TEST BED MATERIAL	Ottawa Flintshot
TEST BED DENSITY (gm/cc)	1.796
MOISTURE CONTENT	nom. 0
TEST BED GEOMETRY	homogeneous
CRATER DIAMETER (cm)	17.78
CRATER RADIUS (cm)	8.89
MAX. CRATER DEPTH (cm)	2.02
CRATER ASPECT RATIO (r/h)	4.40
CRATER VOLUME (cc)	284.
LIP DIAMETER (cm)	22.0
LIP HEIGHT (cm)	.581
LIP VOLUME (cm <sup>3</sup> )	216.
MEAN CRATER PROFILE	AVERAGE OF 8 RADIALS
<u>RANGE (cm)</u>	<u>DEPTH (cm)</u>
0.0	1.513
1.0	1.800
2.0	1.969
3.0	2.019
4.0	1.906
5.0	1.669
6.0	1.319
7.0	0.888
8.0	0.406
9.0	-0.050
10.0	-0.394
11.0	-0.581
12.0	-0.544
13.0	-0.394
14.0	-0.231
15.0	-0.206
16.0	-0.119
17.0	-0.069
18.0	-0.050
19.0	-0.025
20.0	-0.019
21.0	-0.013
22.0	0.000

Table B2 (cont.) Ottawa sand 1G control shots, 0.4 gram PETN.

SHOT NUMBER	UDRI-117	UDRI-120
DATE	11 June 73	15 June 73
PURPOSE	AFWL-TR-74-182	AFWL-TR-74-182
CHARGE DESCRIPTION	CICS-5 (14)	CICS-5 (21)
CHARGE WT. (gm)	.125 AgN <sub>3</sub> /.3602 PETN	.125 AgN <sub>3</sub> /.3602 PETN
CHARGE RADIUS (cm)	.390	.390
CHARGE CONFIGURATION	half buried sphere	half buried sphere
TEST BED MATERIAL	Ottawa Flintshot	Ottawa Flintshot
TEST BED DENSITY (gm/cc)	1.802	1.796
MOISTURE CONTENT	nom. 0%	nom. 0%
TEST BED GEOMETRY	homogeneous	homogeneous
CRATER DIAMETER (cm)	17.5	17.76
CRATER RADIUS (cm)	8.76	8.88
MAX. CRATER DEPTH (cm)	2.06	2.13
CRATER ASPECT RATIO (r/h)	4.25	4.17
CRATER VOLUME (cc)	274.	292.
LIP DIAMETER (cm)	22.0	22.0
LIP HEIGHT (cm)	.569	.581
LIP VOLUME (cm <sup>3</sup> )	217.0	265.

MEAN CRATER PROFILE

AVERAGE OF 8 RADIALS FOR EACH CRATER

<u>RANGE (cm)</u>	<u>DEPTH (cm)</u>	<u>DEPTH (cm)</u>
0.0	1.813	1.925
1.0	1.938	1.994
2.0	2.056	2.125
3.0	2.038	2.069
4.0	1.863	1.950
5.0	1.625	1.706
6.0	1.250	1.313
7.0	0.825	0.919
8.0	0.331	0.406
9.0	-0.106	-0.056
10.0	-0.431	-0.425
11.0	-0.569	-0.581
12.0	-0.513	-0.556
13.0	-0.363	-0.431
14.0	-0.263	-0.288
15.0	-0.175	-0.200
16.0	-0.125	-0.156
17.0	-0.094	-0.119
18.0	-0.044	-0.081
19.0	-0.044	-0.069
20.0	-0.031	-0.031
21.0	-0.019	-0.031
22.0	0.000	-0.031
23.0	--	-0.031
24.0	--	-0.038

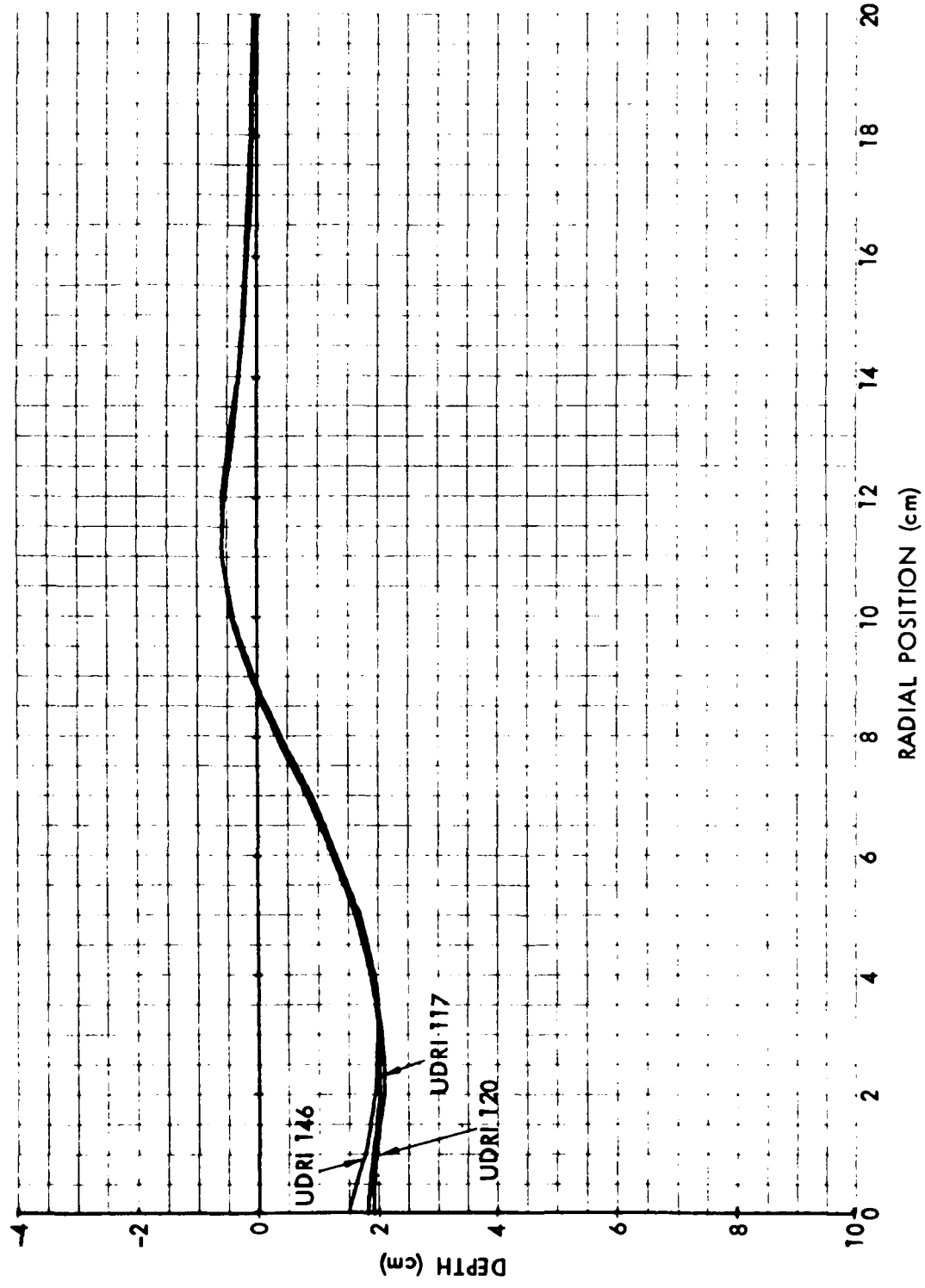


Figure B2. Comparison of craters 117, 120 and 146.

Table B3. Ottawa sand 1G control shots, 1.265 grams PETN.

SHOT NUMBER	UDRI-642	UDRI-644
DATE	19 Oct. 77	24 Oct. 77
PURPOSE	1G Control	1G Control
CHARGE DESCRIPTION	CICS-1.265 (B-5)	CICS-1.265 (B-4)
CHARGE WT. (gm)	.125 AgN <sub>3</sub> /1.2245 PETN	.125 AgN <sub>3</sub> /1.2326 PETN
CHARGE RADIUS (cm)	.565	.565
CHARGE CONFIGURATION	half buried sphere	half buried sphere
TEST BED MATERIAL	Ottawa Flintshot	Ottawa Flintshot
TEST BED DENSITY (gm/cc)	1.802	1.802
MOISTURE CONTENT	nom. 0%	nom. 0%
TEST BED GEOMETRY	homogeneous	homogeneous
CRATER DIAMETER (cm)	23.6	24.0
CRATER RADIUS (cm)	11.8	12.0
MAX. CRATER DEPTH (cm)	2.50	2.66
CRATER ASPECT RATIO (r/h)	4.72	4.51
CRATER VOLUME (cc)	640.	706.
LIP DIAMETER (cm)	30.0	30.0
LIP HEIGHT (cm)	.838	.863
LIP VOLUME (cm <sup>3</sup> )	798.	814.
MEAN CRATER PROFILE	AVERAGE OF 8 RADIALS FOR EACH CRATER	
RANGE (cm)	DEPTH (cm)	DEPTH (cm)
0.0	1.600	1.650
1.0	1.681	1.894
2.0	2.156	2.319
3.0	2.419	2.569
4.0	2.500	2.656
5.0	2.488	2.613
6.0	2.319	2.463
7.0	2.094	2.206
8.0	1.731	1.869
9.0	1.313	1.481
10.0	0.838	1.019
11.0	0.338	0.488
12.0	-0.106	0.019
13.0	-0.475	-0.388
14.0	-0.719	-0.681
15.0	-0.838	-0.863
16.0	-0.763	-0.844
17.0	-0.644	-0.719
18.0	-0.531	-0.581
19.0	-0.431	-0.481
20.0	-0.363	-0.381
21.0	-0.306	-0.300
22.0	-0.263	-0.256
23.0	-0.188	-0.219
24.0	-0.156	-0.169

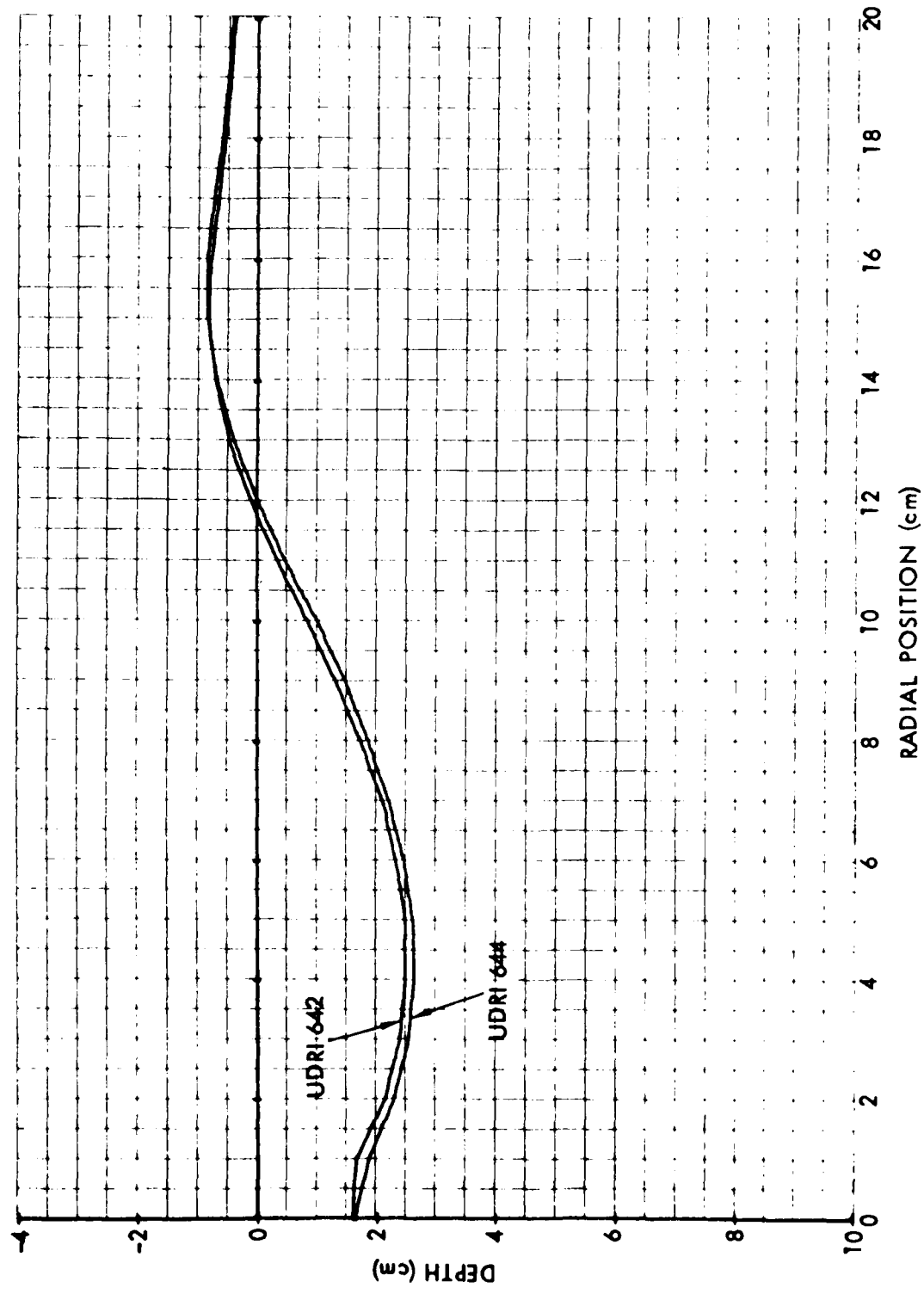


Figure B3. Comparison of crater 642 with crater 644.

Table B4. Ottawa sand 1G control shots, 4.0 grams PETN.

SHOT NUMBER	UDRI-643	UDRI-645
DATE	20 Oct. 77	25 Oct. 77
PURPOSE	1G Control	1G Control
CHARGE DESCRIPTION	CICS-4 (BL-6)	CICS-4 (BL-7)
CHARGE WT. (gm)	.125 AgN <sub>3</sub> /3.9348 PETN	.125 AgN <sub>3</sub> /3.9493 PETN
CHARGE RADIUS (cm)	.826	.826
CHARGE CONFIGURATION	half buried sphere	half buried sphere
TEST BED MATERIAL	Ottawa Flintshot	Ottawa Flintshot
TEST BED DENSITY (gm/cc)	1.802	1.802
MOISTURE CONTENT	nom. 0%	nom. 0%
TEST BED GEOMETRY	homogeneous	homogeneous
CRATER DIAMETER (cm)	32.6	32.8
CRATER RADIUS (cm)	16.3	16.4
MAX. CRATER DEPTH (cm)	3.39	3.54
CRATER ASPECT RATIO (r/h)	4.81	4.63
CRATER VOLUME (cc)	1677.	1751.
LIP DIAMETER (cm)	42.0	42.0
LIP HEIGHT (cm)	1.13	1.17
LIP VOLUME (cm <sup>3</sup> )	1925.	2062.

MEAN CRATER PROFILE

AVERAGE OF 8 RADIALS FOR EACH CRATER

RANGE (cm)	DEPTH (cm)	DEPTH (cm)
0.0	2.400	2.300
1.0	2.338	2.388
2.0	2.638	2.869
3.0	2.931	3.194
4.0	3.156	3.406
5.0	3.331	3.513
6.0	3.388	3.538
7.0	3.356	3.488
8.0	3.244	3.294
9.0	3.031	3.069
10.0	2.750	2.794
11.0	2.394	2.475
12.0	2.019	2.125
13.0	1.556	1.656
14.0	1.081	1.163
15.0	0.600	0.638
16.0	0.119	0.163
17.0	-0.281	-0.256
18.0	-0.638	-0.625
19.0	-0.919	-0.925
20.0	-1.081	-1.106
21.0	-1.125	-1.169
22.0	-1.050	-1.119
23.0	-0.950	-1.000
24.0	-0.800	-0.856

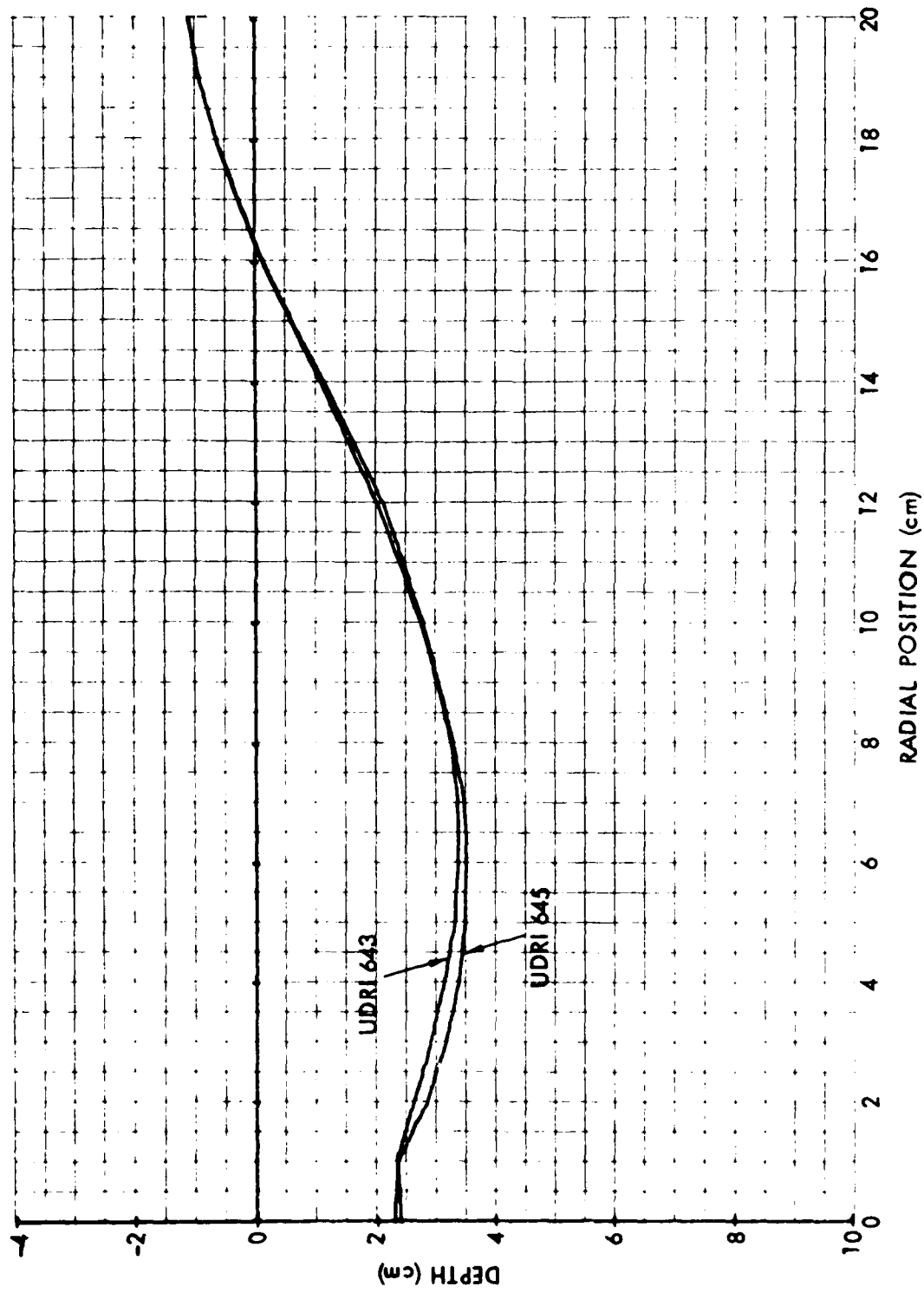


Figure B4. Comparison of crater 643 with crater 645.

Table B5. KAFB alluvium 1G control shots, 1.7 grams lead azide.

SHOT NUMBER	UDRI-646	UDRI-647
DATE	11 Nov. 77	14 Nov. 77
PURPOSE	1G Control	1G Control
CHARGE DESCRIPTION	CILAS-13 (814)	CILAS-13 (815)
CHARGE WT. (gm)	1.7004 PbN <sub>6</sub>	1.7099 PbN <sub>6</sub>
CHARGE RADIUS (cm)	.508	.508
CHARGE CONFIGURATION	half buried sphere	half buried sphere
TEST BED MATERIAL	KAFB Alluvium	KAFB Alluvium
TEST BED DENSITY (gm/cc)	1.622	1.581
MOISTURE CONTENT	nom. 4.5%	nom. 4.5%
TEST BED GEOMETRY	homogeneous	homogeneous
CRATER DIAMETER (cm)	12.94	13.8
CRATER RADIUS (cm)	6.47	6.90
MAX. CRATER DEPTH (cm)	1.85	1.95
CRATER ASPECT RATIO (r/h)	3.50	3.54
CRATER VOLUME (cc)	58.7	72.4
LIP DIAMETER (cm)	23.0	20.0
LIP HEIGHT (cm)	.163	.131
LIP VOLUME (cm <sup>3</sup> )	104.	61.7
MEAN CRATER PROFILE	AVERAGE OF 8 RADIALS FOR EACH CRATER	
<u>RANGE (cm)</u>	<u>DEPTH (cm)</u>	<u>DEPTH (cm)</u>
0.0	1.850	1.950
1.0	1.588	1.713
2.0	0.744	0.988
3.0	0.619	0.806
4.0	0.613	0.631
5.0	0.269	0.369
6.0	0.006	0.081
7.0	-0.044	0.006
8.0	-0.031	-0.031
9.0	-0.088	-0.125
10.0	-0.156	-0.131
11.0	-0.163	-0.119
12.0	-0.163	-0.088
13.0	-0.119	-0.075
14.0	-0.113	-0.063
15.0	-0.081	-0.005
16.0	-0.056	-0.031
17.0	-0.056	-0.025
18.0	-0.044	-0.025
19.0	-0.038	-0.019
20.0	-0.031	-0.013
21.0	-0.019	0.000
22.0	-0.019	0.000
23.0	-0.019	--
24.0	-0.006	--

Table B5 (cont.) KAFB alluvium 1G control shot, 1.7 grams lead azide.

SHOT NUMBER	UDRI-648
DATE	18 Nov. 77
PURPOSE	1G Control
CHARGE DESCRIPTION	CILAS-13 (816)
CHARGE WT. (gm)	1.7004 PbN6
CHARGE RADIUS (cm)	.508
CHARGE CONFIGURATION	half buried sphere
TEST BED MATERIAL	KAFB Alluvium
TEST BED DENSITY (gm/cc)	1.600
MOISTURE CONTENT	nom. 4.5%
TEST BED GEOMETRY	homogeneous
CRATER DIAMETER (cm)	11.68
CRATER RADIUS (cm)	5.84
MAX. CRATER DEPTH (cm)	1.75
CRATER ASPECT RATIO (r/h)	3.34
CRATER VOLUME (cc)	45.0
LIP DIAMETER (cm)	20.0
LIP HEIGHT (cm)	.144
LIP VOLUME (cm <sup>3</sup> )	71.8
MEAN CRATER PROFILE	AVERAGE OF 8 RADIALS
<u>RANGE (cm)</u>	<u>DEPTH (cm)</u>
0.0	1.750
1.0	1.450
2.0	0.713
3.0	0.581
4.0	0.425
5.0	0.113
6.0	-0.075
7.0	-0.006
8.0	-0.044
9.0	-0.081
10.0	-0.144
11.0	-0.144
12.0	-0.119
13.0	-0.113
14.0	-0.113
15.0	-0.075
16.0	-0.038
17.0	-0.025
18.0	-0.013
19.0	0.000
20.0	0.000

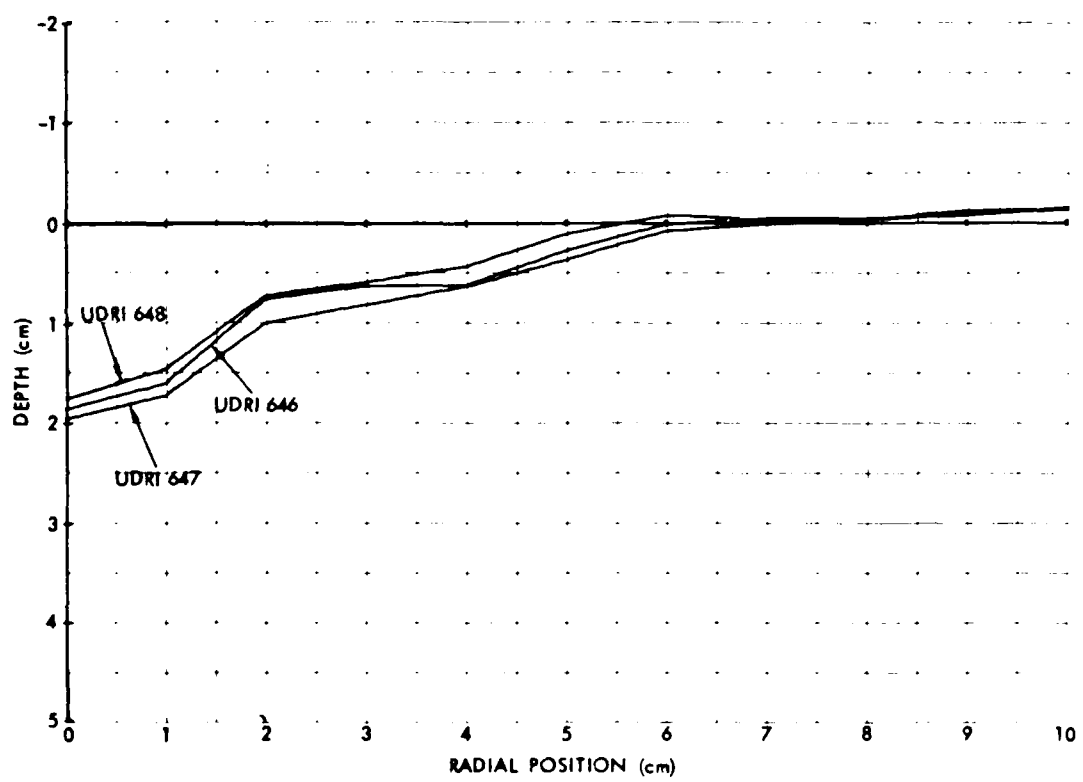


Figure B5. Comparison of craters 646, 647 and 648.

Table B6. KAFB alluvium 1G control shots, 1.265 grams PETN.

SHOT NUMBER	UDRI-649	UDRI-652
DATE	22 Nov. 77	9 Dec. 77
PURPOSE	1G Control	1G Control
CHARGE DESCRIPTION	CICS-1.265 (B-6)	CICS-1.265 (B-7)
CHARGE WT. (gm)	.125 AgN <sub>3</sub> /1.2241 PETN	.125 AgN <sub>3</sub> /1.2259 PETN
CHARGE RADIUS (cm)	.565	.565
CHARGE CONFIGURATION	half buried sphere	half buried sphere
TEST BED MATERIAL	KAFB Alluvium	KAFB Alluvium
TEST BED DENSITY (gm/cc)	1.571	1.587
MOISTURE CONTENT	nom. 4.5%	nom. 4.5%
TEST BED GEOMETRY	homogeneous	homogeneous
CRATER DIAMETER (cm)	13.75	12.88
CRATER RADIUS (cm)	6.88	6.44
MAX. CRATER DEPTH (cm)	2.40	2.00
CRATER ASPECT RATIO (r/h)	2.87	3.22
CRATER VOLUME (cc)	103.	66.6
LIP DIAMETER (cm)	16.0	14.0
LIP HEIGHT (cm)	.131	.075
LIP VOLUME (cm <sup>3</sup> )	65.8	60.8

MEAN CRATER PROFILE

AVERAGE OF 8 RADIALS FOR EACH CRATER

<u>RANGE (cm)</u>	<u>DEPTH (cm)</u>	<u>DEPTH (cm)</u>
0.0	2.400	2.000
1.0	2.244	1.738
2.0	1.513	0.844
3.0	0.956	0.688
4.0	0.838	0.606
5.0	0.613	0.369
6.0	0.250	0.081
7.0	-0.044	-0.075
8.0	-0.131	-0.050
9.0	-0.038	-0.013
10.0	0.000	0.013
11.0	-0.069	0.019
12.0	-0.113	0.006
13.0	-0.056	0.000
14.0	-0.050	-0.025
15.0	-0.069	-0.050
16.0	-0.019	-0.044
17.0	-0.019	-0.031
18.0	-0.038	-0.056
19.0	-0.025	-0.056
20.0	-0.025	-0.044
21.0	-0.025	-0.056
22.0	-0.019	-0.025
23.0	-0.013	-0.025
24.0	-0.019	-0.025

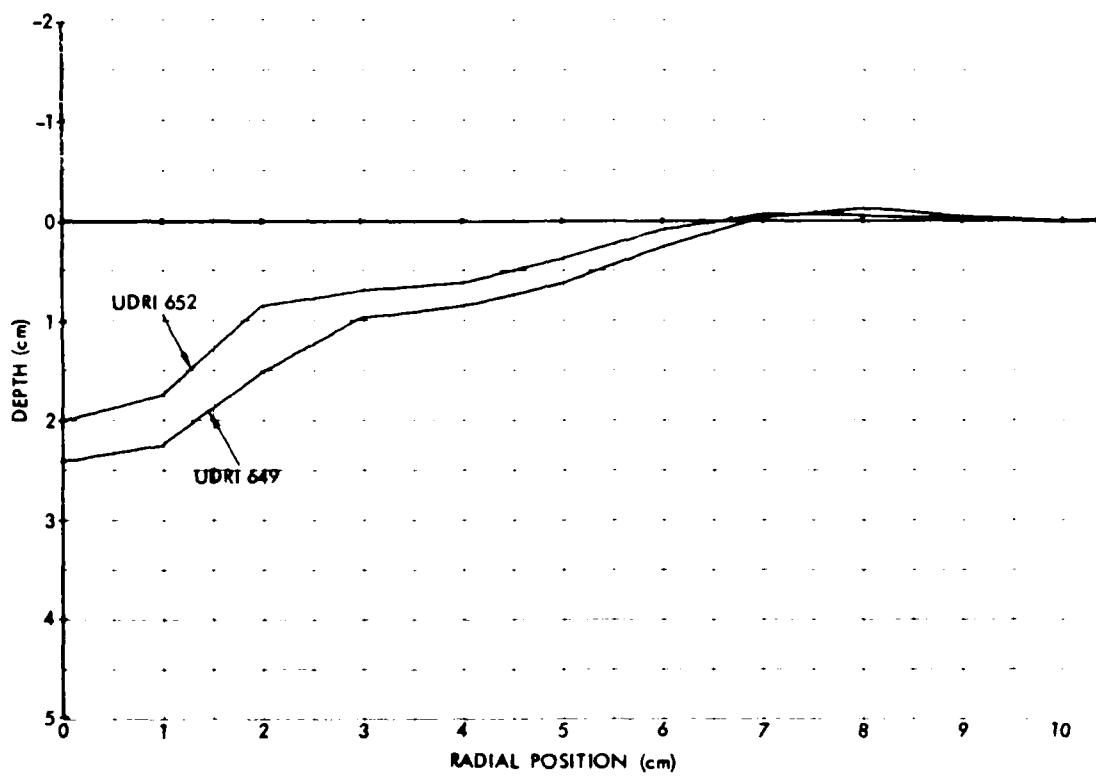


Figure B6. Comparison of crater 649 with crater 652.

Table B7. KAFB alluvium 1G control shots, 4 grams PETN

SHOT NUMBER	UDRI-650	UDRI-651
DATE	30 Nov. 77	5 Dec. 77
PURPOSE	1G Control	1G Control
CHARGE DESCRIPTION	CICS-4 (BL-8)	CICS-4 (BL-9)
CHARGE WT. (gm)	.125 AgN <sub>3</sub> /3.9509 PETN	.125 AgN <sub>3</sub> /3.9620 PETN
CHARGE RADIUS (cm)	.826	.826
CHARGE CONFIGURATION	half buried sphere	half buried sphere
TEST BED MATERIAL	KAFB Alluvium	KAFB Alluvium
TEST BED DENSITY (gm/cc)	1.555	1.584
MOISTURE CONTENT	nom. 4%	nom. 4%
TEST BED GEOMETRY	homogeneous	homogeneous
CRATER DIAMETER (cm)	16.56	17.0
CRATER RADIUS (cm)	8.28	8.52
MAX. CRATER DEPTH (cm)	2.86	2.80
CRATER ASPECT RATIO (r/h)	2.90	3.04
CRATER VOLUME (cc)	196.	175.
LIP DIAMETER (cm)	20.0	20.0
LIP HEIGHT (cm)	.30	.294
LIP VOLUME (cm <sup>3</sup> )	354.	403.

MEAN CRATER PROFILE

AVERAGE OF 8 RADIALS FOR EACH CRATER

RANGE (cm)	DEPTH (cm)	DEPTH (cm)
0.0	2.850	2.800
1.0	2.863	2.663
2.0	2.425	2.156
3.0	1.719	1.400
4.0	1.213	1.038
5.0	1.038	0.844
6.0	0.763	0.650
7.0	0.388	0.413
8.0	0.075	0.156
9.0	-0.200	-0.131
10.0	-0.300	-0.294
11.0	-0.250	-0.288
12.0	-0.163	-0.219
13.0	-0.119	-0.125
14.0	-0.094	-0.100
15.0	-0.056	-0.100
16.0	-0.094	-0.100
17.0	-0.100	-0.119
18.0	-0.088	-0.125
19.0	-0.081	-0.106
20.0	-0.113	-0.088
21.0	-0.075	-0.075
22.0	-0.075	-0.075
23.0	-0.081	-0.094
24.0	-0.063	-0.075

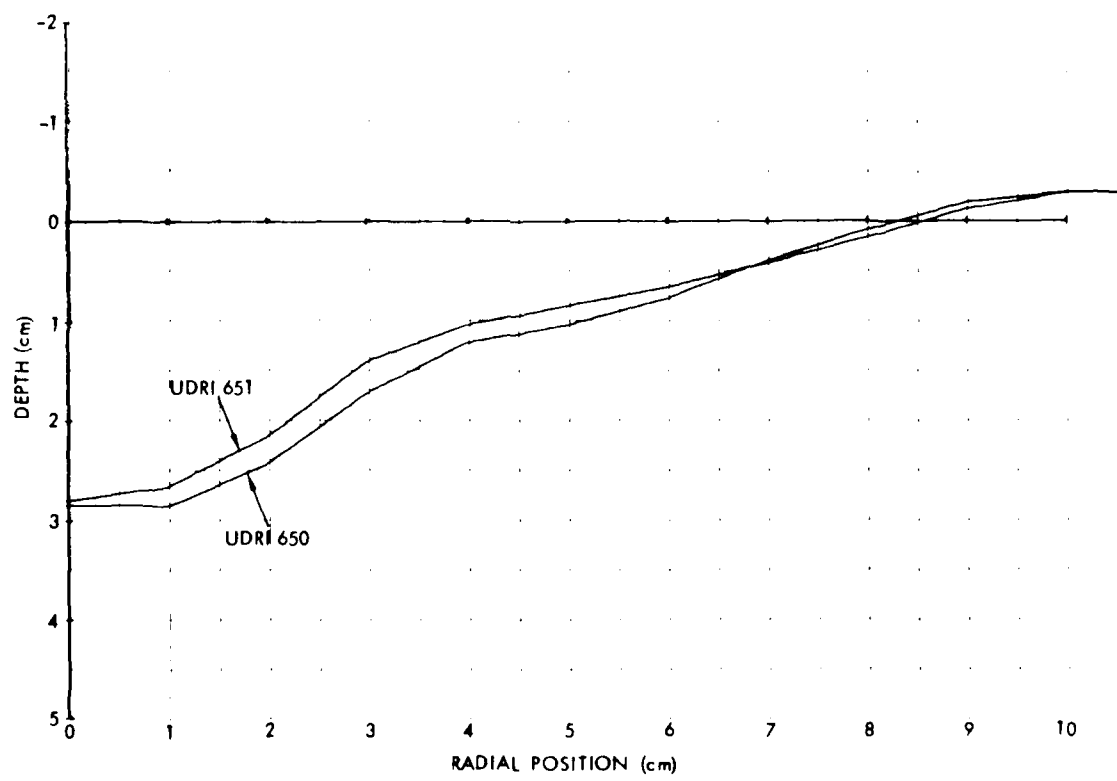


Figure B7. Comparison of crater 650 with crater 651.

APPENDIX C  
MATERIAL PROPERTIES OF TEST SOILS

REPORT OF  
LABORATORY TESTS  
ON SOIL MATERIALS  
FOR  
BOEING AEROSPACE COMPANY

DECEMBER 1977

SHANNON & WILSON, INC.  
GEOTECHNICAL CONSULTANTS  
1105 NORTH 38TH STREET  
SEATTLE, WASHINGTON 98103

PRECEDING PAGE BLANK-NOT FILMED

## TABLE OF CONTENTS

	<u>Page</u>
I. PURPOSE AND SCOPE	139
II. TEST PROCEDURES	139
III. TEST RESULTS	140
A. Presentation	140
B. Interpretation	140

## LIST OF TABLES AND FIGURES

Table C1	Summary of Materials and Test Specifications	141
Figure C1	Modeling Clay Test Results	142
Figure C2	Sawing Sand Test Results	143
Figure C3	Flintshot Sand Test Results	144
Figure C4	Banding Sand Test Results	145
Figure C5	KAFB Alluvium #2 Test Results	146
Figure C6	KAFB Alluvium #4 Test Results	147

REPORT OF  
LABORATORY TESTS  
PERFORMED ON  
SOIL MATERIALS

I. PURPOSE AND SCOPE

This report presents the results of a series of unconsolidated-undrained (UU), triaxial compression tests performed on each of six soil materials provided by Boeing Aerospace Company. Three UU tests were performed on each material type to determine the shear strength parameters of the material. The samples were designated as follows: KAFB Alluvium #2, Banding Sand, Sawing Sand, KAFB Alluvium #4, Molding Clay and Flintshot Sand.

II. TEST PROCEDURES

Three test specimens were prepared from each of the six material types. Test specimens of the five sand and alluvium material types were prepared by compacting the material to a density specified by Boeing (see Table C1 for a summary of specified densities). Compaction to the specified density was achieved by vibrating a known weight of material into a cylindrical mold of known volume. The mold was lined with a thin rubber membrane that remained in place around the compacted test specimen throughout the test in order to protect the material from the water used as a confining medium during the test. Test specimens from the "modeling clay" material type were prepared by trimming the bulk sample into three cylindrical specimens and then encasing each specimen in a thin rubber membrane to protect them from the confining medium.

After each test specimen was prepared, it was mounted in a triaxial test chamber and subjected to a specified triaxial confining pressure, then it was immediately sheared under strain-controlled conditions, while maintaining a constant confining pressure and without allowing drainage. For each material type, triaxial confining pressures of 100, 200 and 400 psi were used on the first, second and third test specimens, respectively, as specified. Water was used as the confining medium for all tests.

Simultaneous readings of load and deformation were obtained at regular time intervals throughout the shearing period. Deviator stress and axial strain values were then computed from these readings.

### III. TEST RESULTS

#### A. Presentation

The results of each of the six series of UU tests are presented in Figures C1 thru C6. Included in each figure are plots of deviator stresses versus axial strains, Mohr circles, pertinent specimen dimensions and test parameters for each of the three tests in the series. In addition, sketches of each specimen's failure mode, failure criteria, and sample classification are included.

#### B. Interpretation

The results of these triaxial compression tests may be used to estimate the parameters of cohesion,  $c$ , and angle of internal friction,  $\phi$ , in the Mohr-Coulomb equation for shear strength under unconsolidated, undrained conditions. This equation relates shear strength to triaxial confining pressure by:

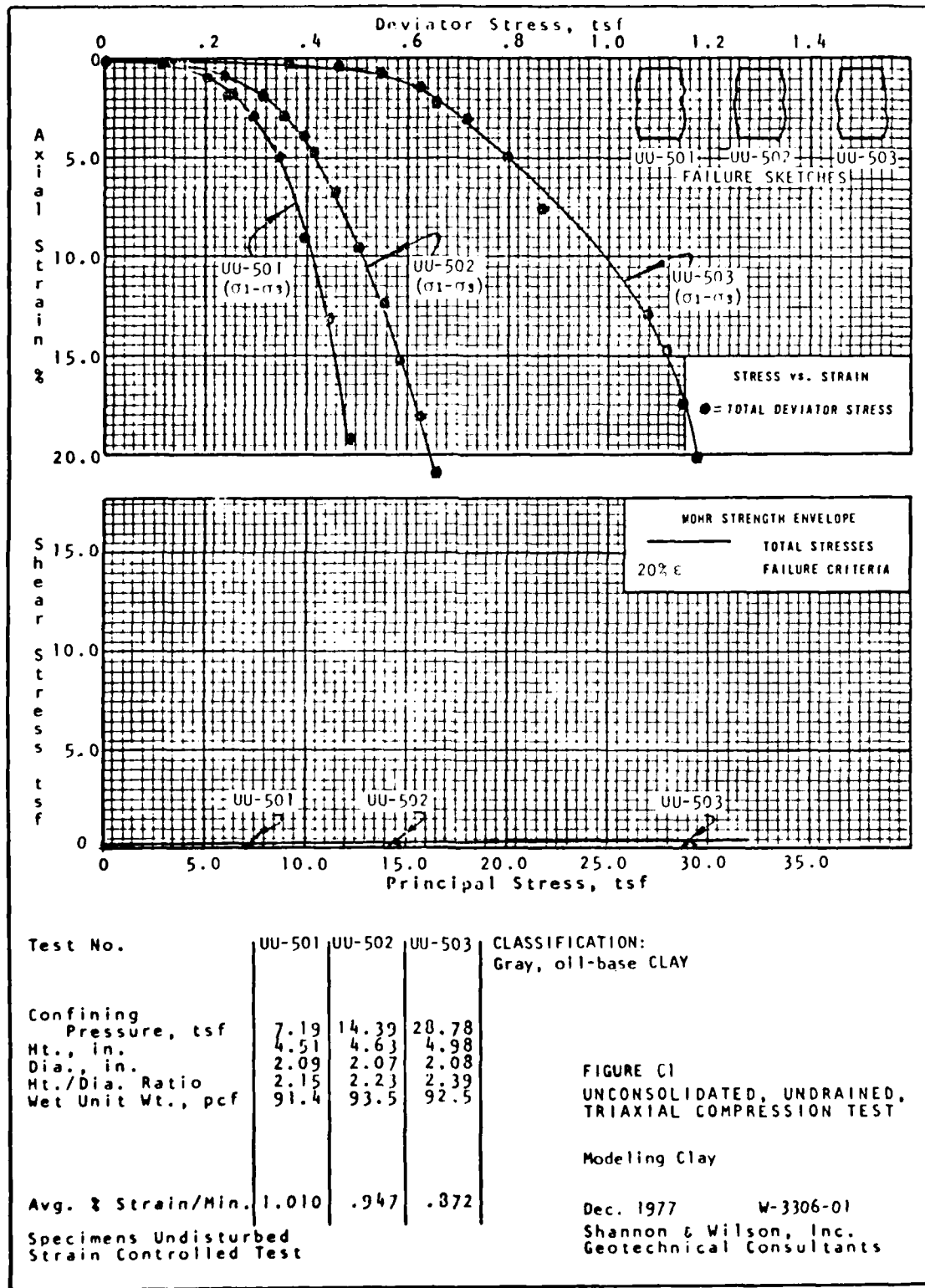
$$\tau = c + N \tan \phi$$

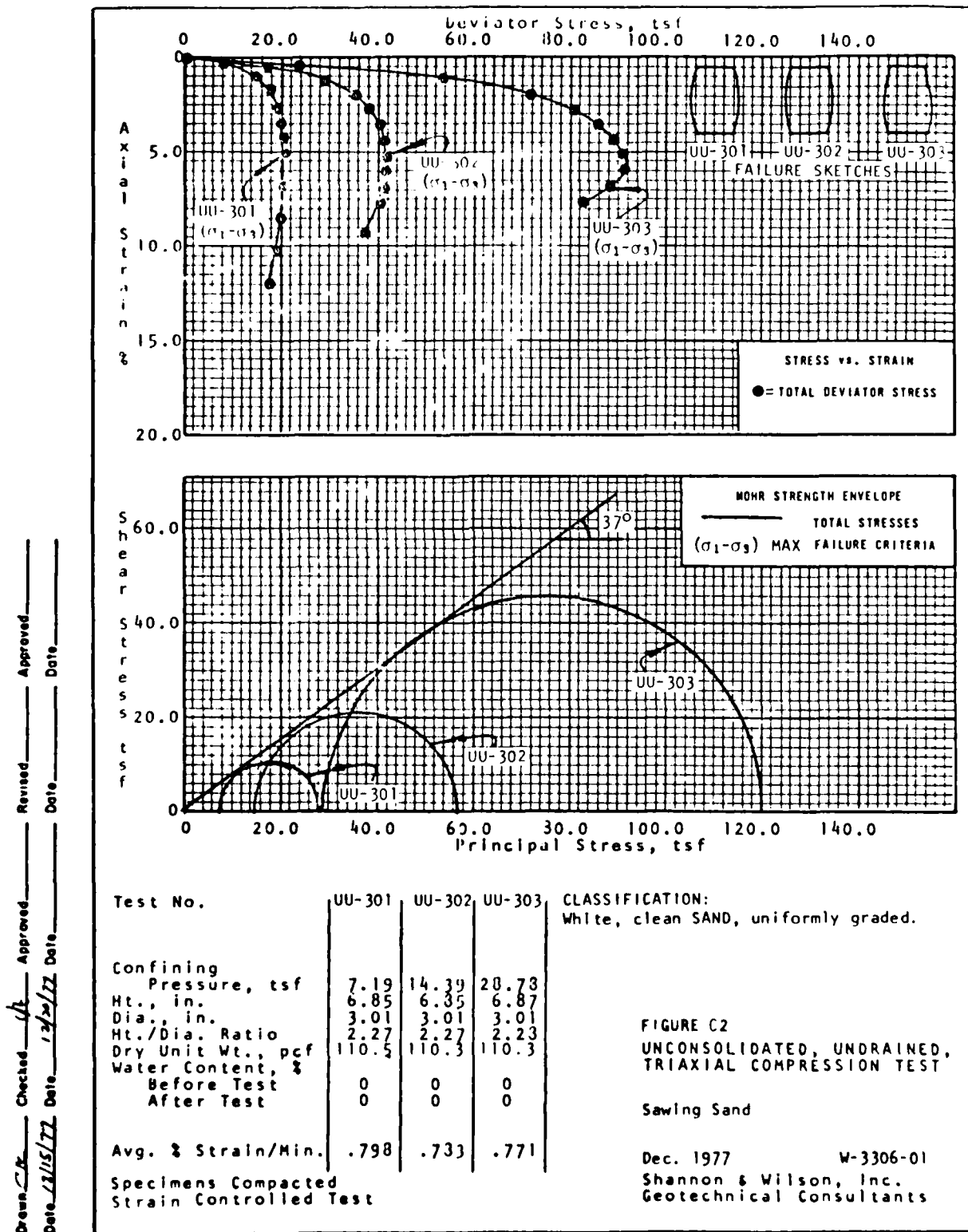
where:  $\tau$  = shear strength  
and  $N$  = principal stress

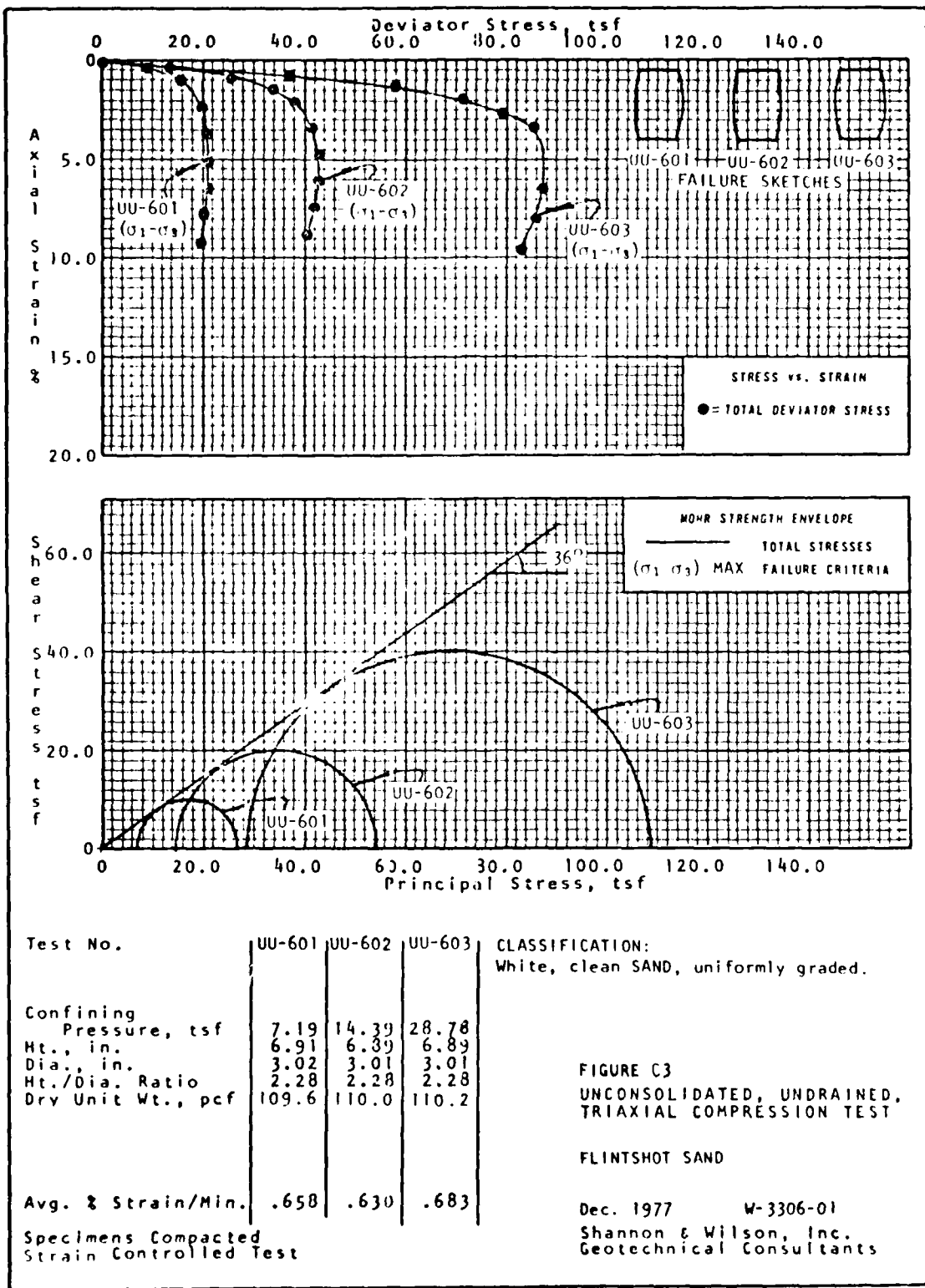
The parameters,  $c$  and  $\phi$ , are obtained from the line, drawn tangent to the three Mohr circles of a test series, which represents the Mohr-Coulomb equation. The Mohr circles are drawn with centers at  $\sigma_3 + \frac{(\sigma_1 - \sigma_3)}{2}$  on the principal stress axis and with radius  $\frac{(\sigma_1 - \sigma_3)}{2}$ ; where  $\sigma_3$  is the triaxial confining pressure and  $(\sigma_1 - \sigma_3)$  is the deviator stress. The values of deviator stress used to construct the Mohr circles are obtained from the plots of deviator stress versus axial strain based on the failure criteria used for the test series.

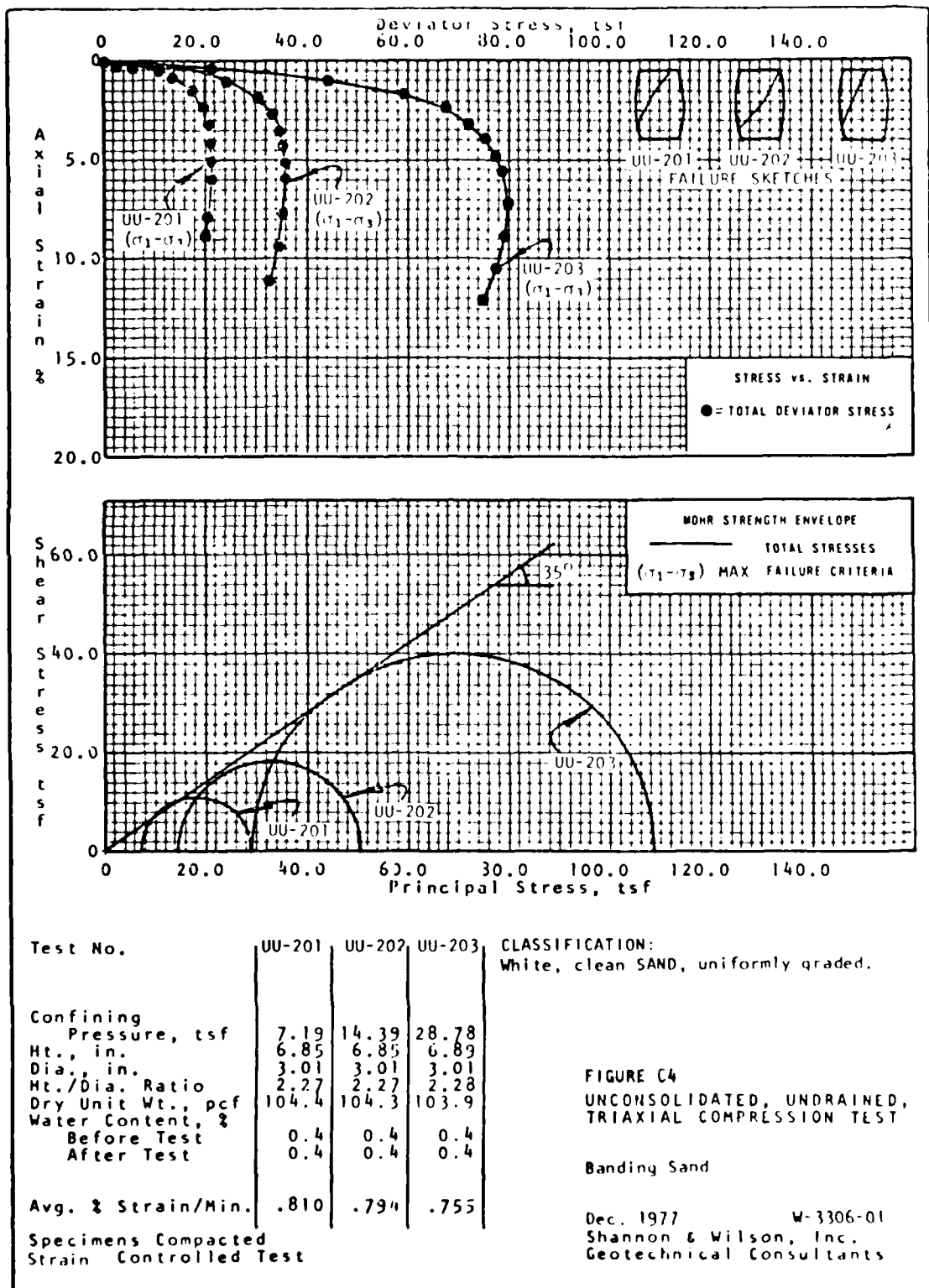
TABLE C1  
 SUMMARY OF  
 MATERIALS AND  
 TEST SPECIFICATIONS

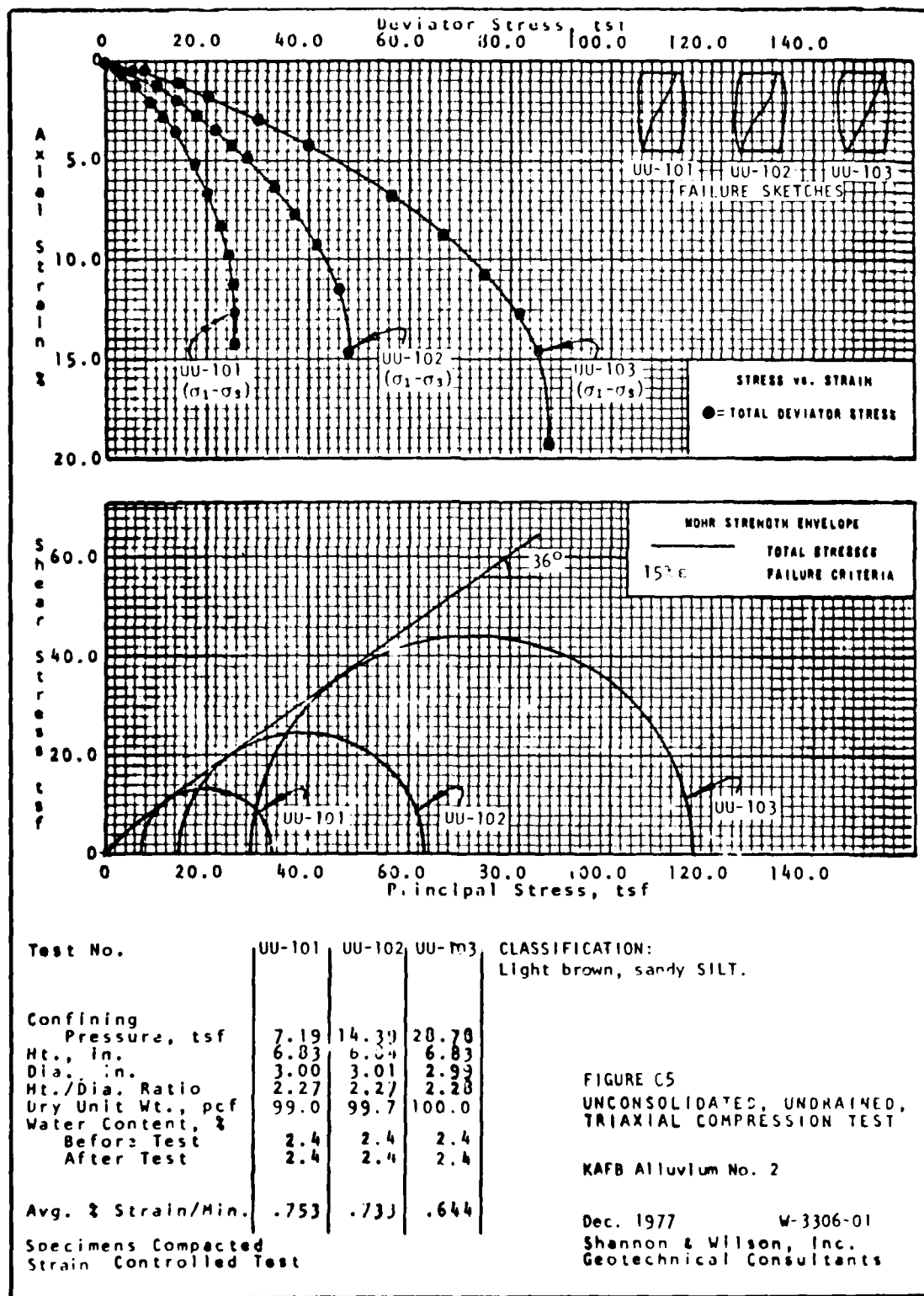
<u>SAMPLE</u>	<u>SPECIFIED DENSITY</u> gms/cc	<u>SPECIFIED DENSITY</u> lbs/ft <sup>3</sup>	<u>SPECIFIED CONFINING PRESSURE</u> psi	<u>LABORATORY TEST NUMBER</u>
Modeling Clay	—	—	100	UU-501
Modeling Clay	—	—	200	UU-502
Modeling Clay	—	—	400	UU-503
Sawing Sand	1.78	110.1	100	UU-301
Sawing Sand	1.78	110.1	200	UU-302
Sawing Sand	1.78	110.1	400	UU-303
Flintshot Sand	1.78	110.1	100	UU-601
Flintshot Sand	1.78	110.1	200	UU-602
Flintshot Sand	1.78	110.1	400	UU-603
Banding Sand	1.68	104.8	100	UU-201
Banding Sand	1.68	104.8	200	UU-202
Banding Sand	1.68	104.8	400	UU-203
KAFB Alluvium #2	1.61	100.5	100	UU-101
KAFB Alluvium #2	1.61	100.5	200	UU-102
KAFB Alluvium #2	1.61	100.5	400	UU-103
KAFB Alluvium #4	1.61	100.5	100	UU-401
KAFB Alluvium #4	1.61	100.5	200	UU-402
KAFB Alluvium #4	1.61	100.5	400	UU-403



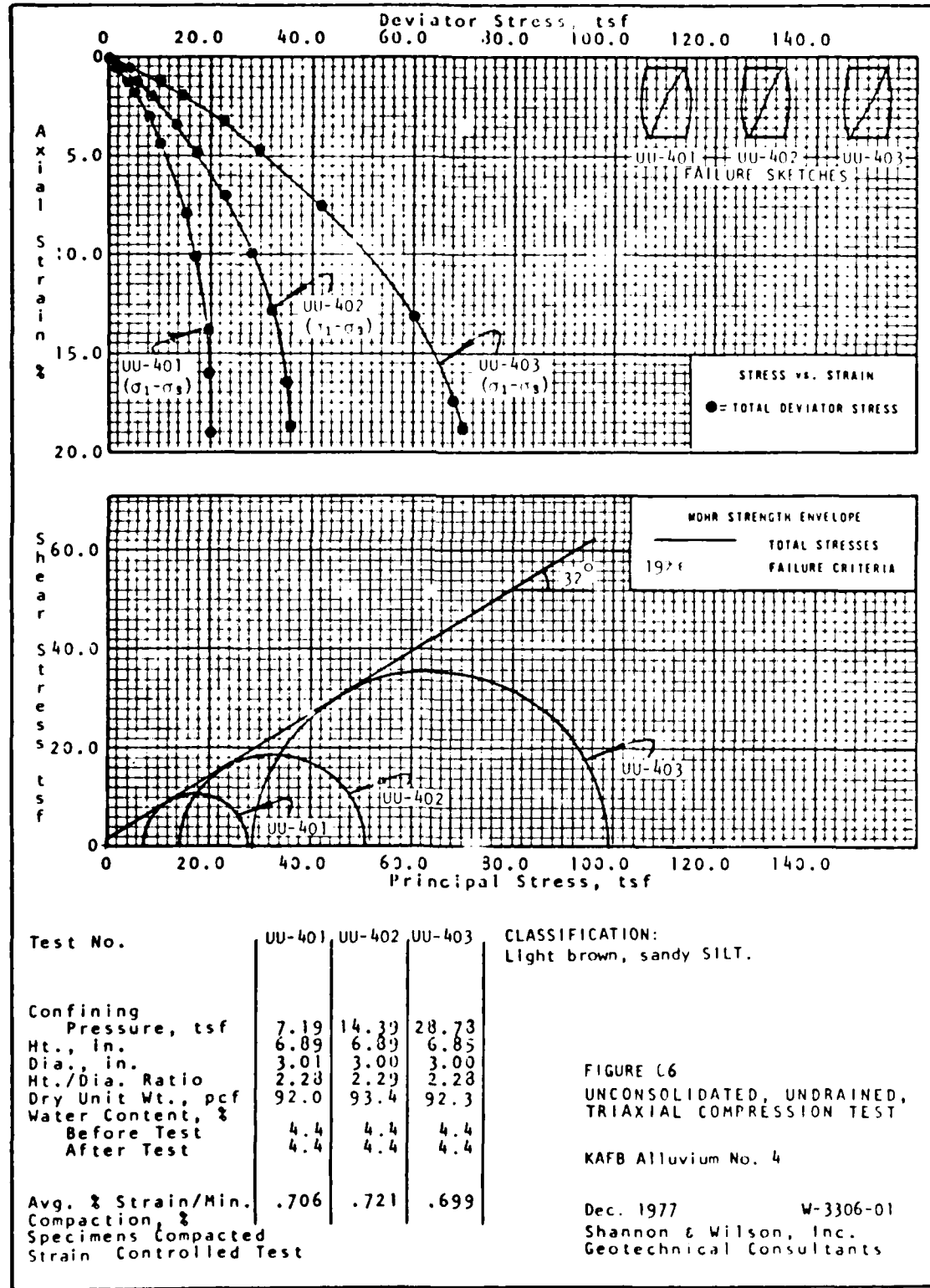








Drawn \_\_\_\_\_ Approved \_\_\_\_\_  
 Checked \_\_\_\_\_ Date 12/20/77 Date \_\_\_\_\_



## APPENDIX D STEREO-CAMERA DYNAMIC PHOTOGRAMMETRY

Analytical photogrammetry can be applied to obtain spatial measurements of explosive crater formation at the time of formation while under large centripetal acceleration in an operating centrifuge. Close-range photogrammetry techniques have been developed for small craters in granular soils using nonmetric cameras. The surface area and the volume of a calibrated object space control frame photographed under static 1-G conditions have been determined. In addition, a contour map was prepared for a typical crater also photographed under static conditions. These show a high degree of accuracy. In preparation for dynamic tests, cameras have been made to operate under the high centripetal accelerations of the rotor hub during centrifuge operation. It remains to be shown what accuracy degradation, if any, results from these centrifugal loads acting on the camera system.

### DESIGN CRITERIA

The conventional profilometer method of post-test measurement can be employed only for stable craters. For fluid craters the topological mapping must be obtained dynamically under high centripetal accelerations. It was the purpose of this study to develop a relatively rapid and accurate method for obtaining such data through the application of photogrammetric techniques.

Due to the fact that clearance volume within the arm of the centrifuge is limited to a length of available 140 cm with a 38-cm width and a 15-cm depth, the maximum distance between the camera film plane and the specimen is 100 to 140 cm depending upon the size of the test sample. The maximum base of the camera station is 25 cm and the height of the cameras can not exceed 15 cm. Since the photographs are to be taken of specimens undergoing centripetal accelerations up to 600 G, the vibration of the camera system must also be taken into consideration in order to obtain quality images.

### PHOTOGRAMMETRIC SYSTEMS

Since there are no terrestrial cameras with fixed base that meet these criteria, two motor-driven Nikon F2 35-mm cameras were considered in conjunction

with analytical concepts. A control frame was built around the specimen to provide an image on the photographs which can be measured, allowing the camera positions and orientation relative to the frame to be computed. This allows calibration for measuring three dimensional coordinates of the crater.

The two cameras, each having a focal length of 55 mm, are mounted on a fixed camera base of 21 cm within the arm of the centrifuge as shown in Figures D1 and D2. The fixed control frame with 20 reference points at five different levels machined into the soil-specimen container is shown in Figure D3. The target diameter of the object-space control points was selected using eq. D1.

$$T = \frac{Dm}{f} \quad (D1)$$

where

T = target diameter on control frame

D = distance between camera and specimen

f = focal length

m = diameter of micrometer measuring-dot on comparator

In order to fit the various measuring instruments, two different target diameters, 0.05 cm and 0.10 cm, were drilled into alternating levels of the control frame which produce film image sizes of approximately 25  $\mu$  and 50  $\mu$ , respectively.

The on-board location of the cameras was chosen to avoid the complex optical geometry which would have been necessary with a stationary mount. In addition, the large tangential velocity of the rotor tip would have required a strobe light with a sub-microsecond duration.

The cameras were mounted as close to the rotor axis as the six-inch-diameter hub would allow. The actual location of the cameras produced an average acceleration in excess of 60 G on each camera at the maximum centrifuge speed of 620 rpm. Tests were performed photographing high contrast resolution charts mounted on the rotor tip. The cameras performed satisfactorily with no appreciable loss of resolution up to maximum centrifuge speed. The shutter mechanism worked properly on both cameras throughout the entire speed range.

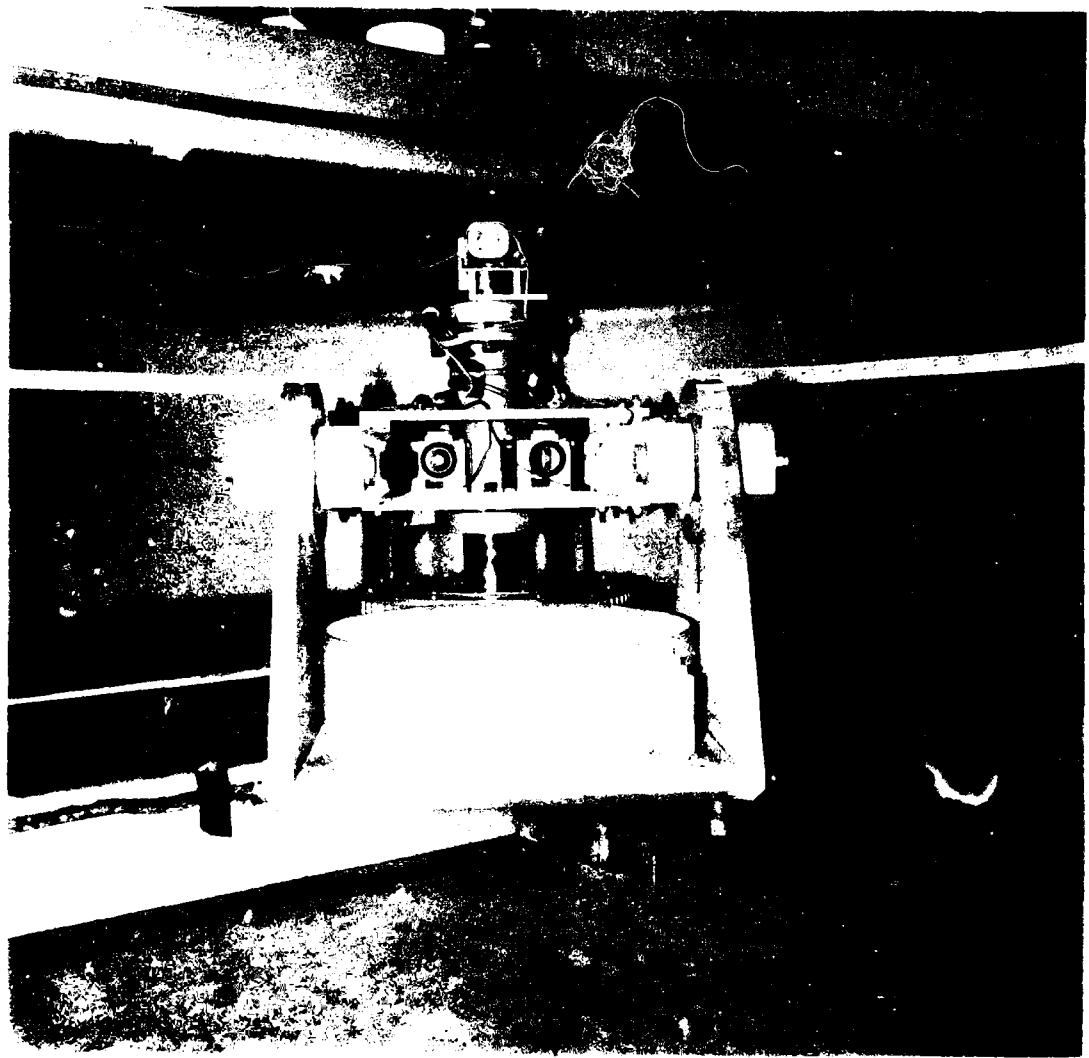


Figure D.1. The centrifuge rotor showing the two cameras in relation to a mounted sample in the rest position.

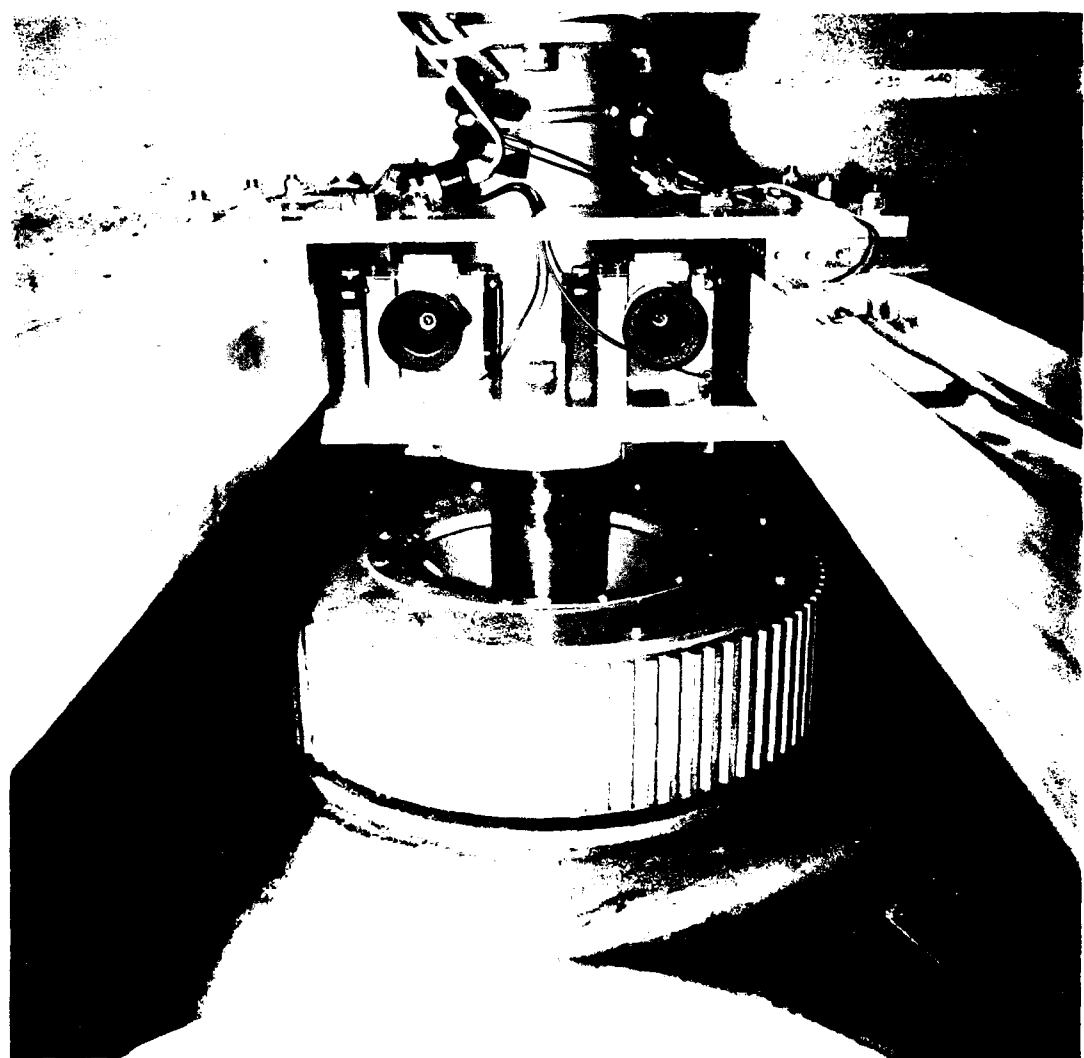


Figure 92. The fixed camera base in the rotor hub of the centrifuge.

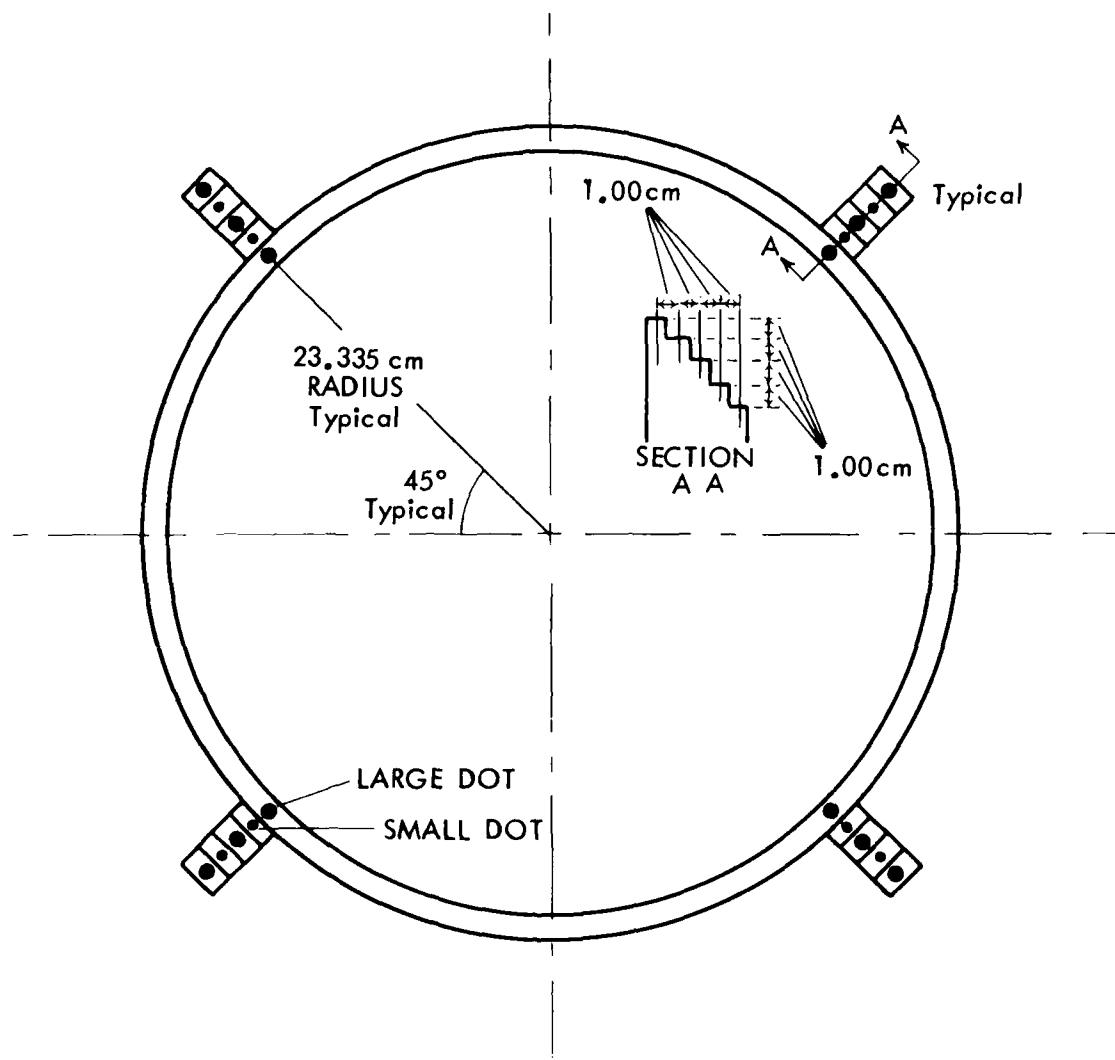


Figure D3. Control frame and control points.

The cameras were operated in the semiautomatic mode using the motors to advance the film. At 600 rpm the motor-drive mechanism of the right-hand camera started to advance the film somewhat erratically. The location at a radius of approximately 19 cm corresponds to 77 G. This can be remedied by mounting the right-hand camera upside down bringing the wind mechanism more inboard. The camera motors were powered through the centrifuge slip rings using a standard laboratory 16-Vdc supply.

In the automatic mode at 5 frames per second, the shutter speed (set at 1/500 of a second) went out of calibration at approximately 300 rpm corresponding to 15 to 20 G acting on the cameras. No further centrifuge tests were performed. A slower shutter speed with an electronic flash may provide satisfactory operation at higher rpm in the automatic framing mode. In general, the operation of the cameras exceeded expectations and it is felt that they will provide satisfactory photographs for the intended dynamic photogrammetry application. Figure D4 shows typical dynamic photos.

#### METHODOLOGY

Analytical photogrammetry is not a new concept, having been thoroughly developed by mathematicians prior to the 1930's. However, the laborious computations inspired development of analogical instruments which make a simple graphic solution. The speed with which present day computers perform computations has revitalized the mathematical analytical methods which permit correction of systematic errors not correctable with the mechanical analogical (D1) system.

Analytical photogrammetry uses data measured stereoscopically using a comparator in a coordinate system with the origin at the principal point based on camera fiducial marks. These data are transformed to photo coordinates using a linear transformation to change the scale and rotation. (D2)

$$x = a_{11} R + a_{12} H + x_0 \quad (D2.1)$$

$$y = a_{11} H - a_{12} R + y_0 \quad (D2.2)$$

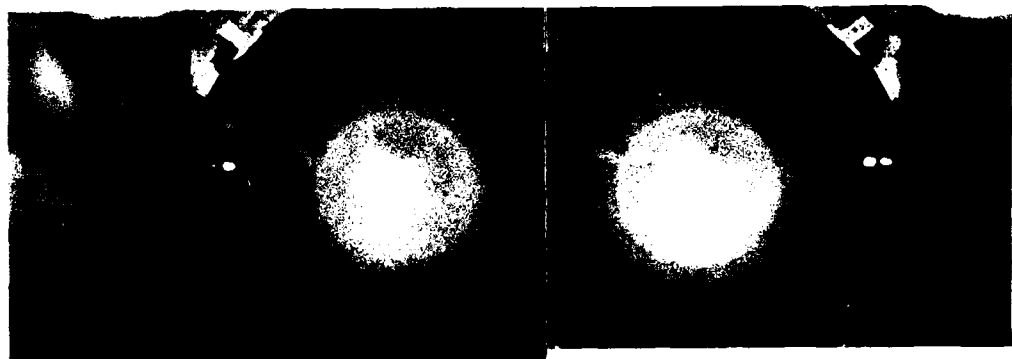


Figure D4. Stereo-photographs of craters under the acceleration of 10G (above) and 100G (below).

The transformed coordinates of a point P in the photo coordinates system are x and y. R and H are the coordinates of point P expressed in the comparator system,  $a_{11}$  and  $a_{12}$  are unknown coefficients of the transformation, and  $x_0$  and  $y_0$  are the unknown translation terms in x and y.

Since the Nikon camera is not equipped with fiducial marks, comparator coordinates of the four corner points were measured and used in eq. D2, with a least-squares method, to determine the transformation coefficients. These were then used on all the points in each photo for transforming to the photo coordinates system. The camera station for each photo was then determined using the coordinates of the object-space control points and their corresponding photo coordinates, using collinearity equations<sup>(D3,D4)</sup> as follows:

$$x = \left[ \frac{(E - E_0)m_{11} + (N - N_0)m_{12} + (Z - Z_0)m_{13}}{(E - E_0)m_{31} + (N - N_0)m_{32} + (Z - Z_0)m_{33}} \right] f \quad (D3.1)$$

$$y = \left[ \frac{(E - E_0)m_{21} + (N - N_0)m_{22} + (Z - Z_0)m_{33}}{(E - E_0)m_{31} + (N - N_0)m_{32} + (Z - Z_0)m_{33}} \right] f \quad (D3.2)$$

where x and y are the photo coordinates of the control point whose ground coordinates are E, N, and Z.  $E_0$ ,  $N_0$ ,  $Z_0$  are the coordinates of the camera station, f is the focal length of the camera,  $m_{ij}$  are elements of the rotational orthogonal matrix consisting of direction cosines or of the exterior orientation elements ( $\phi$ ,  $\omega$ ,  $\kappa$ ) of the presently unknown camera station. The above equations can be written in the form of the collinearity condition using determinant notation

$$\begin{vmatrix} x & f \\ M_1 E^* & M_3 E^* \end{vmatrix} = 0 = F_x \quad (D4.1)$$

$$\begin{vmatrix} x & f \\ M_2 E^* & M_3 E^* \end{vmatrix} = 0 = F_y \quad (D4.2)$$

where

$$M_i = m_{i1}, m_{i2}, m_{i3}$$

$$E^* = \begin{bmatrix} E - E_0 \\ N - N_0 \\ Z - Z_0 \end{bmatrix}$$

and

$$m_{11} = \cos \phi \cos \kappa$$

$$m_{12} = \cos \phi \sin \kappa$$

$$m_{13} = \sin \phi$$

$$m_{21} = -\sin \omega \sin \phi \cos \kappa - \cos \omega \sin \kappa$$

$$m_{22} = -\sin \omega \sin \phi \sin \kappa + \cos \omega \cos \kappa$$

$$m_{23} = \cos \phi \sin \omega$$

$$m_{31} = -\cos \omega \sin \phi \cos \kappa + \sin \omega \cos \kappa$$

$$m_{32} = \cos \omega \sin \phi \sin \kappa - \sin \omega \cos \kappa$$

$$m_{33} = \cos \omega \cos \phi$$

Since the number of control points exceeds the number of unknowns, a least-squares adjustment is used. The observation equations are:

$$V_x = F_x + dF_x \quad (D5.1)$$

$$V_y = F_y + dF_y \quad (D5.2)$$

where F's are composed of initially estimated values and

$$dF_x = \frac{\partial F_x}{\partial E_0} dE_0 + \frac{\partial F_x}{\partial N_0} dN_0 + \frac{\partial F_x}{\partial Z_0} dZ_0 + \frac{\partial F_x}{\partial \omega} d\omega + \frac{\partial F_x}{\partial \phi} d\phi + \frac{\partial F_x}{\partial \kappa} d\kappa \quad (D6)$$

The operator d denotes corrections to the initial approximations, and the V's are residuals of the photographic measurement. Eq. D6 is substituted into eq.

D5, which, after linearization using a Taylor expansion neglecting all second and higher order terms, becomes

$$v_x = b_1 dE_0 + b_2 dN_0 + b_3 df + b_4 d\omega + b_5 d\phi + b_6 d\kappa + l_x \quad (D7)$$

where

$$l_x = F_x - x$$

and

$$b_1 = \frac{-f}{(M_3 E^*)^2} \begin{vmatrix} M_3 E^* & M_1 E^* \\ \frac{\partial (M_3 E^*)}{\partial E_0} & \frac{\partial (M_1 E^*)}{\partial E_0} \end{vmatrix}$$

$$b_2 = \frac{-f}{(M_3 E^*)^2} \begin{vmatrix} M_3 E^* & M_1 E^* \\ \frac{\partial (M_3 E^*)}{\partial N_0} & \frac{\partial (M_1 E^*)}{\partial N_0} \end{vmatrix}$$

$$b_3 = \frac{-f}{(M_3 E^*)^2} \begin{vmatrix} M_3 E^* & M_1 E^* \\ \frac{\partial (M_3 E^*)}{\partial \gamma_0} & \frac{\partial (M_1 E^*)}{\partial \gamma_0} \end{vmatrix}$$

$$b_4 = \frac{-f}{(M_3 E^*)^2} \begin{vmatrix} M_3 E^* & M_1 E^* \\ \frac{\partial (M_3 E^*)}{\partial \omega} & \frac{\partial (M_1 E^*)}{\partial \omega} \end{vmatrix}$$

$$b_5 = \frac{-f}{(M_3 E^*)^2} \begin{vmatrix} M_3 E^* & M_1 E^* \\ \frac{\partial (M_3 E^*)}{\partial \phi} & \frac{\partial (M_1 E^*)}{\partial \phi} \end{vmatrix}$$

$$b_6 = \frac{-f}{(M_3 E^*)^2} \begin{vmatrix} M_3 E^* & M_1 E^* \\ \frac{\partial (M_3 E^*)}{\partial \kappa} & \frac{\partial (M_1 E^*)}{\partial \kappa} \end{vmatrix}$$

A similar equation is formed for the  $dF_y$ . Equations D5 are solved for the differential corrections, which are then added to the approximations to update them. The iteration is continued until the corrections become negligibly small.

The positions of the cameras, as well as the orientation elements, are determined through these resections. The location of the points observed on the crater are determined by space intersections. The same mathematical concept is then repeated with the only difference being the coordinates of camera stations ( $E_0$ ,  $N_0$ ,  $Z_0$ ) now known as  $E$ ,  $N$ , and  $Z$  space coordinates. More detailed working equations can be found in References D1 through D4. The generalized flow chart for the above computations is shown in Figure D5.

#### CONTROL FRAME CALIBRATION RESULTS

Four ground control points were used for the determination of the camera stations and the orientation elements. The other 16 ground control points were used as check points for evaluation of the accuracy. The results of analysis of photographs taken under static 1-G conditions of the check points are shown in Table D1. As can be seen from this table, the coordinates of the check points, from the photogrammetric method, when compared to the results of the actual measurements differ by only 0.02 cm and 0.04 cm in the two horizontal directions and 0.14 cm in the vertical direction.

The surface area and volume of the control frame (as well as of the crater) can be obtained by using the  $E$ ,  $N$  and  $Z$  coordinates, which are determined by the space intersection. The total surface area may be computed from the following equation: (D1,D5)

$$S_j = \frac{1}{2} \sum_{i=1}^{i=n} \sqrt{(E_{i,j}^2 + Z_{i,j}^2)} (N_{i-1,j} - N_{i+1,j}) \quad (D9)$$

where  $E_{i,j}$ ,  $N_{i,j}$ , and  $Z_{i,j}$  are the coordinates of points in the  $j$  sector.

The total volume may be expressed by the following double integral (D5,D6)

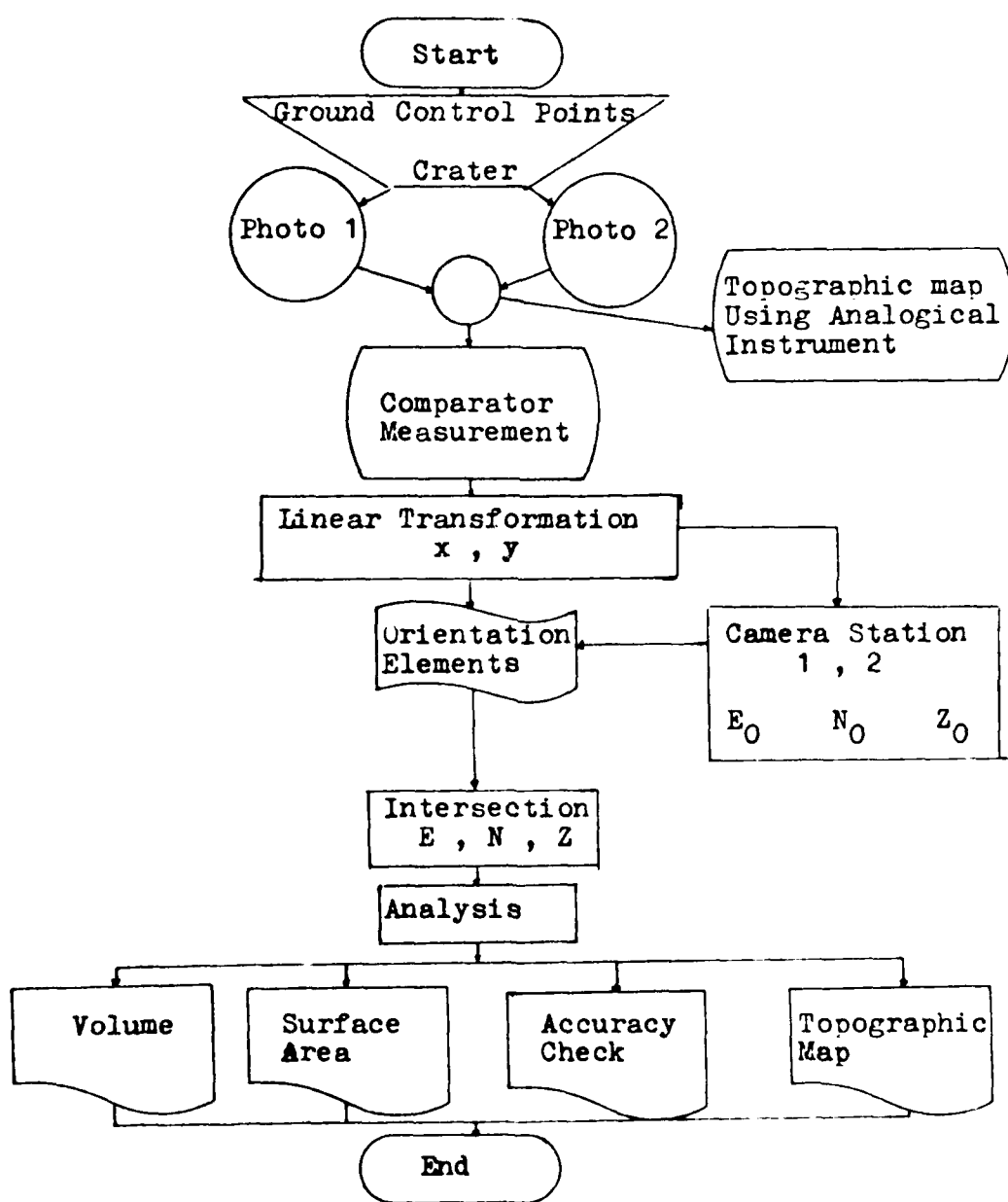


Figure D5. The generalized flow chart for photogrammetric computation.

Table D1. The results of distance determination between check points on the control frame.

No.	E (x) cm			N (y) cm			Z cm		
	Given	Comp.	Diff.	Given	Comp	Diff.	Given	Comp.	Diff.
11	100.00	99.98	+0.02	127.33	127.27	+0.06	104.00	103.82	+0.18
12	100.00	100.00	0.00	126.33	126.23	+0.10	103.00	102.76	+0.24
13	100.00	100.00	0.00	125.33	125.26	+0.07	102.00	101.77	+0.23
14	100.00	100.00	0.00	124.33	124.28	+0.05	101.00	100.87	+0.13
*15	100.00	100.00	0.00	123.33	123.31	+0.02	100.00	99.92	+0.08
21	127.33	127.27	+0.06	100.00	100.00	0.00	104.00	104.04	-0.04
22	126.33	126.31	+0.06	100.00	100.01	-0.01	103.00	103.12	-0.12
23	125.33	125.32	+0.02	100.00	100.01	-0.01	102.00	102.10	-0.10
24	124.33	124.34	-0.01	100.00	100.12	-0.02	101.00	101.16	-0.16
*25	123.33	123.36	-0.03	100.00	100.00	0.00	100.00	100.07	-0.07
31	100.00	100.00	0.00	72.67	72.77	-0.10	104.00	103.84	+0.16
32	100.00	100.01	-0.01	73.67	73.71	-0.04	103.00	102.76	+0.24
34	100.00	100.00	0.00	75.67	75.71	-0.04	101.00	100.86	+0.14
*35	100.00	100.00	0.00	76.67	76.69	-0.02	100.00	99.93	+0.07
41	72.67	72.73	-0.06	100.00	100.02	-0.02	104.00	103.91	+0.09
42	72.67	72.73	-0.03	100.00	100.02	-0.02	103.00	102.99	+0.09
43	74.67	74.67	0.00	100.00	100.01	-0.01	102.00	102.03	-0.03
44	75.67	75.65	+0.02	100.00	100.01	-0.01	101.00	101.10	-0.10
*45	76.67	76.65	+0.02	100.00	100.00	0.00	100.00	100.08	-0.08
Standard error			+0.02				0.04		0.14

\*Used as control points for resection.

$$\int_S \int f(E, N) dEdN = \sum_{i=1}^{i=m} \int_S \int p_i(E, N) dEdN \quad (D9)$$

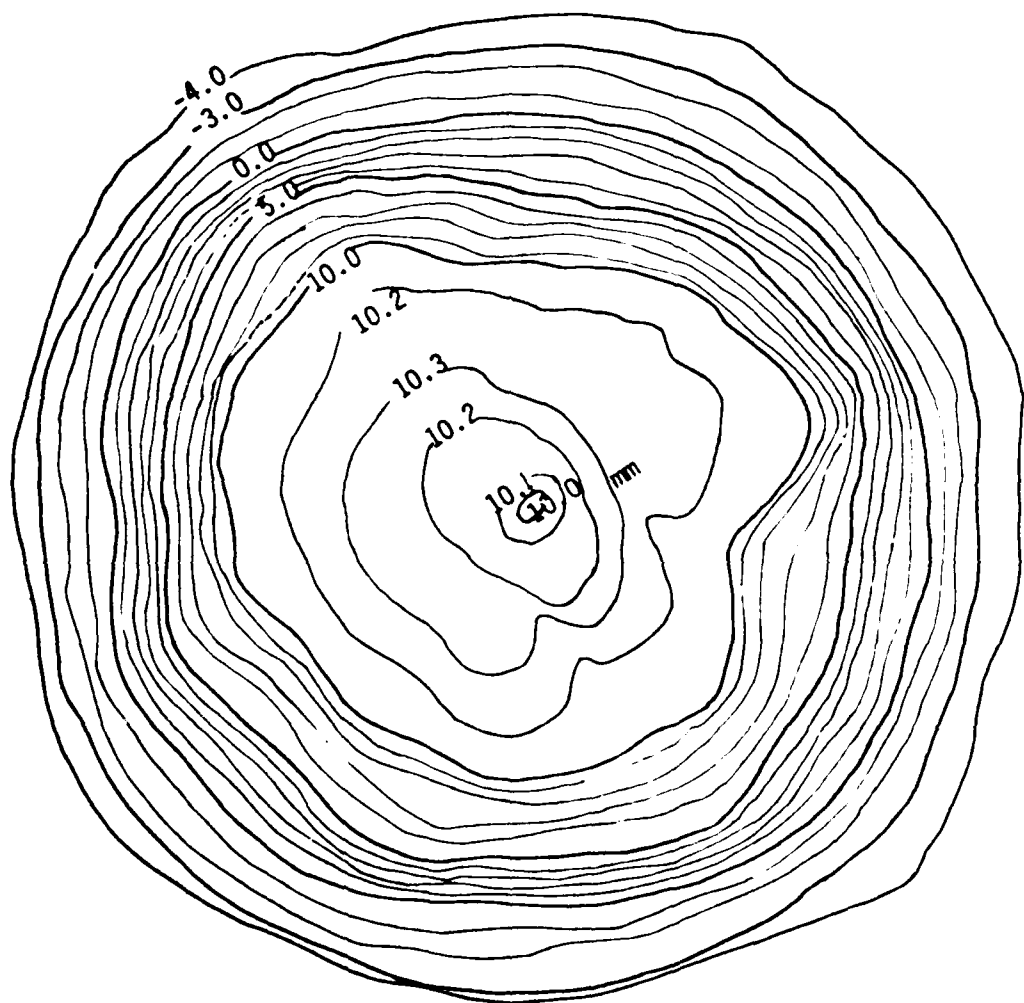
where the function  $p_i(E, N)$  is a polynomial of fixed degree  $N$ , i.e.,  $Z = f(E, N)$ . With this approach, the surface area and the volume of the control frame were determined to have values as shown in Table D2. It was found from this experiment that a 0.23% error in surface area was obtained and a 0.62% error was observed in the volume.

Table D2. Results of the surface area and volume determination for the control frame.

Sector	Surface				Volume			
	cm <sup>2</sup>				cm <sup>3</sup>			
	Given	Comp.	Diff.	Diff%	Given	Comp.	Diff.	Diff%
1	1089	1088	1	0.09	1089	1074.4	14.6	1.3
4	1387	1382	5	0.36	1387	1379	8.4	0.56
5	1495	1499	4	0.3	1495	1495	0.0	0.0
Mean				0.23%				0.62%

#### CRATER RESULTS

Using the control frame calibration of the photogrammetry system, a contour map was prepared for a typical crater photographed statically. This is shown in Fig. D6. Depths on this map compare favorably with those of the average crater contour shown in Figure D7, which was determined using eight radial profilometer measurements. The stereophoto pair is also shown in Figure D7.



0 1 2cm

SCALE

Figure D6. Topographic map for a typical crater.

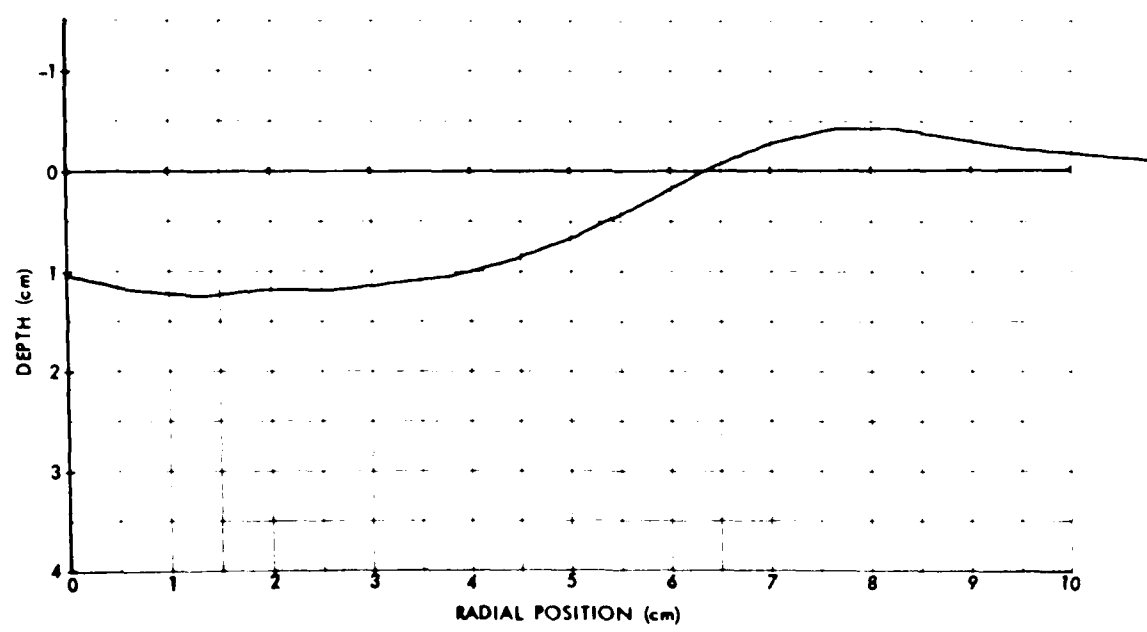


Figure D7. Stereophoto and crater profile determined by profilometer.

## CONCLUSIONS

Analytical photogrammetry has a great potential for the precise measurements of explosively formed craters under centripetal acceleration. The present experiment gives an upper limit on accuracy based on a static calibration. The surface and the volume of the control frame were obtained by photogrammetry with accuracies of 0.03 cm in the horizontal direction, 0.14 cm in the vertical direction, 0.23% in surface area and 0.62% in volume.

These results were obtained from the photographs taken with a nonmetric camera producing no fiducial marks on the photo and without correcting for lens distortion. It is expected that these results could be considerably improved with the installation of fiducial marks on the present cameras. A calibration procedure should be used to determine the true focal length of the camera and to correct for lens distortion as well as film distortion under high gravity forces.

The stability of the system under gravity and with continued use has not been conclusively tested. However, from all indications it would appear that variations in centripetal accelerations would have only a small effect if exposure as well as processing is done under controlled circumstances. The residuals in the analysis of the check control points suggest that an error existed in the prior measurements of the control frame used as the given reference dimensions or the establishment of the control frame may contain some systematic errors, both of which can be corrected.

## REFERENCES

- D1. Hou, M.C.Y., S.A. Veress, and J. W. Prothero, "A Quantitative Study of Biological Form," IEEE Transactions on Bio-Medical Engineering Vol. BME-17, Number 2, April 1970.
- D2. Hou, M.C.Y., "Linear Transformation for Data Rejection," Photogrammetric Engineering and Remote Sensing, pp. 1093-1105, 1974.
- D3. Hou, M.C.Y., "Adaptation of Analytical and Semianalytical Numerical Photogrammetry Methods Into Production Routings in Highway Photogrammetry," Final Research Report, Washington State Highway Commission in Cooperation With U.S. Department of Transportation, Federal Highway Administration, 1973.
- D4. Keller, M. and Tewinkel, "Space Resection in Photogrammetry," Technical Report No. 32, U.S.C. & G.S.
- D5. Hou, M.C.Y., S.A. Veress, "Determination of Surface Area and Volume of a Specimen by Photogrammetry," Symposium on Close-Range Photogrammetry, Jan. 1971, Urbana, Illinois.
- D6. Kheyfets, B.C., "Some Problems in Determining the Volumes of Bodies Bounded by Topographic Surfaces," Geodesy and Aerophotography, No. 5, 1966.

## DISTRIBUTION LIST

### DEPARTMENT OF DEFENSE

Assistant to the Secretary of Defense  
Atomic Energy  
    ATTN: Executive Assistant

Defense Advanced Rsch. Proj. Agency  
    ATTN: TIO

Defense Intelligence Agency  
    ATTN: DB-4C, E. O'Farrell  
    ATTN: DT-1C  
    ATTN: DT-2  
    ATTN: DB-4N

Defense Nuclear Agency  
    4 cy ATTN: TITL  
    4 cy ATTN: SPSS

Defense Technical Information Center  
12 cy ATTN: DD

Field Command  
Defense Nuclear Agency  
    ATTN: FCPR  
    ATTN: FCTK

Field Command  
Defense Nuclear Agency  
Livermore Division  
    ATTN: FCPRL

Interservice Nuclear Weapons School  
    ATTN: TTV

Joint Strat. Tgt. Planning Staff  
    ATTN: JLA  
    ATTN: NRI-STINFO Library

NATO School (SHAPE)  
    ATTN: U.S. Documents Officer

Undersecretary of Defense for Rsch. & Engrg.  
    ATTN: Strategic & Space Systems (OS)

### DEPARTMENT OF THE ARMY

BMD Advanced Technology Center  
Department of the Army  
    ATTN: ICRDABH-X  
    ATTN: ATC-T

Chief of Engineers  
Department of the Army  
    ATTN: DAEN-MCE-D  
    ATTN: DAEN-RDM

Deputy Chief of Staff for Ops. & Plans  
Department of the Army  
    ATTN: MOCA-ADL

Harry Diamond Laboratories  
Department of the Army  
    ATTN: DELHD-N-P  
    ATTN: DELHD-I-TL

### DEPARTMENT OF THE ARMY (Continued)

U.S. Army Ballistic Research Labs  
    ATTN: DRDAR-TSB-S  
    ATTN: DRDAR-BLT, W. Taylor  
    ATTN: DRDAR-BLE, J. Keefer  
    ATTN: DRDAR-BLV

U.S. Army Engineer Center  
    ATTN: DT-LRC

U.S. Army Engineer Div., Huntsville  
    ATTN: HNDEO-SR

U.S. Army Engineer Div., Ohio River  
    ATTN: ORDAS-L

U.S. Army Engr. Waterways Exper. Station  
    ATTN: WESSE, L. Ingram  
    ATTN: J. Strange  
    ATTN: WESSD, G. Jackson  
    ATTN: Library  
    ATTN: WESSA, W. Flathau

U.S. Army Material & Mechanics Rsch. Center  
    ATTN: Technical Library

U.S. Army Materiel Dev. & Readiness Command  
    ATTN: DRXAM-TL

U.S. Army Missile Command  
    ATTN: RSIC

U.S. Army Mobility Equip. R&D Command  
    ATTN: DRDME-WC

U.S. Army Nuclear & Chemical Agency  
    ATTN: Library

XVIII Airborne Corps  
Department of the Army  
    ATTN: F. Ford

### DEPARTMENT OF THE NAVY

David Taylor Naval Ship R&D Center  
    ATTN: Code 1844  
    ATTN: Code 142-3  
    ATTN: Code 17  
2 cy ATTN: Code 1740.5, B. Whang

Naval Construction Battalion Center  
    ATTN: Code 103A  
    ATTN: Code 151, R. Odello  
    ATTN: Code 151, S. Takahashi

Naval Electronic Systems Command  
    ATTN: PME 117-71

Naval Facilities Engineering Command  
    ATTN: Code 09M, PC  
    ATTN: Code 046  
    ATTN: Code 037

Naval Material Command  
    ATTN: MAT 034-22

DEPARTMENT OF THE NAVY (Continued)

Naval Postgraduate School  
ATTN: Code 0142 Library

Naval Research Laboratory  
ATTN: Code 8440, G. O'Hara  
ATTN: Code 2627

Naval Sea Systems Command  
ATTN: SEA-0351  
ATTN: SEA-0322  
ATTN: SEA-09653

Naval Surface Weapons Center  
ATTN: Code F31  
ATTN: Code R14  
ATTN: Code R14, I. Blatstein

Naval Surface Weapons Center  
ATTN: Tech, Library & Info Services Branch

Naval War College  
ATTN: Code E-11

Naval Weapons Evaluation Facility  
ATTN: Code 10

Office of Naval Research  
ATTN: Code 474, N. Perrone  
ATTN: Code 715

Office of the Chief of Naval Operations  
ATTN: OP 981  
ATTN: OP 036G

Strategic Systems Project Office  
Department of the Navy  
ATTN: NSP-43  
ATTN: NSP-272

DEPARTMENT OF THE AIR FORCE

Air Force Geophysics Laboratory  
ATTN: LWW, K. Thompson

Air Force Institute of Technology  
ATTN: Library

Air Force Systems Command  
ATTN: DLW

Air Force Weapons Laboratory  
Air Force Systems Command  
ATTN: SUL  
ATTN: NTE, M. Plamondon  
ATTN: DYT  
ATTN: NTE-C, R. Benny  
ATTN: DEX

Assistant Chief of Staff  
Intelligence  
Department of the Air Force  
ATTN: INT

Ballistic Missile Office  
Air Force Systems Command  
ATTN: MMU

DEPARTMENT OF THE AIR FORCE (Continued)

Deputy Chief of Staff  
Research, Development, & Acq.  
Department of the Air Force  
ATTN: AFRDQSM

Deputy Chief of Staff  
Logistics & Engineering  
Department of the Air Force  
ATTN: LLEE

Foreign Technology Division  
Air Force Systems Command  
ATTN: NIIS Library

Rome Air Development Center  
Air Force Systems Command  
ATTN: TSID

Strategic Air Command  
Department of the Air Force  
ATTN: NRI-STINFO Library

DEPARTMENT OF ENERGY

Department of Energy  
Albuquerque Operations Office  
ATTN: CTID

Department of Energy  
ATTN: OMA/RD&T

Department of Energy  
Nevada Operations Office  
ATTN: Mail & Records for Technical Library

DEPARTMENT OF ENERGY CONTRACTORS

Lawrence Livermore Laboratory  
ATTN: Technical Info. Dept. Library  
ATTN: L-96, L. Woodruff  
ATTN: L-10, H. Kruger  
ATTN: W. Crowley  
ATTN: J. Nutt  
ATTN: L-200, R. Swift  
ATTN: L-200, J. Bryan

Los Alamos Scientific Laboratory  
ATTN: G. Spillman  
ATTN: R. Bridwell  
ATTN: M. Henderson  
ATTN: MS 364  
ATTN: MS 362, Librarian  
ATTN: MS 420, R. Hughes  
ATTN: MS 232, J. Lillley

Oak Ridge National Laboratory  
ATTN: Central Research Library  
ATTN: Civil Def. Res. Proj.

Sandia Laboratories  
Livermore Laboratory  
ATTN: Library & Sec. Classification Div.

Sandia Laboratories  
ATTN: A. Chabot  
ATTN: 3141

OTHER GOVERNMENT AGENCIES

Central Intelligence Agency  
ATTN: OSI/NED, J. Ingle

Department of the Interior  
Bureau of Mines  
ATTN: Tech Lib.

Federal Emergency Management Agency  
ATTN: Hazard Eval. & Vul. Red. Div.

U.S. Geological Survey  
Astrogeologic Studies  
ATTN: D. Roddy

U.S. Geological Survey  
ATTN: H. Moore

National Science Foundation  
ATTN: C. Babendrier

DEPARTMENT OF DEFENSE CONTRACTORS

Acurex Corp.  
ATTN: J. Stockton

Aerospace Corp.  
ATTN: Technical Information Services

Agbabian Associates  
ATTN: M. Agbabian

Applied Theory, Inc.  
2 cy ATTN: J. Trulio

AVCO Research & Systems Group  
ATTN: Library A830

BDM Corp.  
ATTN: T. Neighbors  
ATTN: Corporate Library

Boeing Co.  
ATTN: Aerospace Library  
20 cy ATTN: R. Schmidt

California Institute of Technology  
ATTN: R. Scott/MS 104-44

California Research & Technology, Inc.  
ATTN: K. Kreyenhagen  
ATTN: Library  
ATTN: M. Rosenblatt  
ATTN: S. Schuster

California Research & Technology, Inc.  
ATTN: D. Orphal

Calspan Corp.  
ATTN: Library

Civil Systems, Inc.  
ATTN: J. Bratton

University of Denver, Colorado Seminary  
ATTN: J. Wisotski

EG&G Washington Analytical Services Center, Inc.  
ATTN: Library

DEPARTMENT OF DEFENSE CONTRACTORS (Continued)

Eric H. Wang, Civil Engineering Rsch. Fac.  
ATTN: N. Baum

Gard, Inc.  
ATTN: G. Neidhardt

General Electric Company—TEMPO  
ATTN: DASIAC

Geocenters, Inc.  
ATTN: E. Marram

H-Tech Labs., Inc.  
ATTN: B. Hartenbaum

IIT Research Institute  
ATTN: Documents Library

Institute for Defense Analyses  
ATTN: Library

JAYCOR  
ATTN: H. Linnerud

Kaman AviDyne  
ATTN: Library  
ATTN: E. Criscione

Kaman Sciences Corp.  
ATTN: Library

Lockheed Engineering Management Services  
ATTN: R. Schaal, Code C-23

Lockheed Missiles & Space Co., Inc.  
ATTN: TIC-Library

Lockheed Missiles & Space Co., Inc.  
ATTN: Technical Library  
ATTN: T. Geery  
ATTN: Technical Information Center

Lovelace Biomedical & Envir. Rsch. Institute, Inc.  
ATTN: D. Richmond

McDonnell Douglas Corp.  
ATTN: R. Halpin

Merritt CASES, Inc.  
ATTN: Library  
ATTN: J. Merritt

Nathan M. Newmark Consult. Eng. Inc.  
ATTN: N. Newmark  
ATTN: J. Sullivan

University of New Mexico  
ATTN: CERI, G. Leigh  
ATTN: CERI, N. Baum

Pacific-Sierra Research Corp.  
ATTN: H. Brede

Pacifica Technology  
ATTN: J. Font  
ATTN: R. Allen

Physics Applications, Inc.  
ATTN: F. Ford

DEPARTMENT OF DEFENSE CONTRACTORS (Continued)

Physics International Co.

ATTN: E. Moore  
ATTN: F. Sauer  
ATTN: J. Thomsen  
ATTN: L. Behrmann  
ATTN: Technical Library

R & D Associates

ATTN: C. MacDonald  
ATTN: R. Port  
ATTN: P. Haas  
ATTN: J. Carpenter  
ATTN: Technical Information Center  
ATTN: W. Wright, Jr.  
ATTN: J. Lewis

Science Applications, Inc.

ATTN: Technical Library  
ATTN: H. Wilson

Science Applications, Inc.

ATTN: J. Dishon

Science Applications, Inc.

ATTN: D. Bernstein  
ATTN: D. Maxwell

Science Applications, Inc.

ATTN: M. Knasel

Southwest Research Institute

ATTN: A. Wenzel  
ATTN: W. Baker

State University of New York at Stony Brook

ATTN: H. Melosh

Systems, Science & Software, Inc.

ATTN: J. Riney  
ATTN: E. Pyatt  
ATTN: Library  
ATTN: R. LaFrenz  
ATTN: D. Grine  
ATTN: T. Cherry

DEPARTMENT OF DEFENSE CONTRACTORS (Continued)

Terra Tek, Inc.

ATTN: S. Green  
ATTN: Library

Tetra Tech, Inc.

ATTN: Library  
ATTN: L. Hwang

TRW Defense & Space Sys. Group

ATTN: I. Alber  
ATTN: R. Plebush  
ATTN: Technical Information Center  
ATTN: D. Baer  
2 cy ATTN: P. Dai

TRW Defense & Space Sys. Group

ATTN: E. Wong

Universal Analytics, Inc.

ATTN: E. Field

University of Dayton Research Institute

ATTN: A. Piekutowski

Weidlinger Assoc., Consulting Engineers

ATTN: J. Isenberg

Weidlinger Assoc., Consulting Engineers

ATTN: J. Wright  
ATTN: M. Baron

Westinghouse Electric Corp.

ATTN: W. Volz

SRI International

ATTN: G. Abrahamson  
ATTN: B. Gasten